A Development of a High-Energy-Resolution X-ray Spectrometer System Towards Microanalysis of Astromaterials

Tasuku Hayashi

Department of Physics, The University of Tokyo

Institute of Space and Astronautical Science,
Japan Aerospace Exploration Agency

December, 2017

Acknowledgements

I would like to express special appreciation to my advisor Professor Kazuhisa Mitsuda. He has patiently guided me throughout the journey of my thesis with his depth and breadth of knowledge. I would also thank Professor Noriko Y. Yamasaki for her support and encouragement. In addition, I express my thanks to Dr. Yoh Takei for enormous valuable discussions.

I would like to thank my thesis committee members, Professor Hiroyuki Sagawa, Professor Hiroyuki Takahashi, Professor Shogo Tachibana, Professor Yasuhiro Kishimoto, and Professor Yasushi Sutoh for valuable comments and suggestions that improved the contents of this thesis dramatically.

I would like to thank STEM-TES-EDS projects members, Dr. Hara Toru, Dr. Tanaka Kenichiro, Professor Keisuke Maehata, Yoshihiro Yamanaka, Takuji Ito, Nagata Atsushi, Nakayama Satoshi and Takefumi Miyoshi for valuable comments and support. I am grateful to Dr. Akira Takano for developing and evaluating the polycaillay for the system. SQUIDs used in this thesis were fabricated in the CRAVITY at AIST with a great help from Dr. Mutsuo Hidaka, Dr. Shuichi Nagasawa, and Dr. Satoshi Kohjiro. The three-dimentional superconducting wiring on Cu stage was performed in the PHOTO PRECISION with a great help from Takahiro Ishii and HOWA MACHUNERY with a great from Atsushi Suenaga. The superconducting flip-chip bonding was performed in MANUFACTURING SOLUTION with a great help from Hiroshi Karaki. The sapphire wafer of the circuit board was provided by Dr. Hirotake Yamamori who belongs to AIST. Dr. Shota Yoshimoto helped me when evaluating the sapphire circuit boards at 4 K.

The Olivine sample to calucurate the response function was provided by Professor Takaaki Noguchi who belongs to Kyushu University. Dr. Morita Masaki who belongs to JEOL taught me how to analyze EDS. Taku Moronaga who belongs to NIMS helped with settings for capturing STEM images.

Kenichiro Nagayoshi taught me all about TES fabrication processes. Without his work, the establishment of the TES process would have been difficult. Dr. Sakai Kazuhiro taught me all about SQUID and the analysis methods of the TES waveforms. Without his program source which is ‘tesana’, I could not be able to create the source of the analysis program. Dr. Ryo Yamamoto and Akira Chiba developed and evaluated SQUIDs and the readout system for this system. Professor Shinya Yamada taught me the way of making the response function program. Dr. Makoto Mita gave me advice on the micro-process and repaired the ICP together in the clean room. If I should mention a second author, Haruka Muramatsu would definitely be the one. She helped me to conduct the entire research in this thesis. Without her help, I could never be able to finish my thesis. I should also mention Keisei Maehisa, who helped the fabrication of the TES for these two years. A special thanks to my fellow labmates: Dr. Norio Sekiya, Takahiro Kikuchi, Yuki Tsurugasaki, Masatoshi Hoshino, Yuki Nakashima, Takahiro Nakayama, Dr. Tomotake Matsumura, Dr. Shu Koyama and Dr. Hiroaki Imada. I would also like to thank Secretary Akiko Yokoyama and Noriko Takahashi for all about the daily life in the lab.

Last but not the least, I would like to thank my family. I am grateful to my mother, father, and sister.

This work was financially supported by SENTAN, Japan Science and Technology Agency (JST). This work was supported by Grant-in-Aid for JSPS Fellows (17J07948).

Tasuku Hayashi

Abstract

We have developed a high energy-resolution EDS (Energy Dispersive x-ray Spectrometer) system for an STEM (Scanning Transmission Electron Microscope) utilizing a TES (Transition Edge Sensor) microcalorimeter array. We have developed not only the detector chip, but also the spectrometer as a whole system including from the detector and the detector head to calibration and analysis methods as an STEM EDS. Although the system is useful for wide varieties of material analysis, as the calibration and analysis methods, we considered analysis of astromaterials, where precise determination of O to Si ratio is one of the key parameters for the understanding of history of silicates in planetary formation.

Requirements for the STEM EDS are a high energy-resolution of < 10 eV FWHM, high counting rate capability (> 5 kcps), and a wide energy range (0.5 - 15 keV). To fulfill the requirements we adopted and developed an 8×8 format, 64-pixel TES microcalorimeter array, and obtained an energy resolution of 4.8 eV in a laboratory low counting-rate environment. The decay time constant of the X-ray pulse was 70 μs, which is fast enough to obtain a maximum counting rate of ~ 300 cps per pixel. The TES microcalorimeter array was designed and fabricated in house using facilities at ISAS/JAXA and Tokyo Metropolitan University.

We then developed a detector head on which not only the TES microcalorimeter but also the cryogenic front-end electronics were mounted. In order to reduce the number of wire bondings, we adopted superconducting flip-chip bonding technology for the front-end electronics chips. This caused troubles to degrade the yield rate. Although we resolved some of the problems and made improvements by adjusting the liner thermal expansion coefficients of the materials, we still had a problem and we could read only 19 pixels on the STEM. Even with 19 pixels, we could almost satisfy the requirements for the energy resolution and counting rate simultaneously.

We analyzed an Olivine standard sample with the STEM-TES-EDS, because Olivine is a typical form of silicates in astromaterials. We could detect O Kα, Fe Lα , Cu Lα, Mg Kα, Mg Kβ, Si Kα, Si Kβ, Fe Kα and Fe Kβ lines from the sample. With an SDD (Silicon Drift Detector), a typical conventional semiconductor detector, we could not detect Cu Lα line, and also Mg Kβ and Si Kβ lines were not resolved from Mg Kα and Si Kα lines respectively. Furthermore, we could see Mg and Si absorption edge structures in the continuum spectrum with TES. These results prove that spectroscopy with TES has a high potential that opens up a new window for material analysis.

To analyze the TES spectra, we constructed the response function of the TES EDS system, which consists of the response matrix (= pulse height re-distribution function) and efficiency function (often called ancillary response file: ARF in X-ray astronomy). Some of the parameters of the response function were determined by using the Olivine spectra. From the model fits of the spectrum, we determined the energy spectrum of X-rays emitted from the Olivine sample. Then we determined the K factors which will be used as calibration data in the element abundance analysis. We analyzed the spectrum of SiO_2 taken with the STEM-TES-EDS and applied the K factors. We found the O to Si ratio was correctly estimated with the statistical error.

We investigated the difference between the conventional semiconductor-based EDS and the present TES EDS using Monte-Carlo simulations. We also simulated the cases where most of 64 pixels work instead of 19 pixels. Assuming the best-fit model of Olivine spectrum obtained with TES EDS as the input spectrum, we simulated the SDD spectrum. Since it was difficult to distinguish the continuum spectrum from emission lines, we adopted the

analysis method which uses the top hat filter and which is widely used in the material analysis. We found that the analysis results involve 10% of systematic error in O to Si abundance ratio. This is because the contaminations from Fe K and Cu K and the background continuum emission could not be properly subtracted. On the other hand, with TES spectrum, the systematic error is at most 1% for O to Si ratio, even if we do not have knowledge on the exact spectral shape of the background continuum emission.

Contents

List of Figures

List of Tables

Nomenclature

ARF	ancillary response file
at.%	atomic percent
cps	counts per second
bkn2pow	double-broken power-law function
ETF	Electron-Thermal feedback
EDS	Energy Dispersive x-ray Spectrometer
OBF	optical bloking filters
PHA	Pulse Height Analyzed value by optimum filtering
PI	Pulse Invariant
RMF	Redistribution Matrix File
STEM	Scanning Transmission Electron Microscope
SDD	Silicon Drift Detector
SAA	SQUD array amplifier
SQUID	Superconducting Quantum Interference Device
TES	Transition Edge Sensor
wt.%	weight percent

Chapter 1

Introduction

The formation and evolution of the solar system is one of the most important research subjects in astrophysics and planetary science. Understanding the early phase of the evolutions is critical, and the information is mainly obtained by astromaterials which are considered to keep the information of the early phase of the solar system. An energy-dispersive X-ray spectroscopy (EDS) on a scanning transmission electron microscope (STEM), which can perform element mapping and quantitative analysis on the subnano-scale, is an important tool in investigating the astromaterials. However the energy resolution of a conventional semiconductor-based EDS system (typically 130 eV) is sometimes insufficient to resolve emission lines at closely adjacent energies.

The software provided by venters is usually used to estimate the element concentrations, where a top-hat filter is employed in order to subtract background continuum emission. However, as discussed in Chapter 9, this method introduces systematic errors when adjacent lines overlap and/or when the underlying continuum spectrum has a non-linear spectral shape. In addition, the statistical treatment of model fits to a filtered spectrum is not straightforward because the spectral bins are not independent to each other. However, as far as we know this point is not treated properly. When we cannot dissolve the continuum spectrum and emission lines because of limited energy resolution, the top-hat filter is a useful method to find emission lines subtracting background and overlapping emission lines. However these issues mentioned above involve problems for quantitative analysis.

A transition edge sensor (TES) X-ray microcalorimeter is a promising solution to overcome these problems. TES microcalorimeters achieve a high energy resolution, a high counting rate and a wide energy range simultaneously. The ideal energy resolution of TES can reach 2 eV full-width at half maximum (FWHM) at 5.9 keV (Mn Kα). With the high energy resolution, the most of adjacent lines are resolved and the continuum spectrum and emission lines are separated. Thus the problem shown above can be resolved. In addition, because of the high signal to noise ratio of emission line to the background continuum, it is possible to detect weak emission lines which are never possible with conventional semiconductor-based EDS. The problem mentioned above are potential problems in all material analysis using EDS.

The STEM-TES-EDS project has started in 2013 to overcome the problems with TES. In the project we developed the TES-EDS system. The requirements of the TES-EDS system are a high energy resolution ($<$ 10 eV), a high counting rate ($>$ 5 kcps) capability, and a wide energy band ($0.5 - 15$ keV). In order to fulfill the requirements, we developed a new 8×8 format 64 pixel TES microcalorimeter array and the detector head optimized for the STEM-TES-EDS system. On the detector head the TES array and front-end electronics chips on which 64 SQUID (Superconducting Quantum Interference Device) array amplifiers, 64 bias shunt resisters, and 64 dumping inductors are mounted. We have proved experimentally that the detector system integrated to the STEM fulfills the requirements. We then studied the calibration and analysis methods. For this purpose we first analyzed a standard sample whose element concentrations are known to estimate the values of so-called K factors. Then we applied the value to the measurements of SiO_2 to prove that the Si to O ratio could be correctly estimated. We finally compare the material analyses with conventional semiconductor detectors and

with our TES by simulations. We find that for Olivine, the O line intensity estimated with the semiconductor spectrum contains about 25% systematic error because the instrument cannot distinguish continuum spectrum from emission lines and also because the contamination of adjacent Fe and Cu L lines cannot be subtracted precisely. With TES, we can avoid all the problems with its supreme energy resolution.

In this thesis, we newly developed a TES device with these performances required and a detector head for the assembly TES, and constructed an analysis method toward the quantitative analysis. To take high counting rate, the TES devices need to be arrayed and to increase the response speed. However, increasing the response speed of TES narrows the energy band, and widening the energy band leads to deterioration of the energy resolution and decrease response speed. In other words, these parameters are in a trade-off relationship. On the other hand, the detector head is limited by the cryogenic stage of a refrigerator, and increasing the number of wirings also loads the detector head. To solve this problem, it is necessary to introduce new mounting technology. In order to achieve the requirements, we developed the TES device optimized for the STEM-TES-EDS system.This thesis consists of ten chapters. In Chapter 2, we will review the present status of material analysis using TEM/STEM EDS. We show in particular the importance of determining O to Si ratio precisely which we consider is difficult for conventional semiconductor detectors. In Chapter 3, we describe the STEM-TES project, and then in Chapter 4 we review TES X-ray microcalorimeters and its related technologies including the SQUID array amplifies and the readout electronics. Chapter 5 is devoted for the development (design, fabrication, test and evaluation) of the TES microcalorimeter array. Then in Chapter 6, we describe the detector head developed for STEM TES EDS. In Chapter 7, the detector head is installed in the STEM as an EDS and the performance on STEM was verified. In Chapter 8 we describe the calibration and analysis methods, and their verification experiments using Olivine and SiO_2. In Chapter 9, we first summarize and discuss the development results. We then perform simulations in order to discuss the expected performance in material analysis. Finally we conclude our results in Chapter 10.

Chapter 2

Review

2.1 Astromaterials science with Microanalysis

The formation and evaluation of the solar system is one of the most important research subjects in astrophysics and planetary science. Among them, the formation of organic matters (OM) is an important issue. Understanding the early phase of the evolutions is critical (Figure 2.1 top), and the information is mainly obtained by astromaterials which are considered to keep the information of the early phase of the solar system, theoretical simulations, and observations of exoplanets. Among them "primordial" astromaterials are only substance directly analyzed on hands. By investigating the kind of the elements and crystal structure in the astormaterial, we can constrain the time of formation, formation process, and thermal history of the substance, from which we can obtain information on the formation of the solar system. The size of many astromaterials is as small as several cm to several mm, and many structures of submicro-scale are seen in the astromaterial. Moreover, it is important to know what kind of substances (such as OM and silicate) on the structure. For that purpose, we need an application capable of elemental analysis of all elements simultaneously with structure analysis on submicro-scale. In order to analyze, a transmission electron microscope (TEM) and an energy dispersive spectrometer (EDS) are used.

Small solid particles, called dust or grains, exist in both interstellar space and inter-planetary space. From

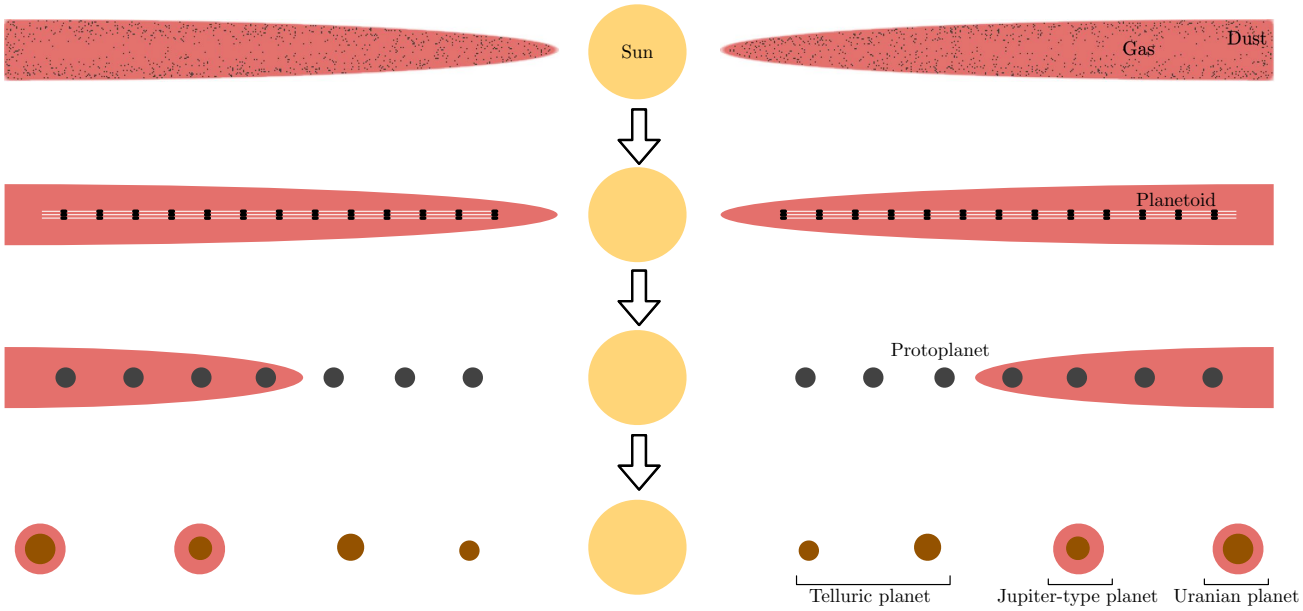

Fig. 2.1 Solar system formation process model

Table 2.1 Set of X-ray peaks being not able to separate by a semiconductor [5]

Peak 1		Peak 2		$\lvert E_{\mathrm{Peak1}} - E_{\mathrm{Peak2}} \rvert$
Characteristic X - ray	Energy (eV)	Characteristic X - ray	Energy (eV)	(eV)
Ti Kβ_1	4932	V Kα_1	4952	20
V Kβ_1	5427	Cr Kα_1	5415	12
Cr Kβ_1	5947	Mn Kα_1	5899	48
Mn Kβ_1	6490	Fe Kα_1	6404	86
Fe Kβ_1	7058	Co Kα_1	6930	128
S Kα_1	2308	Mo Lα_1	2293	15
		Pb Mα_1	2346	38
Si Kα_1	1740	W Mα_1	1775	35
		Ta Mα_1	1710	30
N Kα_1	392	C Kα_1	277	115
		Ti Lα_1	452	60
O Kα_1	525	Cr Lα_1	573	48
		V Lα_1	511	14

infrared observations, more than 98% of interstellar grains are considered to be amorphous silicate (e.g. [9]). Although amorphous silicates must have been widely present in the early stage of the solar system formation and are thought to be a primitive substance of planet formation [16], detailed roles in the planet formation process are not well established . It is widely known that an amorphous silicate easily transforms into a layered silicate due to hydration reaction after accumulation on a parent body. Elucidating the alteration process of amorphous silicate leads to understanding of the formation process and thermal history of parent bodies of present ice celestial bodies. Le Guillou and Brearley, 2014 [11] analyzed the CR3 chondrite meteorite, which is a few meteorites rich in amorphous silicate, and they suggested that hydration occurs before the amorphous silicate turns into a layered silicate. They carried out quantitative analysis using the TEM and the EDS, and indicated the excess of oxygen from analyzing characteristic X-rays from oxygen (O Kα) with respect to characteristic X-rays of Si (Si Kα). They considered that it may be derived from water by hydration. Although the authors do not mention, the precise quantitative analysis of O line is difficult with semiconductor detectors, because the semiconductor spectrum is contaminated with Fe L (from the sample) and Cu L (from the carrier of TEM) lines, as well as the bremsstrahlung continuum. We need an energy resolution better than $\sim$ 10 eV, in order to solve these problems.

2.2 Scanning Transmission Electron Microscope

The size of the silicate in the astromaterial is on the submicron-scale, and analysis using an electron microscope is indispensable for observing the submicron-scale region. Electron microscope irradiates an electron beam accelerated to several tens to several hundreds keV on a sample and has a high spatial resolution of about 1 μm $\sim$ 10 nm by capturing electrons transmitted through the sample, so that the fine observation of structure and crystal structure are possible. By using Energy-dispersive X-ray spectroscopy (EDS) to capture characteristic X-rays from the sample excited by electron beams, it is possible to analyze the composition of the sample. With Transmission electron microscope (TEM), the sample is sliced into a membrane of $\sim$ 1 μm thickness using a focused ion beam (FIB). We can obtain a better spatial resolution than a SEM (scanning electron microscope) because multiple scattering of electrons is suppressed. We can perform a better quantitative element analysis with EDS under TEM because of smaller self-absorption of X-rays. By combining an EDS and a scanning transmission electron microscope (STEM) that scans an electron beam on a sample, two-dimensional element mapping on a sample

can be performed, and element analysis on a fine structure becomes possible. A silicon drift detector (SDD) is generally used as an X-ray detector of an EDS system. In SDD, electron-hole pairs proportional to the energy of incident X-rays are generated and the energy of X-rays is measured by counting the number of these electrons. Therefore, the energy resolution is determined by the statistical fluctuation of the number of electrons, and it is described as a function of the energy E of an incident X-ray, the average ionization energy W of the photoelectrically absorbing substance, and Fano factor F:

$$\Delta E_{\mathrm{FWHM}} = 2\sqrt{2\log 2}\sqrt{EWF}. \tag{2.1}$$

In SDD, W is about 3.65 eV, F is about 0.1, and Full Width of Half Maximum is about 120 eV for 5.9 keV X-rays, it is difficult to separate the characteristic X-ray peaks shown in Table 2.1. On the low energy side, L line of copper generated from the grid used as a TEM sample holder, K line of carbon which can be contamination, and L lines of iron and chromium, which are often in the material itself, will overlap with low energy lines of interest and make it impossible to accurately measure the intensity of each element. Because quantitative analysis is based on the intensity of each element, if the strength can not be accurately obtained, the reliability of the accuracy of quantitative analysis is lowered.

2.3 Quantitative Analysis

2.3.1 Quantum analysis by X-ray energy spectra

In the EDS system, qualitative analysis and quantitative analysis are performed using the energy spectrum obtained by the X-ray detector, and therefore it is required to extract correct information from the energy spectrum. In the analysis of the X-ray energy spectrum in quantitative analysis, it is necessary to obtain the intensity of the characteristic X-rays of an element. When we determine line intensities, we need to consider backgrounds in the spectrum, which are usually consist of three components: X-rays from proximity line emissions, non X-ray background, and bremsstrahlung due to the electrons irradiated on the sample being bent by the electromagnetic field created by the nuclei and the electrons losing energy. Since this background largely depends on the element density contained in the sample, the thickness of the sample and the setup of the sample, the theoretical calculation process becomes complicated. In most of material analysis using EDS, users use an analysis software provided by the vendors. Thus it is important to know what the software does in order to be confident about the results. In most of vender's software, background is subtracted by using a top hat filter, and then line intensity is estimated by a least-square model fitting to the filtered spectrum. We consider that this process contains potential problems. First, the background subtraction is precise in only limited cases, e.g. the background is linearly dependent on energy. However this is not true for virtually all cases. Secondly the counting rates of each bin of filtered spectrum are not statistically independent to each other. This makes it very difficult to estimate the statistical parameter errors of the model fitting.

2.3.2 Cliff-Lorimer Methods

To estimate element concentrations from an EDS spectrum, Cliff-Lorimer method is widely used in material analysis. The total intensity of characteristic X-rays emitted from a sample, i (photons/s), is given by [20] and is expressed as,

$$i = CN_{\mathrm{A}}\frac{Q\omega a}{A}\rho\tau J_{\mathrm{e}}, \tag{2.2}$$

where, C is the element concentration (wt.%), N_{A} is the Avogadro constant (mol^{-1}), Q is the ionization cross section (cm^2), ω is the probability that characteristic X-rays are generated in the relaxation process of ionized atoms, a is the transition probability, A is atomic weight (g/mol), ρ is substance density ($\mathrm{g/cm}^3$), τ is the sample thickness (cm) and J_{e} is the incident electron dose (A) = (C/s). In Equation (2.2), it is assumed that the sample is thin against both for scattering and absorption of incident electrons and absorption of X-rays emitted from the sample. The intensity I (counts/s) detected by the detector using the solid angle $\left(\frac{\Omega}{4\pi}\right)$ and the detection efficiency ϵ,

$$I = CN_{\mathrm{A}}\frac{Q\omega a}{A}\rho\tau J_{\mathrm{e}}\left(\frac{\Omega}{4\pi}\right)\epsilon, \tag{2.3}$$

Therefore, the concentration of the element,

$$C = \frac{I}{N_{\mathrm{A}}\frac{Q\omega a}{A}\rho\tau J_{\mathrm{e}}\left(\frac{\Omega}{4\pi}\right)\epsilon}, \tag{2.4}$$

Equation (2.4) is possible to calculate the element concentration from X-ray intensities if we know all the parameters accurately. However, it is impossible to know all the parameters exactly, and it is difficult to correctly determine the concentration. Cliff-Lorimer, 1975 [4] proposed that the quantitative analysis is possible with the EDS system by using Equation 2.5, 2.6, 2.7, 2.8 assuming that all bright lines of all the elements contained in the sample are detected in an ideal thin film sample whose thickness can be ignored

$$\frac{C_1}{C_2} = K_{12}\frac{I_1}{I_2}, \tag{2.5}$$

$$\frac{C_3}{C_2} = K_{32}\frac{I_1}{I_2}, \tag{2.6}$$

$$\vdots$$

$$\frac{C_{\mathrm{N}}}{C_2} = K_{\mathrm{N}2}\frac{I_{\mathrm{N}}}{I_2}, \tag{2.7}$$

$$C_1 + C_2 + \cdots C_{\mathrm{N}} = 1. \tag{2.8}$$

Here, $C_1, C_2, C_3, \cdots, C_{\mathrm{N}}$ are respectively the concentration (wt.%) of elements $1, 2, 3, \cdots, N$, while $K_{12}, K_{32}, \cdots, K_{\mathrm{N}2}$ are the element K-factor (Cliff-Lormer factor) of elements $1, 3, \cdots, N$ respect to element 2, and $I_1, I_2, I_3, \cdots, I_{\mathrm{N}}$ are the intensity of characteristic X-rays of the elements $1, 2, 3, \cdots, N$. From Equation 2.4, the K factor for the element n and the element m is given by

$$\frac{C_{\mathrm{m}}}{C_{\mathrm{n}}} = \frac{\left[N_{\mathrm{A}}\frac{Q\omega a}{A}\rho\tau J_{\mathrm{e}}\left(\frac{\Omega}{4\pi}\right)\epsilon\right]_n I_{\mathrm{m}}}{\left[N_{\mathrm{A}}\frac{Q\omega a}{A}\rho\tau J_{\mathrm{e}}\left(\frac{\Omega}{4\pi}\right)\epsilon\right]_m I_{\mathrm{n}}} = \frac{\left[\frac{Q\omega a}{A}\epsilon\right]_n}{\left[\frac{Q\omega a}{A}\epsilon\right]_m}\frac{I_{\mathrm{m}}}{I_{\mathrm{n}}}, \tag{2.9}$$

$$K_{\mathrm{mn}} = \frac{\left[\frac{Q\omega a}{A}\epsilon\right]_{\mathrm{n}}}{\left[\frac{Q\omega a}{A}\epsilon\right]_{\mathrm{m}}}. \tag{2.10}$$

In order to calculate K-factor from Equation 2.10, correct radiation efficiency and detection efficiency for each element are necessary. However, since they are difficult to estimate, in real applications, a standard sample whose

concentrations of all elements are known is used to estimate K_{mn} from C_{m}, C_{n}, I_{m}, and I_{n}. However, as described above, since the energy resolution is not sufficient on the low energy side, the peaks overlap and it is difficult to obtain an accurate K-factor. Moreover, even for a TEM sample, self-absorption X-ray is not negligible. Since the assumption of Cliff-Lormer methods is not satisfied and the intensity is not accurately determined, it is not suitable to apply this method to low energy characteristic X-rays like O Kα.

2.4 Analysis with Wavelength-dispersive X-ray spectroscopy (WDS)

In the EDS system using SDD, it is not possible to separate adjacent peaks or mixed peaks because the energy resolution is not sufficient, which reduces the accuracy of quantitative analysis. In the analysis using the wavelength dispersive X-ray spectrometer (WDS), it is an X-ray detector that separates X-rays of wavelengths satisfying the Bragg condition by using spectroscopic crystals. The energy resolution ΔE_{FWHM} is proportional to E^2, and typically about 10 eV resolution can be obtained for 1 keV X-rays. On the other hand, since only diffracted X-ray photons can be detected, the detection efficiency of X-ray is lower than the SDD. Also, since the dispersion angle is proportional to the wavelength of the incident X-rays, high energy resolution cannot be obtained for short wavelength X-rays. Kato and Wallis., 2011 have made it possible to quantitatively analyze oxygen with high accuracy using an electron microprobe using WDS. In WDS, X-ray detector efficiency is low and a wide band cannot be quantitatively analyzed at the same time. Therefore, in quantitative analysis, an X-ray detector that simultaneously achieves high energy resolution, high detection efficiency, and wide energy band has been demanded. An X-ray microcalorimeter is the only X-ray detector capable of achieving this condition.

Chapter 3

Project of Next Generation STEM-EDS System

3.1 Detector for next generation EDS system

The required performances of next-generation STEM-EDS System are high energy resolution, high count rate and, wide energy range. Although WDS can obtain high energy resolution, there are problems that the energy band is narrow and the count rate is low. An X-ray microcalorimeter is a detector which fulfills these three requirements by precisely measuring a temperature increase of an X-ray photon incident on the absorber. It is a non dispersive spectrometer capable of achieving high energy resolution ($\Delta E < 10$ eV) by operating it at low temperature below 100 mK. In addition, the wide energy band can be achieved.

The microcalorimeter has already been used in an X-ray astronomical satellite like Hitomi's mission [2]. In this mission, a semiconductor thermistors have been used as the thermometer to measure, but it is not suited to read signals under the high count rate due to the signal time constant as long as 1 ms. The transition edge sensor (TES) can achieve a shorter signal time constant. The TES is a thermometer using a superconductor and it is very sensitive at its transition edge.

In principle, TES can achieve an energy resolution of 2 eV, which makes it possible to obtain the detailed fine structures of each line as shown Figure 3.1.

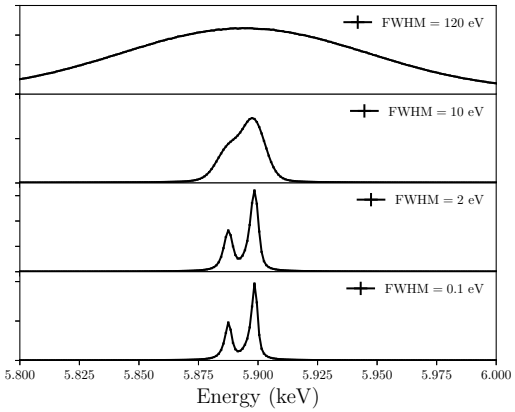

Fig. 3.1 The simulated X-ray spectra of Mn Kα for various energy resolutions

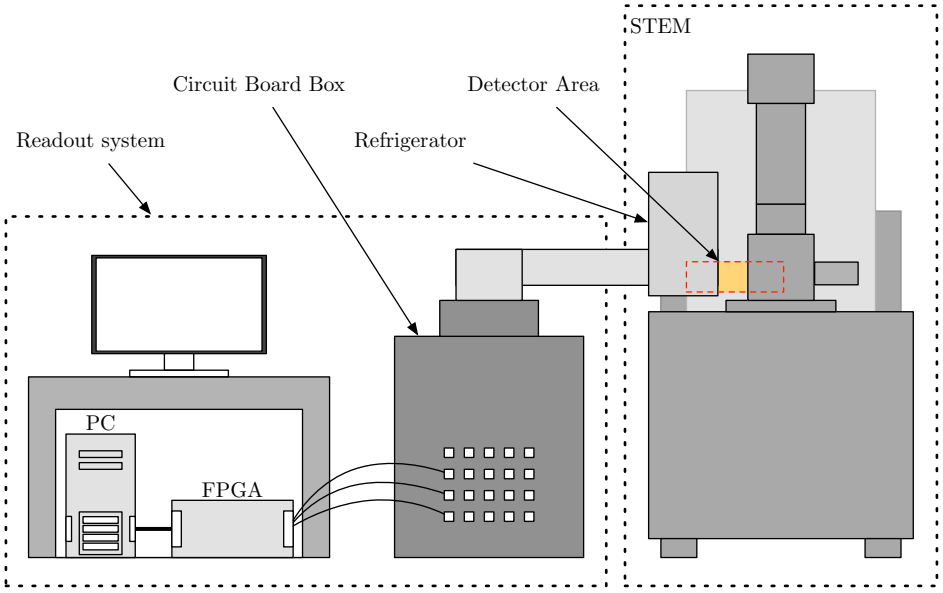

Fig. 3.2 System Concept of STEM-TES-EDS

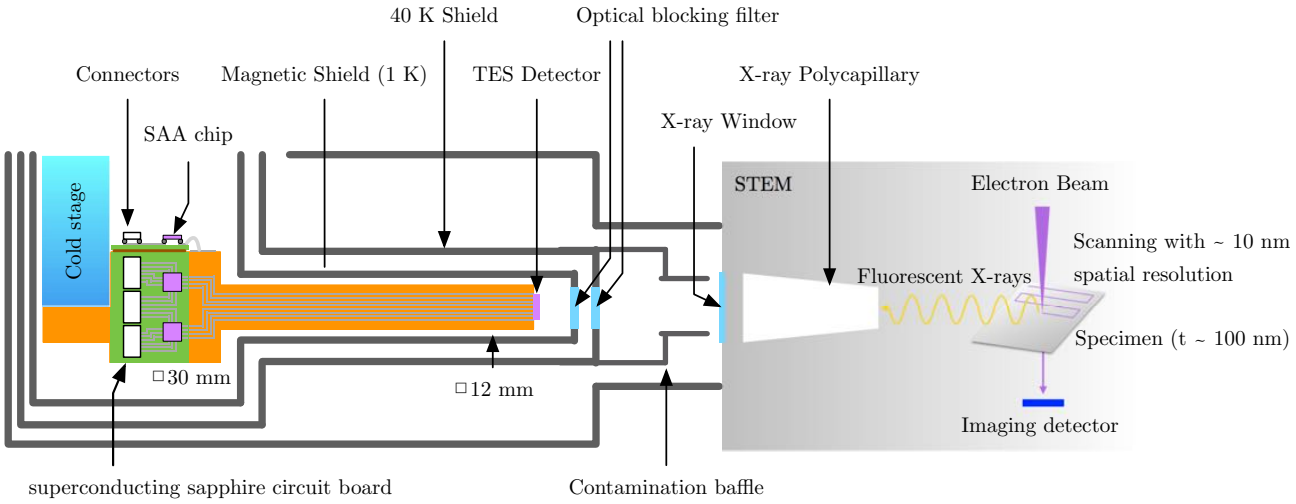

Fig. 3.3 Detector area region. the distances between the TES detector and the specimen, the cold stage and the specimen, and the X-ray polycapillary and the specimen are approximately 20 cm, 30 cm and 10 mm, respectively (see Chapter 7).

3.2 STEM-TES-EDS Project

An STEM-TES-EDS project is to develop a completely new STEM-EDS system that combines the high spatial resolution of STEM and the high energy resolution of a TES X-ray microcalorimeter. From FY2013 the STEM-TES-EDS Project started as SENTAN program of Japan Science and Technology Agency (JST), in collaboration with National Institute for Materials Science (NIMS), Hitachi High-Tech Science Corporation, Kyushu University, ISAS/JAXA, Taiyo Nippon Sanso Corporation, National Institute of Advanced Industrial Science and Technology (AIST), Hitachi High-Technologies Corporation.

The components of the STEM-TES-EDS System are divided into two parts, the STEM part and the detector

Table 3.1 Requirements of STEM-TES-EDS system

Part	Component		Details		Unit
STEM	STEM		spatial resolution	< 10	nm
	Polycapillary		Intensity gain	450	
			Focal spot size (FWHM at 1.5 keV)	300.0	μm
Detector	Refrigerator		Minimum attained temperature	< 100	mK
			Temperature stability	< 50	μK
			continuous operation time	24	h
	Detector		Energy resolution	< 10	eV
			Count rate	> 5000	cps
			Energy range	$0.1 - 15$	keV
	Readout system	Pre-amplifier	input-referred noise	< 1	nV/$\sqrt{\text{Hz}}$
			Bandwidth	DC-100	kHz
		ADC	Sampling	$\geqq 125$	MSps
			Resolution	$\geqq 14$	bit

part. In the STEM-TES-EDS system, it is important to install the superconducting detector without affecting the high spatial resolution of the STEM (Figure 3.2). The detector is needed to be install as close to the STEM as possible to increase the solid angle and obtain the high count rate. However, since the electron beam is focused by a magnetic field, and since the superconducting devices, which are used for TES and SQUID (see Chapter 4), are sensitive to magnetic field, we decided to install the detector relatively away from the STEM focus. We then decided to use a capillary X-ray optics to increase the solid angle. The polycapillary is an X-ray focusing optics and possible to conduct to the detector by reflecting X-rays having an incident angle smaller than a critical angle. We adopted the STEM developed and sold by Hitach High-Technologies. The interface to the capillary optics and TES system was developed by NIMS and the company. The polycapillary optics is developed by Hitachi High-Tech Science Corporation and Kyushu University. In detector part, there are three components: the TES microcalorimeter, the refrigerator to cool the detector, and the readout system to read out the detector signals. The refrigerator requires the cooling power that can be cooled to a temperature below the transition temperature of the TES ($<\sim 100$ mK), the high temperature stability (< 50 μK) to stabilize the operation of the TES and the long operation for long time measurement (> 24 h). The refrigerator is developed by Taiyo Nippon Sanso Corporation and Kyushu University. In STEM-TES-EDS, the detector is required to have not only a high energy resolution (< 10 eV) but also a high count rate (> 5 kcps) capability and the wide energy band ($0.5 - 15.0$ keV), and is developed by our group at ISAS. In a developing reading system, there are two types: an analog signal processing and a digital signal processing. To read out TES signals, a Superconducting Quantum Interference Devices (SQUID) array amplifier (SAA) operating at low temperature is used (see Chapter 4). In STEM, it is decided to put SAA in low temperature stage, and development of low heat dissipation type SAA is necessary. For the SAA, the room pre-amplifier and FLL circuit are provided. In order to achieve the target energy resolution of < 10 eV, an input-referred noise < 1 nV/$\sqrt{\text{Hz}}$, and a bandwidth of DC to 100 kHz are required. It is also necessary not to degrade the energy resolution of TES by a noise and a sampling during digitization. The readout system developed by Hitachi High-Tech Science Corporation, Kyushu University, ISAS/JAXA, and AIST.

We have developed the TES detectors and packaging technology around the detector stage, and evaluated the integrated system. The TES detector and the detector stage (detector head) are designed and fabricated in-house. We summarized the requirements of the STEM-TES-EDS system in Table 3.1.

Chapter 4

X-ray Microcalorimeter and Readout system

4.1 X-ray Microcalorimeter

4.1.1 Principles of X-ray Microcalorimeter

The X-ray microcalorimeter is a detector to determine the energy of an incident X-ray photon by measuring the temperature change of the detector. The simple structure of X-ray microcalorimeter is divided by three parts: an absorber to convert the incident energy to heat by absorbing the X-ray photon, a thermometer to measure the temperature change of the detector, and a thermal link to allow absorbed heat to escape to the heat sink from the detector (Figure 4.1). The X-ray photon which enter the absorber is absorbed by the photoelectric effect, and the energy changes to heat. Then the change in the temperature ΔT of the detector is expressed by the following:

$$\Delta T = \frac{E}{C}, \tag{4.1}$$

where E is the incident X-ray energy and C is the heat capacity of the detector. The heat generated in the absorber escapes to the heat sink through the thermal link from the detector and the detector slowly returns to the equilibrium state by the following equation,

$$C\frac{d\Delta T}{dt} = -G\Delta T, \tag{4.2}$$

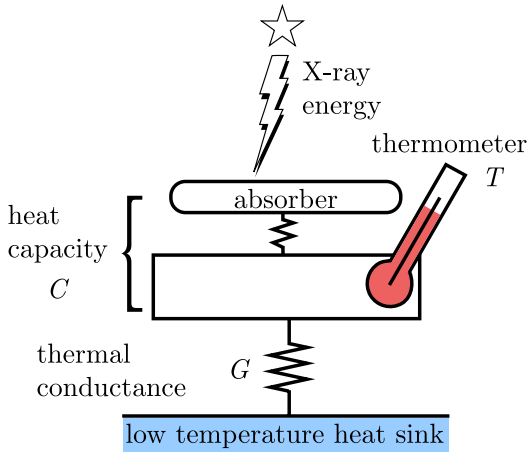

Fig. 4.1 X-ray microcalorimeter model

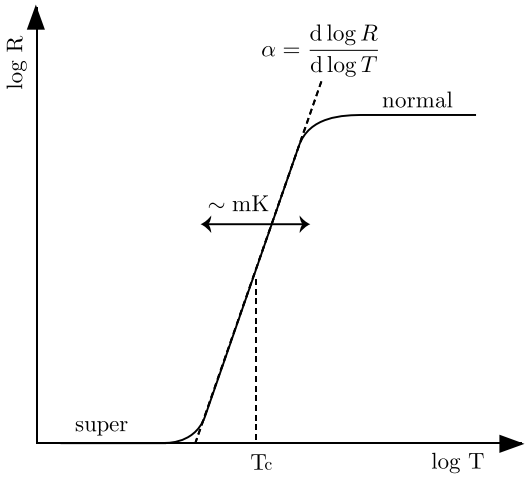

Fig. 4.2 Transition Edge

where G is the thermal conductivity of the link to the sink. Therefor, the temperature of the detector is decayed by the exponential of the time constant as the following,

$$\tau_0 = \frac{C}{G}. \tag{4.3}$$

The energy resolution of X-ray microcalorimeter is limited by a thermal fluctuation in the detector. The number of phonons in the detector is written as $N \sim CT/k_{\mathrm{B}}T = C/k_{\mathrm{B}}$, and then the thermal fluctuation of the detector will be

$$\Delta U \sim \sqrt{N} k_{\mathrm{B}} T = \sqrt{k_{\mathrm{B}} T^2 C}. \tag{4.4}$$

Generally, the intrinsic energy resolution of X-ray microcalorimeter is

$$\Delta E_{\mathrm{FWHM}} = 2.35\xi\sqrt{k_{\mathrm{B}} T^2 C}, \tag{4.5}$$

as we derive in subsection 4.5 [14], where ξ is a parameter determined by the sensitivity of the thermometer, operating conditions, etc.

4.2 Transition Edge Sensor (TES)

Thermometers used for measuring temperature change of the detector are resistances as a function of the temperature. In such a case, the sensitivity of thermometer is defined as follows:

$$\alpha \equiv \frac{d\log R}{d\log T} = \frac{T}{R}\frac{dR}{dT}, \tag{4.6}$$

where T is the temperature of the thermometer and R is the resistance of the thermometer. Increasing the sensitivity α of the thermometer leads to an improvement in the energy resolution of the microcalorimeter. One of the candidates of the thermometer is semiconductor. The sensitivity of the semiconductor is $|\alpha| \sim 6$. However, using superconductor, it is possible to achieve one hundred times better sensitivity than that of the semiconductor. Transition edge sensor (TES) is a thermometer with a sharp superconducting transition edge and measures the temperature change as a rapid resistance change. Since superconducting transition occurs in a very narrow temperature range ($\sim$ mK) (Figure 4.2), the TES can achieve the high sensitivity $|\alpha| \sim 1000$ defined by

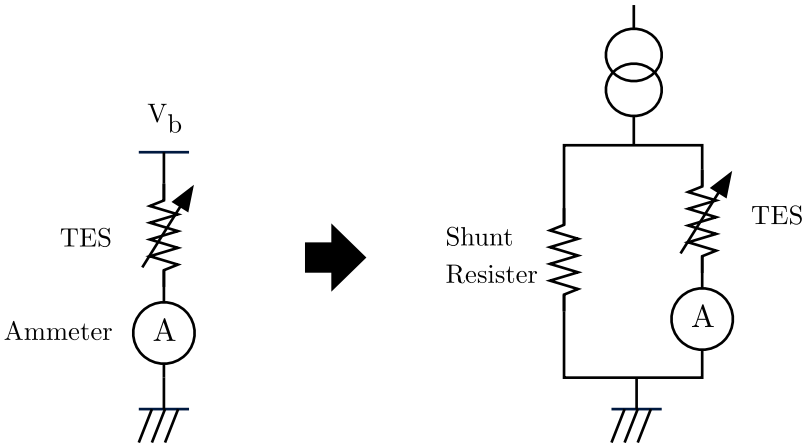

Fig. 4.3 Constant voltage bias (left), Pseudo constant voltage bias by using shunt resistance (right)

Equation (4.6). It is possible to improve the intrinsic energy resolution to 1/10 or less using the TES instead of semiconductor. When using the TES, it is necessary to keep the operating temperature of the calorimeter at the transition temperature of the TES. The transition temperature can be controlled by the proximity effect using the bilayer TES.

4.3 Electrothermal Feedback (ETF)

Since the sensitivity of the TES can achieve high sensitivity only in a very narrow range such as a few mK, it requires to keep the operating points during the transition edge. By operating the TES in the constant voltage bias and using a feedback, keeping the operating points at the transition edge can be obtained. This is called Electron-Thermal feedback (ETF) [6].

In this subsection, we describe the behavior of the TES during the ETF.

4.3.1 Response to temperature change in the Electrothermal Feedback

As shown in Figure 4.3 (left), suppose the situation where the TES is biased by the constant voltage. The temperature rises by the incident photon energy, and the resistance quickly increases. Joule heat is described $P = V^2/R$, under constant voltage bias, and the joule heat is smaller and the negative feedback works as to cancel the thermal input, and then the temperature of TES stabilizes. Practically, the TES is biased by pseudo constant voltage using a shunt resistance (Figure 4.3 right) due to the resistance in room-temperature. Assume that the TES is biased with ideal constant voltage.

Thermal conductivity is defined by

$$G \equiv dP/dT. \tag{4.7}$$

The thermal conductivity is written by a function as a temperature,

$$G = G_0 T^{n-1}, \tag{4.8}$$

and represented as a power of temperature. The index n depends on the substance responsible for thermal conduction. In the case of $n = 2$ the electrons are responsible for thermal conduction. In other case of $n = 4$

lattice vibrations are responsible for thermal conduction. G_0 is a constant.

The thermal conductivity between the thermal link and the TES is calculated by integrating Equation (4.7), considering the heat flow from the TES to the thermal link

$$P = \int_{T_{\rm bath}}^{T} G dT = \frac{G_0}{n}\left(T^n - T_{\rm bath}^n\right), \tag{4.9}$$

where $T \gg T_{\rm bath}$. In a state of equilibrium, the joule heat $P_{\rm b} \equiv V_{\rm b}^2/R_0$ and the amount of the heat flowing from the TES to the thermal link are in equilibrium so $P_{\rm b}$ is expressed as

$$P_{\rm b} = \frac{G_0}{n}\left(T_0^n - T_{\rm bath}^n\right), \tag{4.10}$$

where the T_0 is the temperature of the TES, V_b is a bias voltage, R_0 is the resistance of TES at the operating point, and $T_{\rm bath}$ is the thermal temperature. When the temperature of the TES reaches T due to a slight temperature rise $\Delta T \equiv T - T_0$, the internal energy change is equal to the heat balance,

$$C\frac{dT}{dt} = \frac{V_{\rm b}^2}{R(T)} - \frac{G_0}{n}\left(T^n - T_{\rm bath}^n\right). \tag{4.11}$$

When ΔT is represented by a first order approximation, Equation (4.11) is expressed as

$$C\frac{d\Delta T}{dt} \simeq -\frac{V_{\rm b}^2}{R_0^2}\Delta R - G_0 T^{n-1}\Delta T, \tag{4.12}$$

$$= \frac{P_{\rm b}\alpha}{T}\Delta T - G\Delta T, \tag{4.13}$$

Then, the ΔT in Equation (4.13) is represented as

$$\Delta T = \Delta T_0 \exp\left(-\frac{t}{\tau_{\rm eff}}\right), \tag{4.14}$$

where $\tau_{\rm eff}$ is a effective time constant and is defined by

$$\tau_{\rm eff} \equiv \frac{C/G}{1 + \dfrac{P_{\rm b}\alpha}{GT}}, \tag{4.15}$$

$$= \frac{\tau_0}{1 + \dfrac{P_{\rm b}\alpha}{GT}}. \tag{4.16}$$

Also, by using Equation (4.10) and Equation (4.16), $\tau_{\rm eff}$ is represented as

$$\tau_{\rm eff} = \frac{\tau_0}{1 + \dfrac{\alpha}{n}\left(1 - \left(\dfrac{T_{\rm bath}}{T}\right)^n\right)}, \tag{4.17}$$

where $\tau_0 \equiv C/G$ is a specific time constant in the system. When the temperature of thermal link is much lower than that of the TES ($T_{\rm bath}^n \ll T^n$), $\tau_{\rm eff}$ can be approximated to

$$\tau_{\rm eff} = \frac{\tau_0}{1+\dfrac{\alpha}{n}}, \tag{4.18}$$

$$\approx \frac{n}{\alpha}\tau_0, \tag{4.19}$$

where $\alpha/n \gg 1$ is satisfied. When α is large, the TES response time becomes fast due to ETF. The incident X-ray energy is measured as the current change. The current change is calculated by a simple circuit equation,

$$\Delta I = \frac{V_{\rm b}}{R(T_0+\Delta T)} - \frac{V_{\rm b}}{R(T_0)} \simeq -\frac{\Delta R}{R} I \simeq -\alpha \frac{E}{CT} I. \tag{4.20}$$

4.3.2 Current response of the TES

In the previous subsection, suppose the time-independent system however, in reality, the TES is operated in the time-dependent system. Thus, consider the response of the TES when the small power $\delta P \mathrm{e}^{i\omega t}$ is incident in the TES. Assume the response of the system is linear and the temperature change is represented by $\delta T \mathrm{e}^{i\omega t}$ that correspond to the power change $\delta P \mathrm{e}^{i\omega t}$. The heat conduction equation under no-feedback is,

$$P_{\rm bgd} + \delta P \mathrm{e}^{i\omega t} = \bar{G}(T - T_{\rm bath}) + G\delta T \mathrm{e}^{i\omega t} + i\omega C \delta T \mathrm{e}^{i\omega t}, \tag{4.21}$$

where $P_{\rm bgd}$ is the background power and $\bar{G}$ is the average of thermal conductivity.

In the equilibrium state, the background power is equal to

$$P_{\rm bgd} = \bar{G}(T - T_{\rm bath}). \tag{4.22}$$

By using Equation (4.21) and Equation (4.22), δT is represented as a function of δP,

$$\delta T = \frac{1}{G}\frac{1}{1+i\omega\tau_0}\delta P. \tag{4.23}$$

Under ETF, the energy conservation law is expressed by

$$P_{\rm bgd} + \delta P e^{i\omega t} + P_{\rm b} + \delta P_{\rm b} e^{i\omega t} = \bar{G}(T - T_{\rm bath}) + G\delta T e^{i\omega t} + i\omega C \delta T e^{i\omega t}. \tag{4.24}$$

In the bias of constant voltage, the following relational expressions hold:

$$\delta P_{\rm b} e^{i\omega t} = \frac{dP_{\rm b}}{dI}\delta I e^{i\omega t} = V_{\rm b}\delta I e^{i\omega t}, \tag{4.25}$$

$$\delta I \mathrm{e}^{i\omega t} = \frac{dI}{dR}\delta R \mathrm{e}^{i\omega t} = \frac{d}{dR}\left(\frac{V_{\rm b}}{R}\right)\delta R \mathrm{e}^{i\omega t} = -\frac{V_{\rm b}}{R^2}\delta R \mathrm{e}^{i\omega t}, \tag{4.26}$$

$$\delta R \mathrm{e}^{i\omega t} = \frac{dR}{dT}\delta T \mathrm{e}^{i\omega t} = \alpha\frac{R}{T}\delta T \mathrm{e}^{i\omega t}. \tag{4.27}$$

Then Equation (4.24) can be rewritten as

$$P_{\rm bgd} + \delta P e^{i\omega t} + \frac{V_b^2}{R} - \frac{V_b^2}{R^2}\frac{dR}{dT}\delta T e^{i\omega t} = \bar{G}(T - T_{\rm bath}) + G\delta T e^{i\omega t} + i\omega C \delta T e^{i\omega t}. \tag{4.28}$$

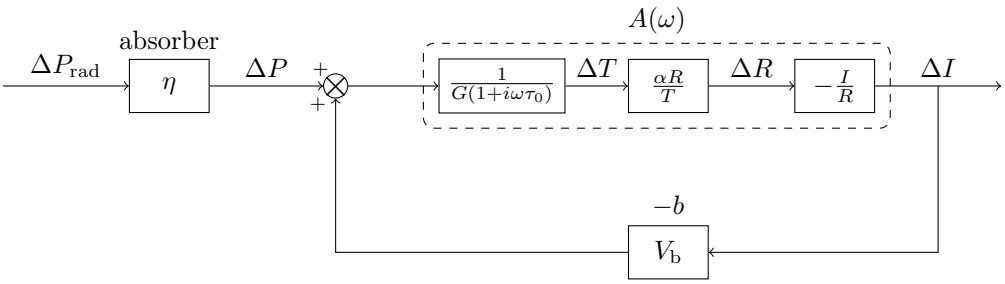

Fig. 4.4 Diagram of ETF

The solution of Equation (4.28) $\delta T e^{i\omega t}$ is

$$\delta T \mathrm{e}^{i\omega t} = \frac{1}{\alpha\dfrac{P_{\rm b}}{T} + G + i\omega C}\delta P \mathrm{e}^{i\omega t}, \tag{4.29}$$

$$= \frac{1}{G}\frac{1}{1+\dfrac{\alpha P_{\rm b}}{GT}}\frac{1}{1+i\omega\tau_{\rm eff}}\delta P \mathrm{e}^{i\omega t}. \tag{4.30}$$

The system of ETF can be represented as shown in Figure 4.4, using the theory of general feedback. In Figure 4.4, the amount of the feedback b and loop gain of system are obtained respectively.

$$b = -V_{\rm b}, \tag{4.31}$$

$$\mathcal{L}(\omega) = \frac{1}{G(1+i\omega\tau_0)} \times \alpha\frac{R}{T} \times \left(-\frac{I}{R}\right) \times (-V_{\rm b}) = \frac{\alpha P_{\rm b}}{GT}\frac{1}{1+i\omega\tau_0} \equiv \frac{\mathcal{L}_0}{1+i\omega\tau_0}, \tag{4.32}$$

where loop gain $\mathcal{L}_0$ at frequency 0 is defined by

$$\mathcal{L}_0 \equiv \frac{\alpha P_{\rm b}}{GT}. \tag{4.33}$$

The transfer function in the closed loop is defined as

$$S_I(\omega) \equiv \frac{\delta I}{\delta P}, \tag{4.34}$$

then, using $\mathcal{L}(\omega)$, $S_I(\omega)$ is expressed as

$$S_I(\omega) = \frac{1}{b}\frac{\mathcal{L}(\omega)}{1+\mathcal{L}(\omega)}, \tag{4.35}$$

$$= -\frac{1}{V_{\rm b}}\frac{\mathcal{L}_0}{\mathcal{L}_0+1+i\omega\tau_0}, \tag{4.36}$$

$$= -\frac{1}{V_{\rm b}}\frac{\mathcal{L}_0}{\mathcal{L}_0+1}\frac{1}{1+i\omega\tau_{\rm eff}}. \tag{4.37}$$

When the loop gain is sufficiently large($\mathcal{L}_0 \gg 1$), $S_I(\omega)$ is expressed as

$$S_I(\omega) = -\frac{1}{V_{\rm b}}\frac{1}{1+i\omega\tau_{\rm eff}}. \tag{4.38}$$

In the frequency range where $\omega \ll 1/\tau_{\rm eff}$ holds, $S_I(\omega)$ is expressed as the inverse of $V_{\rm b}$

$$S_I = -\frac{1}{V_{\rm b}}. \tag{4.39}$$

$S_I(\omega)$ is called current response.

The response of current to input power; The input power as a function of $P(t) = E\delta(t)$ is calculated as follows. The incident power in the space of angular frequency is represented by

$$P(\omega) = \frac{1}{2\pi}\int_{-\infty}^{\infty} E\delta(t)\mathrm{e}^{i\omega t}dt, \tag{4.40}$$

$$= \frac{E}{2\pi}. \tag{4.41}$$

Since the output current is current responsively to input, the output current is represented by

$$I(\omega) = S_I(\omega)P(\omega), \tag{4.42}$$

$$= -\frac{E}{2\pi V_{\rm b}}\frac{\mathcal{L}_0}{\mathcal{L}_0+1}\frac{1}{1+i\omega\tau_{\rm eff}}. \tag{4.43}$$

When the output current is subjected to inverse Fourier transform and returned to the time axis, the output current in time axis is expressed as

$$I(t) = \int_{-\infty}^{\infty} I(\omega)\mathrm{e}^{-i\omega t}d\omega, \tag{4.44}$$

$$= -\frac{1}{2\pi}\frac{E}{V_{\rm b}}\frac{\mathcal{L}_0}{\mathcal{L}_0+1}\int_{-\infty}^{\infty}\frac{\mathrm{e}^{-i\omega t}}{1+i\omega\tau_{\rm eff}}d\omega, \tag{4.45}$$

$$= -\frac{E}{V_{\rm b}\tau_{\rm eff}}\frac{\mathcal{L}_0}{\mathcal{L}_0+1}\exp\left(-\frac{t}{\tau_{\rm eff}}\right), \tag{4.46}$$

$$= -\frac{\alpha E}{CT}I_0\exp\left(-\frac{t}{\tau_{\rm eff}}\right), \tag{4.47}$$

and consists with Equation (4.20). Here I_0 is a current flowing through the TES in equilibrium. The temperature change by the input power $P(t) = E\delta(t)$ is

$$\Delta T(\omega) = \frac{1}{G(1+i\omega\tau_0)}\frac{1}{1+\mathcal{L}(\omega)}P(\omega), \tag{4.48}$$

$$= \frac{1}{2\pi}\frac{E}{G}\frac{1}{1+\mathcal{L}_0}\frac{1}{1+i\omega\tau_{\rm eff}}. \tag{4.49}$$

Converting to time axis, the temperature change is

$$\Delta T(t) = \int_{-\infty}^{\infty} \Delta T(\omega) \mathrm{e}^{-i\omega t} d\omega, \tag{4.50}$$

$$= \frac{1}{2\pi} \frac{E}{G} \frac{1}{\mathcal{L}_0 + 1} \int_{-\infty}^{\infty} \frac{\mathrm{e}^{-i\omega t}}{1 + i\omega\tau_{\mathrm{eff}}} d\omega, \tag{4.51}$$

$$= \frac{E}{G\tau_{\mathrm{eff}}} \frac{1}{\mathcal{L}_0 + 1} \exp\left(-\frac{t}{\tau_{\mathrm{eff}}}\right), \tag{4.52}$$

$$= \frac{E}{C} \exp\left(-\frac{t}{\tau_{\mathrm{eff}}}\right). \tag{4.53}$$

When the loop gain $\mathcal{L}_0$ is constant, Joule heat generated by X-rays is proportional to incident energy and is calculated as

$$\int V_{\mathrm{b}} I(t) dt = -\frac{\mathcal{L}_0}{\mathcal{L}_0 + 1} E. \tag{4.54}$$

In particular, when the relation $\mathcal{L} \gg 1$ holds, the integrated amount of change in Joule heat generated by incident X-ray coincides with incident energy.

4.4 Intrinsic Noise of TES

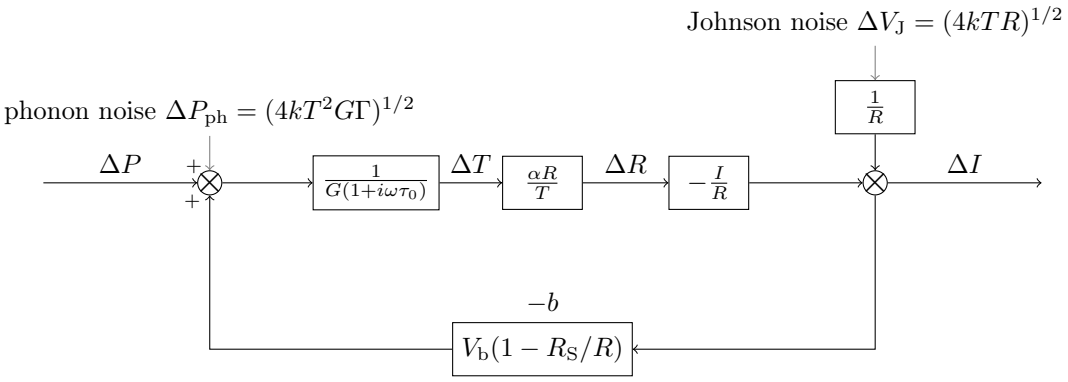

Fig. 4.5 Diagram of ETF within the Jonson noise and photon noise

In order to estimate the energy resolution, the noise level has to be evaluated. The noise has various origins such as background radiation, fluctuation of thermal bath temperature, external magnetic field noise, $1/f$ noise, and rf[*1] noise. Among them, Johnson noise and phonon noise cannot be avoided as far as using an X-ray microcalorimeter, and the theoretical energy resolution is limited by these noises. Readout noise such as the preamplifier also contributes greatly to the main noise of the TES calorimeter. Here we describe Johnson noise and phonon noise, and the readout noise is described in sub-section 4.7.4. Assume the ideal bias of constant voltage. Johnson noise is generated by the resistance of the thermometer, and phonon noise (thermal fluctuation) is generated due to the finite thermal conductivity with the thermal link. The diagram within the Johnson noise and phonon noise is shown in Figure 4.5. The phonon noise that is the origin of heat is to be input at the same point of a signal, on the other hand, the way of transmission Johnson noise differs from phonon noise, because the Johnson noise is caused by resistance.

[*1] radio frequency

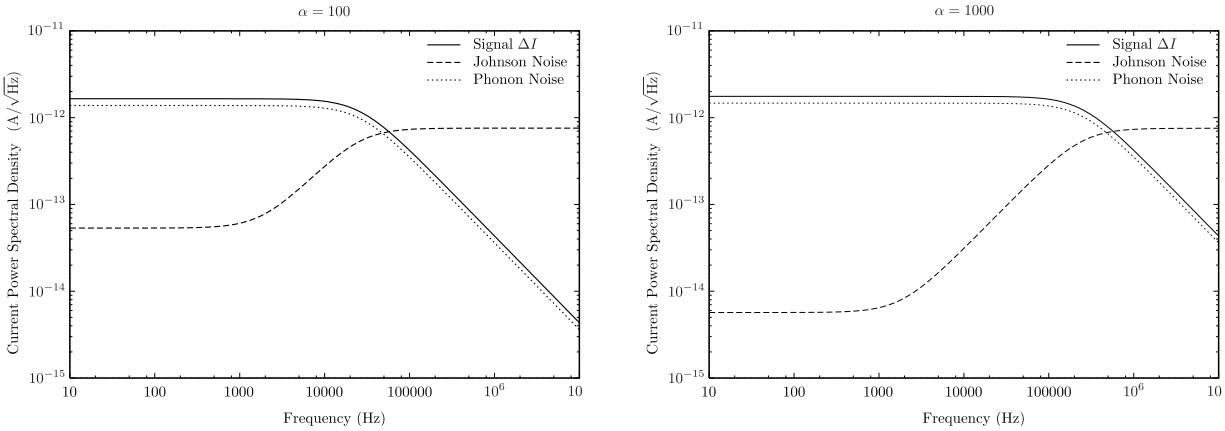

Fig. 4.6 Current density of noise. A solid line represents a signal, a broken line represents Johnson noise and a dotted line represents phonon noise. In low frequency range, Johnson noise is suppressed by ETF. (left) $\alpha = 100$, (right) $\alpha = 1000$

First, we consider phonon noise. The fluctuation of current generated by the small fluctuation of heat $\delta P_{\rm ph}$ is

$$\delta I_{\rm ph} = -\frac{1}{V_{\rm b}} \frac{\mathcal{L}(\omega)}{1+\mathcal{L}(\omega)} \delta P_{\rm ph}, \tag{4.55}$$

$$= S_I \delta P_{\rm ph}. \tag{4.56}$$

Then, the current density of phonon noise is expressed as

$$\delta I_{\rm ph}^2 = |S_I|^2 \delta P_{\rm ph}^2, \tag{4.57}$$

$$= \frac{1}{V_{\rm b}^2} \left(\frac{\mathcal{L}_0}{\mathcal{L}_0 + 1} \right)^2 \frac{1}{1+\omega^2 \tau_{\rm eff}^2} \delta P_{\rm ph}^2. \tag{4.58}$$

By [13], in the range of $0 \leq f < \infty$, the density of power spectrum of phonon noise is represented by

$$\delta P_n^2 = 4 k_B G T^2 \frac{\displaystyle\int_{T_{\rm bath}}^{T} \left(\frac{t\kappa(t)}{T\kappa(T)} \right)^2 dt}{\displaystyle\int_{T_{\rm bath}}^{T} \left(\frac{\kappa(t)}{\kappa(T)} \right) dt}, \tag{4.59}$$

$$\equiv 4 k_B G T^2 \Gamma, \tag{4.60}$$

where, $\kappa(T)$ is the thermal conductivity of the material composing the thermal link. θ is defined by $\theta \equiv T_{\rm bath}/T$. Suppose the relation between $\kappa(T)$ and θ, $\kappa(T) = \kappa(T_{\rm bath})\theta^{-(n-1)}$, is satisfied, Γ is

$$\Gamma = \frac{n}{2n+1} \frac{1-\theta^{(2n+1)}}{1-\theta^n}. \tag{4.61}$$

Substituting Equation (4.60) for Equation (4.58), the current density of phonon noise is represented as

$$\delta I_{\rm ph}^2 = 4k_{\rm B}GT^2\Gamma|S_I|^2, \tag{4.62}$$

$$= \frac{4k_{\rm B}GT^2\Gamma}{b^2}\left(\frac{\mathcal{L}_0}{\mathcal{L}_0+1}\right)^2\frac{1}{1+\omega^2\tau_{\rm eff}^2}, \tag{4.63}$$

$$= \frac{4k_{\rm B}GT^2\Gamma}{V_{\rm b}^2}\left(\frac{\mathcal{L}_0}{\mathcal{L}_0+1}\right)^2\frac{1}{1+\omega^2\tau_{\rm eff}^2}. \tag{4.64}$$

Second, we consider the current density of Johnson noise. The fluctuation of current $\delta I_{\rm J}^0$ that accompany Johnson noise $\delta V_{\rm J}$ is

$$\delta I_{\rm J}^0 = \frac{\delta V_{\rm J}}{R}. \tag{4.65}$$

This fluctuation is input to the system, and then the fluctuation of the output current is

$$\delta I_{\rm J} = \frac{1}{1+\mathcal{L}(\omega)}\delta I_{\rm J}^0, \tag{4.66}$$

$$= \frac{\dfrac{1}{\mathcal{L}_0+1}+i\omega\tau_{\rm eff}}{1+i\omega\tau_{\rm eff}}\frac{\delta V_{\rm J}}{R}, \tag{4.67}$$

$$= \frac{1}{\mathcal{L}_0+1}\frac{1+i\omega\tau_0}{1+i\omega\tau_{\rm eff}}\frac{\delta V_{\rm J}}{R}. \tag{4.68}$$

The voltage density of Johnson noise is $\delta V_{\rm J}^2 = 4k_{\rm B}TR$ in the frequency range of $0 \le f < \infty$, so the output current density is

$$\delta I_{\rm J}^2 = \frac{4k_{\rm B}T}{R}\left(\frac{1}{\mathcal{L}_0+1}\right)^2\left|\frac{1+i\omega\tau_0}{1+i\omega\tau_{\rm eff}}\right|^2, \tag{4.69}$$

$$= \frac{4k_{\rm B}T}{R}\left(\frac{1}{\mathcal{L}_0+1}\right)^2\frac{1+\omega^2\tau_0^2}{1+\omega^2\tau_{\rm eff}^2}, \tag{4.70}$$

$$= \begin{cases} \dfrac{4k_{\rm B}T}{R}\left(\dfrac{1}{\mathcal{L}_0+1}\right)^2 & \text{if } \omega \ll \tau_0^{-1} \\ \dfrac{4k_{\rm B}T}{R} & \text{if } \omega \gg \tau_{\rm eff}^{-1} \end{cases}. \tag{4.71}$$

In the frequency range of $\omega \ll \tau_0^{-1}$ the level of Johnson noise is restrained by ETF, while in the frequency range of $\omega \gg \tau_{\rm eff}^{-1}$, ETF has no effect to the Johnson noise. The total current density including phonon noise and Johnson noise is calculated by the sum of squares of phonon noise and Johnson noise,

$$\delta I^2 = \delta I_{\rm J}^2 + \delta I_{\rm ph}^2, \tag{4.72}$$

$$= \frac{4k_{\rm B}T}{R}\left(\frac{1}{\mathcal{L}_0+1}\right)^2\frac{1+\omega^2\tau_0^2}{1+\omega^2\tau_{\rm eff}^2} + 4k_{\rm B}GT^2\Gamma\frac{1}{V_{\rm b}^2}\left(\frac{\mathcal{L}_0}{\mathcal{L}_0+1}\right)^2\frac{1}{1+\omega^2\tau_{\rm eff}^2}, \tag{4.73}$$

$$= \frac{4k_{\rm B}T}{R}\frac{\dfrac{1+\Gamma\alpha\mathcal{L}_0}{(\mathcal{L}_0+1)^2}+\omega^2\tau_{\rm eff}^2}{1+\omega^2\tau_{\rm eff}^2}, \tag{4.74}$$

in $0 \leq f < \infty$. In the strong ETF limit, the total current density becomes

$$\delta I^2 = \frac{4k_{\mathrm{B}}T}{R}\frac{n/2 + \omega^2\tau_{\mathrm{eff}}^2}{1+\omega^2\tau_{\mathrm{eff}}^2}. \tag{4.75}$$

Figure 4.6 shows the frequency characteristic of phonon noise, Johnson noise, and signal. Taking the ratio of phonon noise to Johnson noise and examining the relation between them,

$$\frac{\delta I_{\mathrm{ph}}^2}{\delta I_{\mathrm{J}}^2} = \frac{\alpha\mathcal{L}_0\Gamma}{1+\omega^2\tau_0^2}, \tag{4.76}$$

in low frequency, phonon noise is $\alpha\mathcal{L}_0\Gamma$ times bigger than Johnson noise, while in $\omega > \tau_0^{-1}$, Johnson noise increases, and in $\omega \gg \tau_{\mathrm{eff}}^{-1}$ Johnson noise becomes the dominant noise component.

We take a ratio of signal to phonon noise

$$\frac{\delta P_{\mathrm{signal}}^2}{\delta P_{\mathrm{n}}} = \frac{2E^2}{4k_BGT^2\Gamma}, \tag{4.77}$$

and the relation is independent of frequency. This is because phonon noise and Johnson noise have the same frequency characteristic. Using Equation (4.37) and Equation (4.71), Johnson noise is represented by current responsively S_I

$$\delta I_{\mathrm{J}}^2 = \frac{4k_{\mathrm{B}}T}{R}\frac{b^2(1+\omega^2\tau_0^2)}{\mathcal{L}_0^2}|S_I|^2. \tag{4.78}$$

Using Equation (4.63) and Equation (4.71), the total noise is expressed as

$$\delta I^2 = \frac{4k_BT}{R}\frac{1+\omega^2\tau_0^2}{\mathcal{L}_0^2}b^2|S_I|^2 + 4k_BGT^2\Gamma|S_I|^2. \tag{4.79}$$

Noise equivalent power is defined as

$$\mathrm{NEP}(f)^2 \equiv \left|\frac{\delta I}{S_I}\right|^2. \tag{4.80}$$

The noise equivalent power that corresponds to the total noise becomes

$$\begin{aligned}
\mathrm{NEP}(f)^2 &= \left|\frac{\delta I}{S_I}\right|^2, && (4.81)\\
&= \frac{4k_BT}{R}\frac{b^2}{\mathcal{L}_0^2}\left(1+(2\pi f)^2\tau_0^2 + \frac{\mathcal{L}_0^2}{b^2}RGT\Gamma\right), && (4.82)\\
&= 4k_BTP_{\mathrm{b}}\left(\frac{1+(2\pi f)^2\tau_0^2}{\mathcal{L}_0^2} + \frac{\alpha\Gamma}{\mathcal{L}_0}\right). && (4.83)
\end{aligned}$$

4.5 Optimal Filtering and Energy resolution

To obtain the high energy resolution of the X-ray microcalorimeter, we need to analyze data carefully. Since the noise has an effect on the pulse shape, we cannot obtain the ideal pulse shape, so the high energy resolution cannot be obtained by analysis using only the peak value of the pulse. Generally, optimal filtering methods [19]

are used for the analysis of X-ray microcalorimeters. It assumes that every pulse is an energy scaled version of a single template ($A \times M(f)$) and the signal can be written as ideal signal with a stationary noise in frequency,

$$D(f) = A \times M(f) + N(f), \tag{4.84}$$

where $M(f)$, $N(f)$, and A are an ideal pulse which roughly equals to S_I, the power spectrum of the measured noise, and the magnitude respectively. The χ^2 fit is used to estimate the optimal pulse hight,

$$\chi^2 \equiv \int \frac{|D(f) - A \times M(f)|^2}{|N(f)|^2}. \tag{4.85}$$

Then, the solution of A is

$$A = \frac{\int_{-\infty}^{\infty} \frac{DM^* + D^*M}{2|N|^2} df}{\int_{-\infty}^{\infty} \frac{|M|^2}{|N|^2} df}. \tag{4.86}$$

These relations $D(-f) = D(f)^*$ and $M(-f) = M(f)^*$ are satisfied since $D(f)$ and $M(f)$ are Fourier components of real function. Thus, the following equation

$$\int_{-\infty}^{\infty} \frac{D(f)M(f)^*}{2|N|^2} df = -\int_{\infty}^{-\infty} \frac{D(-f)M(-f)^*}{2|N|^2} df = \int_{-\infty}^{\infty} \frac{M(f)D(f)^*}{2|N|^2} df, \tag{4.87}$$

is established. The solution of A becomes

$$A = \frac{\int_{-\infty}^{\infty} \frac{D(f)M(f)^*}{|N(f)|^2} df}{\int_{-\infty}^{\infty} \frac{|M(f)|^2}{|N(f)|^2} df}, \tag{4.88}$$

or

$$A = \frac{\int_{-\infty}^{\infty} \frac{D(f)}{M(f)} \left|\frac{M(f)}{N(f)}\right|^2 df}{\int_{-\infty}^{\infty} \left|\frac{M(f)}{N(f)}\right|^2 df}. \tag{4.89}$$

A is the average value of signal to noise ratio (S/N) weighted by $D(f)/M(f)$. When the denominator of Equation (4.89) is Fourier transformed, A is rewritten as

$$A = \frac{\int_{-\infty}^{\infty} D(t)\mathcal{F}^{-1}\left(\frac{M(f)}{|N(f)|^2}\right) dt}{\int_{-\infty}^{\infty} \left|\frac{M}{N}\right|^2 df}, \tag{4.90}$$

where $\mathcal{F}^{-1}$ represents the inverse Fourier transform, and we call $T(t) \equiv \mathcal{F}^{-1}\left(\frac{M(f)}{|N(f)|^2}\right)$ the template of optimal filtering. Here we can write down the pulse height as time dependence,

$$H = N \int_{-\infty}^{\infty} D(t)T(t)dt, \tag{4.91}$$

or for discrete data

$$H = N \sum_{i} D_i(t)T_i(t). \tag{4.92}$$

N is a normalized constant and $D_i(t)$, $T_i(t)$ are quantized pulse and template. The averaged pulse of actually obtained X-ray pulses is used for the model pulse.[*2]

The energy resolution of the TES is given by

$$\Delta E_{\rm rms} = \left(\int_0^{\infty} \frac{4df}{\mathrm{NEP}^2(f)} \right)^{-\frac{1}{2}}, \tag{4.93}$$

using NEP(f) [14]. Using Equation (4.83) and Equation (4.93), the energy resolution determined by the intrinsic noises becomes

$$\Delta E_{\rm rms} = \left(\int_0^{\infty} \frac{4df}{\frac{4k_BT}{R}\frac{b^2}{\mathcal{L}_0^2}\left((1+(2\pi f)^2\tau_0^2) + \frac{\mathcal{L}_0^2}{b^2}RGT\Gamma\right)} \right)^{-\frac{1}{2}}, \tag{4.94}$$

$$= \sqrt{\frac{4k_{\rm B}T}{R}\frac{b^2}{\mathcal{L}_0^2}\tau_0\sqrt{1+\frac{\mathcal{L}_0^2}{b^2}RGT\Gamma}}, \tag{4.95}$$

$$= \sqrt{4k_{\rm B}T^2C\frac{b^2}{RGT\mathcal{L}_0^2}\sqrt{1+\frac{\mathcal{L}_0^2}{b^2}RGT\Gamma}}, \tag{4.96}$$

ξ is defined by

$$\xi \equiv 2\sqrt{\frac{b^2}{RGT\mathcal{L}_0^2}\sqrt{1+\frac{\Gamma}{\frac{b^2}{RGT\mathcal{L}_0^2}}}}. \tag{4.97}$$

The Full band Width of Half Maximum (FWHM) of the energy resolution becomes

$$\Delta E_{\rm FWHM} = 2.35\xi\sqrt{k_{\rm B}T^2C}. \tag{4.98}$$

Substituting Equation (4.31) and Equation (4.33) into Equation (4.97), ξ becomes

$$\xi = 2\sqrt{\frac{1}{\alpha\mathcal{L}_0}\sqrt{1+\alpha\mathcal{L}_0\Gamma}}. \tag{4.99}$$

In $T_{\rm bath} \ll T$, Γ,P_b, and $\mathcal{L}_0$ satisfy these relations: $\Gamma \sim 1/2$, $P_{\rm b} \sim GT/n$, $\mathcal{L}_0 \sim \alpha/n$, so ξ becomes

$$\xi \simeq 2\sqrt{\sqrt{n/2}/\alpha}. \tag{4.100}$$

[*2] We calculate Equation (4.90) using the averaged pulse as $M(f)$, when $D(f) = M(f)$, the value of A is equal to 1. On the other hand we calculate Equation (4.90) using $M(f)$ as current responsively, and A becomes incident energy in $D(f) = M(f)$.

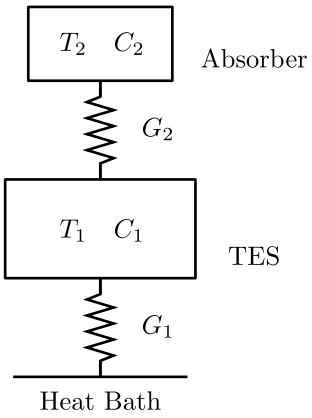

Fig. 4.7 Model when TES and absorber are connected with finite thermal conductivity

When α is sufficiently larger than 1, the energy resolution determined by intrinsic noises becomes better in proportion to $\alpha^{-1/2}$, e.g. α is roughly 1000 then ξ is below 0.1. In fact, the energy resolution may be limited by several noises such as the readout noise, temperature fluctuation of the thermal link, and other unknown noise. In general, the energy resolution (Equation (4.98)) has different dependencies. Variation of the pulse waveform for each event also causes degradation of energy resolution.

4.6 Response of TES when TES and absorber are connected with finite thermal conductivity

We consider the response of the TES when the TES and the absorber are connected with finite thermal conductivity and the model is shown in Figure 4.7.

4.6.1 Formula that represents the temperature change

The temperature difference occurs between the TES and the absorber until heat is transferred from the absorber to the TES. Thermal fluctuation noise is generated by thermal conductivity G_2 of TES and absorber.

Equations expressing the flow of heat become,

$$\frac{d\Delta T_2}{dt} = -\frac{G_2}{C_2}(\Delta T_2 - \Delta T), \tag{4.101}$$

$$\frac{d\Delta T_1}{dt} = -\frac{G_1}{C_1}\Delta T_1 + \frac{G_2}{C_1}(\Delta T_2 - \Delta T_1) - \frac{P_\mathrm{b}\alpha}{C_1 T_1}\Delta T_1. \tag{4.102}$$

G_1 is the thermal conductivity between the TES and the thermal link. G_2 is the thermal conductivity between the TES and the absorber. C_1 and T_1 are heat capacity and temperature of the TES respectively, while C_2 and T_2 are heat capacity and temperature of the absorber respectively. The last term on the right side of Equation (4.102) expresses change in Joule heat by ETF. Taking the sum or difference of Equation (4.101) and Equation (4.102), the following relation is obtained

$$\frac{d}{dt}\left(\Delta T_2 - \Delta T_1\right) = -\left(\frac{G_2}{C_2} + \frac{G_2}{C_1}\right)\left(\Delta T_2 - \Delta T_1\right) + \frac{G_1}{C_1}(1+\mathcal{L}_0)\Delta T, \tag{4.103}$$

$$\frac{d}{dt}\left(\Delta T_1 + \frac{C_2}{C_1}\Delta T_2\right) = -\frac{G_1}{C_1}\Delta T_1. \tag{4.104}$$

Assume that ΔT_2 is shorter than the time of the temperature change in the whole system and consists with ΔT_1, i.e. $G_2 \gg G_1(1+\mathcal{L}_0)$ holds. We can neglect the second term of Equation (4.103). Equation (4.103) is expressed as

$$\frac{d}{dt}\left(\Delta T_2 - \Delta T_1\right) = -\left(\frac{G_2}{C_2} + \frac{G_2}{C_1}\right)\left(\Delta T_2 - \Delta T_1\right). \tag{4.105}$$

It is easy to solve Equation (4.105), and the solution becomes

$$\Delta T_2 - \Delta T_1 \propto \exp\left[-\left(\frac{G_2}{C_{\rm int}}\right)t\right], \tag{4.106}$$

$C_{\rm int}$ is defined by

$$\frac{1}{C_{\rm int}} \equiv \frac{1}{C_1} + \frac{1}{C_1}. \tag{4.107}$$

The decay time constant τ_2 until the temperature ΔT_2 becomes ΔT_1 is

$$\tau_2 = \frac{C_{\rm int}}{G_2} = \frac{CC_2}{(C+C_2)G_2}. \tag{4.108}$$

After the decay time τ_2 has elapsed, ΔT_2 is equal to ΔT_1. ΔT_1 is calculated by Equation (4.104) as follows:

$$\left(1+\frac{C_2}{C_1}\right)\frac{d}{dt}\Delta T_1 = -\frac{G_1}{C_1}(1+\mathcal{L}_0)\Delta T_1, \tag{4.109}$$

$$\frac{d}{dt}\Delta T_1 = -\frac{G_1}{C_1+C_2}(1+\mathcal{L}_0)\Delta T_1, \tag{4.110}$$

$$\Delta T_1 \propto \exp\left(-\frac{G_1}{C_1+C_2}(1+\mathcal{L}_0)t\right). \tag{4.111}$$

The decay time of ΔT_1 becomes

$$\tau_1 = \frac{C_1+C_2}{G}\frac{1}{1+\mathcal{L}_0}. \tag{4.112}$$

The temperature of the TES matches that of the absorber after the decay time τ_2 has elapsed, then becomes stationary state after the decay time τ_1. τ_1 corresponds to the effective decay time of the microcalorimeter.

4.6.2 Pulse waveforms absorbed by absorber and absorbed by TES

Consider the temperature change when X-rays are absorbed by absorber and when absorbed by TES respectively, and we discuss the output pulse waveform because the change in temperature and the change in output correspond.

First, we handle the case where X-rays are absorbed on the absorber. When X-rays are incident into the absorber, the temperature of the absorber rises by $\Delta T_2 = E/C_2$. The heat flows from the absorber to the TES

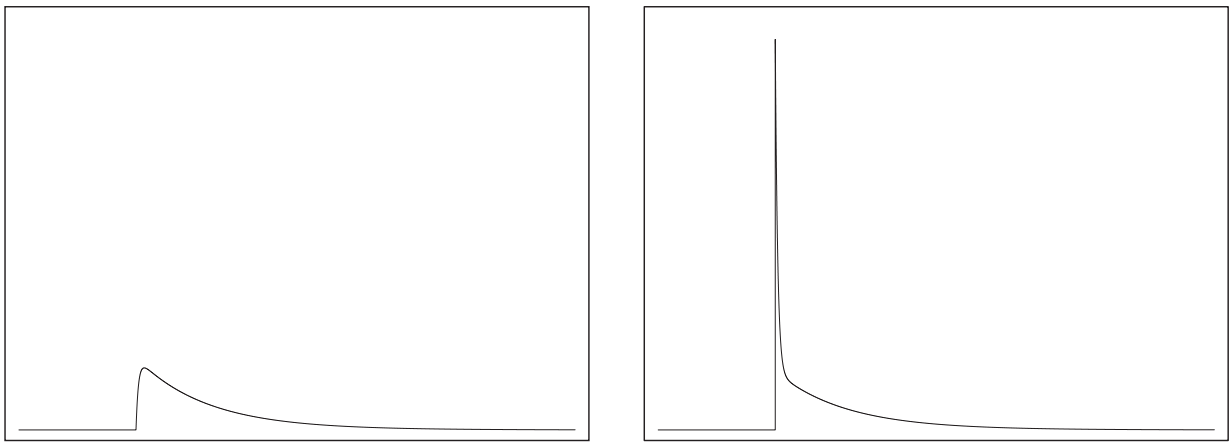

Fig. 4.8 Change in the temperature of the TES calculated by models. The horizontal axis represents time. The case where the absorber absorbed an incident X-ray (left), the other case where the TES absorbed an incident X-rays (right).

with the time scale τ_2, and the temperature of the TES returns to the original value. Thus the temperature of the TES is represented by the rise time constant τ_2 and the decay time constant τ_1,

$$\Delta T_1 \propto \left(\exp\left(-\frac{t}{\tau_1}\right) - \exp\left(-\frac{t}{\tau_2}\right)\right), \tag{4.113}$$

And next, we handle the case where X-rays are absorbed on the TES. The temperature of the TES rises by $\Delta T_1 = E/C_1$. The heat flows from the TES to the absorber with τ_2 and the temperatures of the TES and the absorber come back to the original values. The temperature of the TES is represented by the exponential function with two constant decay times, τ_1 and τ_2

$$\Delta T_1 \propto \left(\exp\left(-\frac{t}{\tau_1}\right) + \exp\left(-\frac{t}{\tau_2}\right)\right). \tag{4.114}$$

We calculate Equation (4.105), assuming $C_2/C_1 = 4$ and $\tau_1/\tau_2 = 20$. The case where the absorber absorbed X-rays is shown on the left side of Figure 4.8 and the other case where the TES absorbed X-rays is shown on the right side of Figure 4.8.

4.6.3 Formulation of output current by frequency responsibility

Finally, we consider the output current when X-rays are incident on the absorber. In subsection 4.3.2, we assume that the incident energy is given as a delta function $P(t) = E\delta(t)$. However, in the case with finite thermal conductivity between the absorber and the TES, heat input is represented as

$$P(t) = \frac{E}{\tau_2}\exp\left(-\frac{t}{\tau_2}\right) \qquad (t \geq 0). \tag{4.115}$$

When $t = 0$, the X-ray enters the absorber. The input power of heat $P(\omega)$ is calculated in the same way as in subsection 4.3.2,

$$P(\omega) = \frac{1}{2\pi}\int_0^\infty \frac{E}{\tau_2}\exp\left(-\frac{t}{\tau_2}\right)\mathrm{e}^{-i\omega t}\mathrm{d}t = \frac{E}{2\pi}\frac{1}{1+i\omega\tau_2}. \tag{4.116}$$

The output current becomes

$$I(\omega) = P(\omega)S_{\mathrm{I}}(\omega), \tag{4.117}$$
$$= -\frac{E}{2\pi}\frac{1}{V_{\mathrm{b}}}\frac{\mathcal{L}_0}{\mathcal{L}_0+1}\frac{1}{1+i\omega\tau_2}\frac{1}{1+i\omega\tau_{\mathrm{eff}}}. \tag{4.118}$$

When the inverse Fourier transform is applied to Equation (4.118) and the output current is returned to the formula as the real space, the output current is expressed as

$$I(t) = \int_{-\infty}^{\infty} I(\omega)\mathrm{e}^{i\omega t}\mathrm{d}\omega, \tag{4.119}$$
$$= -\frac{E}{2\pi}\frac{1}{V_{\mathrm{b}}}\frac{\mathcal{L}_0}{\mathcal{L}_0+1}\int_{-\infty}^{\infty}\frac{1}{1+i\omega\tau_2}\frac{1}{1+i\omega\tau_{\mathrm{eff}}}\mathrm{e}^{i\omega t}\mathrm{d}\omega, \tag{4.120}$$
$$= \frac{E}{V_{\mathrm{b}}}\frac{\mathcal{L}_0}{\mathcal{L}_0+1}\frac{1}{\tau_{\mathrm{eff}}-\tau_2}\left(\exp\left(-\frac{t}{\tau_{\mathrm{eff}}}\right)-\exp\left(-\frac{t}{\tau_2}\right)\right). \tag{4.121}$$

The maximum value of the pulse height is obtained at the time t_{peak} represented as

$$t_{\mathrm{peak}} = \ln\frac{\tau_{\mathrm{eff}}}{\tau_2}\left(\frac{1}{\tau_2}-\frac{1}{\tau_{\mathrm{eff}}}\right)^{-1}. \tag{4.122}$$

Integrating Equation (4.121), the integral value of power becomes

$$\int V_{\mathrm{b}}I(t)dt = -\frac{\mathcal{L}_0}{\mathcal{L}_0+1}E, \tag{4.123}$$

and coincides with the X-ray energy in $\mathcal{L}_0 \gg 1$, which is the same as Equation (4.54).

4.7 Readout system with SQUID

The resistance change of the TES is about a few mΩ when an X-ray is incident in the TES, so an ammeter with a low impedance is needed to read out the small resistance change of the TES. Superconducting Quantum Interference Device (SQUID) is used as the ammeter. We measure the change in resistance using SQUID as shown in Figure 4.9.

4.7.1 dc-SQUID

SQUID is a device utilizing the Josephson effect, and it has a ring with two Josephson junctions in parallel like Figure 4.10. The relation between a phase difference $(\theta_2 - \theta_1)$ and a magnetic flux (Φ) that pierces the ring is described as

$$\theta_2 - \theta_1 = 2\pi\frac{\Phi}{\Phi_0}. \tag{4.124}$$

Φ_0 is a constant and called flux quantum, and the value is

$$\Phi_0 \equiv h/2e = 2.06 \times 10^{-15}\ \mathrm{Wb}. \tag{4.125}$$

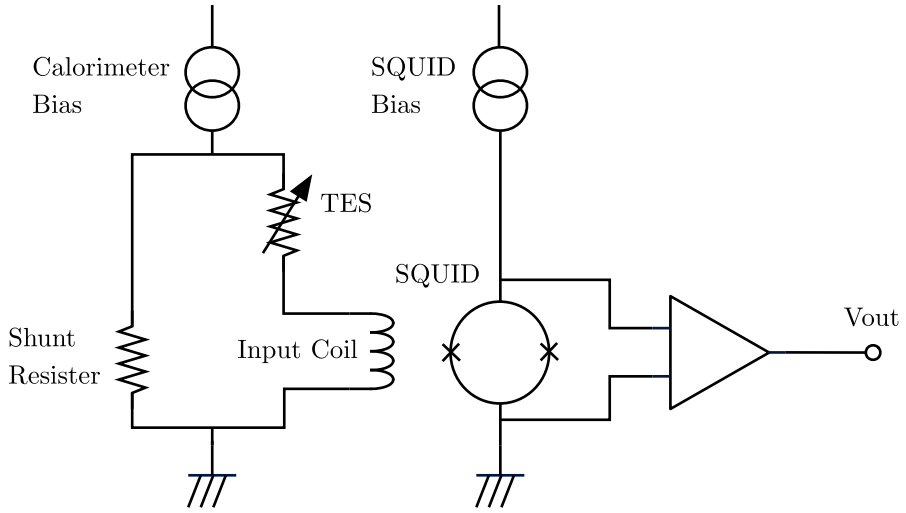

Fig. 4.9 Readout system for TES microcalorimeter using SQUID

Using the magnetic flux Φ, a self-inductance of the ring L, and a current circulating through the ring, we define an external magnetic flux ($\Phi_{\rm exp}$) as

$$\Phi_{\rm exp} \equiv \Phi - LJ. \tag{4.126}$$

Then, when the Josephson junctions are in the superconducting state, the biased current of SQUID ($I_{\mathbf{B}}$) is expressed using critical current I_0 of Josephson junctions and $\Phi_{\rm exp}$ as

$$I_{\rm B} = I_0 \cos\left(\pi \frac{\Phi_{\rm exp}}{\Phi_0}\right) \sin\left(\theta_1 - \pi \frac{\Phi_{\rm exp}}{\Phi_0}\right). \tag{4.127}$$

The maximum current at which the SQUID can maintain the superconducting state, which is the critical current of the SQUID is

$$I_c = 2I_0 \left|\cos\left(\pi \frac{\Phi_{\rm exp}}{\Phi_0}\right)\right|. \tag{4.128}$$

The critical current of the SQUID is changed by external magnetic fields.

4.7.2 Flux-Locked Loop

The response of SQUID is periodic as shown in Equation (4.127) and Equation (4.128). The amplification factor largely fluctuates depending on the position of the operating point, and the response becomes nonlinear. The outputs fold back according to the large inputs. To prevent these behaviors, SQUID is generally operated with a feedback and the magnetic flux penetrating the SQUID is kept constant. This feedback is called Flux-Locked Loop (FLL). The output of the SQUID is returned from a feedback coil magnetically coupled with the SQUID. The amount of feedback b is given by magnetic flux generated by feedback coil and output of the SQUID,

$$b = \frac{\Phi_{\rm FB}}{V_{\rm out}} = \frac{M_{\rm FB}}{R_{\rm FB}}. \tag{4.129}$$

$M_{\rm FB}$ and $R_{\rm FB}$ are a mutual inductance between the feedback coil and the SQUID and the resistance of feedback respectively. Then, a circuit gain of FLL becomes $1/b = R_{\rm FB}/M_{\rm FB}$. A magnetic flux generated by the current

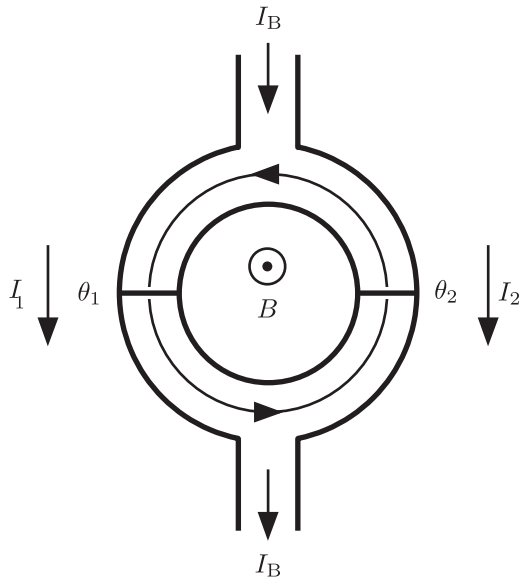

Fig. 4.10 A schematic diagram of dc-SQUID

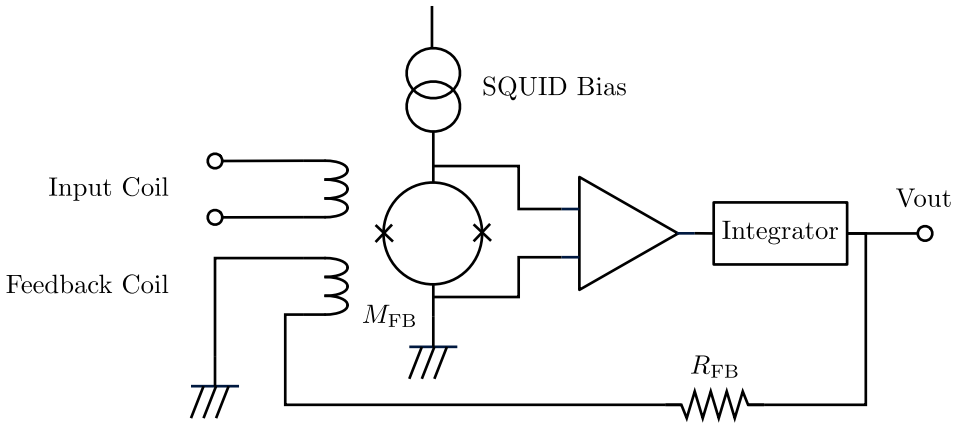

Fig. 4.11 Schematic diagram of FLL circuit

I_{in} going through the input coil is given by the input current I_{in} and the mutual inductance M_{in} between the input coil and the SQUID

$$\Phi_{in} = M_{in} I_{in}. \tag{4.130}$$

Then, a current-voltage conversion coefficient using the FLL circuit becomes

$$\Xi = \frac{M_{in}}{M_{FB}} R_{FB}. \tag{4.131}$$

Generally, the FLL circuit is used together with a lock-in amplifier, but this method makes the frequency band of the SQUID narrow. It is better to use SQUID-array for readout of the calorimeters.

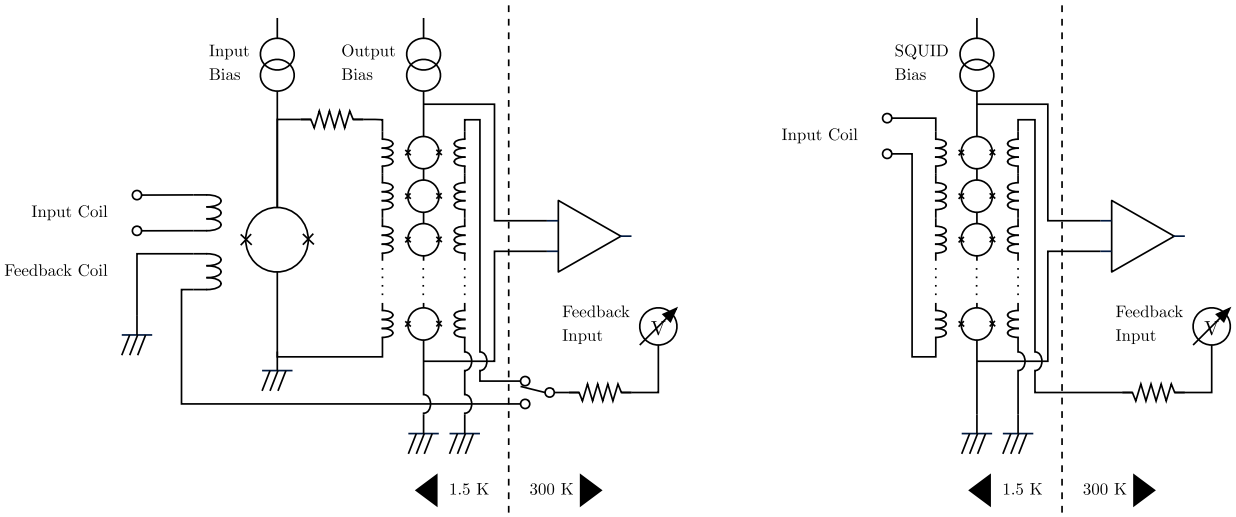

Fig. 4.12 Readout system for the calorimeter using SQUID-array: Two stage SQUID amplifier (left), and serial SQUID array (right)

4.7.3 SQUID-array

A large output is obtained because the outputs from individual SQUIDs are added, when dc-SQUID is operated with the same phase by connecting the SQUID in series. This is called dc-SQUID array. Connecting the SQUID in series makes impedance large. On the other hand, Connecting the SQUID in parallel makes impedance small due to the reduction of the self-inductance of input coil. A single SQUID cannot obtain the large output and the noise of the single SQUID is large, while connecting the SQUID can achieve a high gain and low noise level. There are two type of amplifier circuits which use a SQUID-array: one is Two Stage SQUID amplifier on the left side of Figure 4.12 and the other is Series SQUID Array (SSA) on the right side of Figure 4.12.

4.7.4 Contribution of SQUID noise to energy resolution of microcalorimeter

The noise equivalent power is given by the current density i_n of the SQUID and the current responsively S_I, and is expressed as

$$\mathrm{NEP}^2_{\mathrm{readout}} = \frac{i_n^2}{S_I^2}. \tag{4.132}$$

Using Equation (4.93), the contribution of SQUID noise to energy resolution of microcalorimeter $\Delta E_{\mathrm{SQUID-FWHM}}$ is calculated by the following formula:

$$\Delta E_{\mathrm{SQUID-FWHM}} = 2.35 \left(\int_0^\infty \frac{4df}{\mathrm{NEP}^2_{\mathrm{readout}}(f)} \right)^{-\frac{1}{2}}, \tag{4.133}$$

$$= 2.35 \frac{\mathcal{L}_0 + 1}{\mathcal{L}_0} |b| i_n \sqrt{\tau_{\mathrm{eff}}}, \tag{4.134}$$

$$= 2.35 \frac{\mathcal{L}_0 + 1}{\mathcal{L}_0} V_{\mathrm{b}} i_n \sqrt{\tau_{\mathrm{eff}}}. \tag{4.135}$$

In the case of a large loop gain ($\mathcal{L}_0 \gg 1$), $\Delta E_{\mathrm{SQUID-FWHM}}$ becomes

$$\Delta E_{\mathrm{SQUID-FWHM}} \sim 2.35 V_{\mathrm{b}} i_n \sqrt{\tau_{\mathrm{eff}}}. \tag{4.136}$$

4.7.5 SQUID Multiplexing

To readout the TES using the single SQUID, we generally need 4 pairs of electrical wires; one pair for the TES bias line, one for the SQUID feedback line, one for the SQUID bias line, and one for the SQUID output line. As the number of TES increases, the required number of SQUIDs increases, and the number of required wires also increases, eventually resulting in a non-negligible heat flow from the high temperature stage to the cryogenic stage. Furthermore, the heat of SQUID cannot be ignored. Therefore, the maximum number of SQUIDs that can be placed in the cold stage is generally limited by the cooling power of the stage and is usually less than 100 also by an optimistic estimation. For the readout of hundreds of TES channels, SQUID multiplexing is mandatory. There are three methods for TES signal multiplexing, such as a time division multiplexing (TDM), a code division multiplexing (CDM), and a frequency division multiplexing (FDM) [18].

TDM developed by Irwin et al. [7] is a system that sequentially turns on and off SQUIDs corresponding to inputs from each TES and reads a plurality of TES channels with one signal line while delimiting time. Multiplexing becomes possible if switching of the SQUID is performed sufficiently earlier than the time constant of the X-ray pulse signal. On the other hand, if the number of multiplexing is set to N, it is known that noise of SQUID deteriorates by $\sqrt{N}$ times by aliasing. In order not to deteriorate the resolution of TES, it is impossible to obtain a large number of multiplexing.

CDM is a method of multiplexing multiple TES channels by switching the SQUID which was done with TDM by using a Walsh code. Unlike TDM, concurrently, all the TES channels are conductive while the signs are different. Even with this method, SQUID noise deteriorates by $\sqrt{N}$ times due to noise aliasing of the SQUID. However, since all the TES channels are always conducting, the S/N ratio improves by $\sqrt{N}$ times, and the influence on the resolution by multiplexing disappears [3].

FDM is a system in which a plurality of TES channels are AC-driven at different frequencies, frequency modulation is applied, these signals are added and read with one SQUID. The added signal is demodulated at each driving frequency in the room temperature circuit, and signals of each channel are taken out. The modulation is sufficiently faster than the time constant of the X-ray pulse and modulation is performed at several hundred kHz to several MHz. In this method, SQUID noise aliasing does not occur, so there is no effect on resolution by multiplexing. However, it has been reported that the energy resolution is degraded by the influence of driving TES with AC bias [1].

Chapter 5

Development of TES X-ray microcalorimeter

5.1 Requirements for TES X-ray microcalorimeter

In STEM-EDS system, the TES X-ray microcalorimeter is required to have not only the high energy resolution but also the high count rate and the wide energy band as shown in Table 5.1. The ideal energy resolution of an X-ray microcalorimeter is determined by the Jonson noise of the thermometer and the thermal fluctuation noise of the calorimeter temperature which is caused by random thermal-energy flow between the thermal bath and the TES through the thermal link. It is described by

$$\Delta E_{\mathrm{FWHM}} = 2.35\xi\sqrt{k_{\mathrm{B}}T^2C}, \tag{5.1}$$

$$\xi = 2\sqrt{\frac{1}{\alpha\mathcal{L}_0}\sqrt{1+\alpha\mathcal{L}_0\Gamma}}. \tag{5.2}$$

When $\alpha >> 1$, $\xi \simeq 2\sqrt{\sqrt{n\Gamma}/\alpha}$,

$$\Delta E_{\mathrm{FWHM}} = 2.35\xi'\sqrt{\frac{k_{\mathrm{B}}T^2C}{\alpha}}. \tag{5.3}$$

From this equation, in order to achieve a high energy resolution, it is necessary to have low T and small C. And the count rate is decided by the pulse decay time which is described as $\tau_{\mathrm{eff}} \sim C/\alpha G$. In order to achieve a high count rate capability, it is necessary to make the decay time small. On the other hand, the maximum X-ray energy of a TES is decided by the saturation energy which is roughly approximated with $E_{\mathrm{sat}} \sim CT/\alpha$ and the stopping power of the absorber. Above the saturation energy, the energy resolution suddenly decreases. In order to achieve the wide energy band and high count rate, it is necessary to have large saturation energy and high stopping power. Therefore, the relationship between the energy resolution or the high count rate and the wide energy band is a trade-off. We need to optimize any parameters to achieve the requirements.

Table 5.1 Requirements for TES X-ray microcalorimeter

Item	Requirement	unit
Energy resolution	< 10	(eV)
Count rate	> 5000	(cps)
Energy range	$0.1 - 15$	(keV)

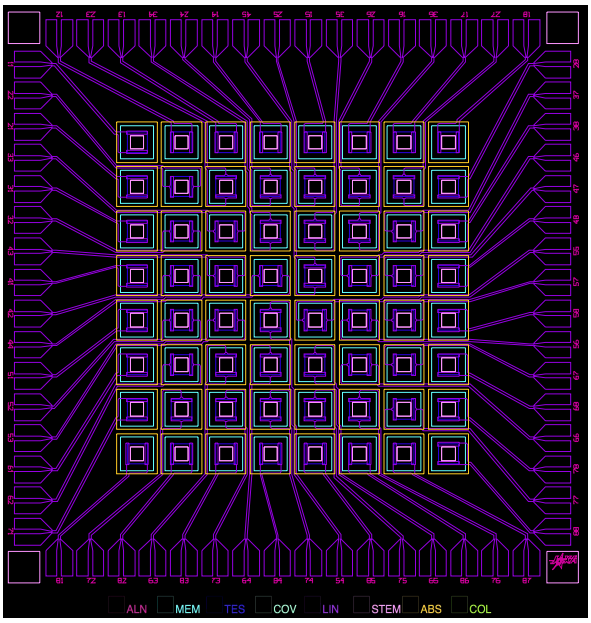

Fig. 5.1 CAD image of overview the TES chip

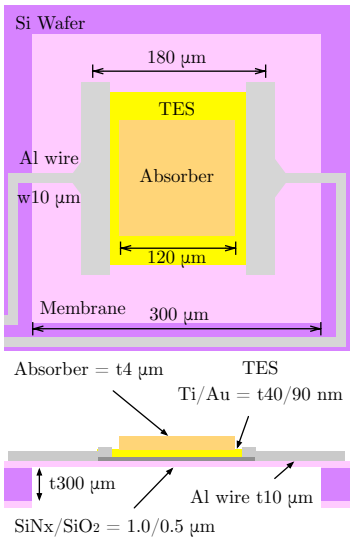

Fig. 5.2 Designs of one pixel TES

5.2 Parameter Optimizations and TES Designs

The design parameters of TES to control the performance are the TES size, the absorber volume, the membrane size, the membrane thickness and the superconducting transition temperature. For example, the TES has the bigger C to increase the TES size or the absorber volume, and the membrane size and thickness. The superconducting transition temperature affects G, and the superconducting transition temperature determines the operation temperature. However it is difficult to control α, which cannot be determined unless it is measured, but it is usually $50 \sim 100$. On the other hand, the TES size is greatly limited by the chip size and TES's mounting space. Among these limitations, we optimized T, C and G to choose the appropriate values for those design parameters. The most stringent requirement in STEM-TES-EDS system is applied for count rate. The maximum count rate per one pixel is about 200 cps, when the pulse decay time of TES is about 300 μs because it is necessary to take an interval of about 5 ms to next pulse so as not to degrade the energy resolution. We tried to overcome the problem with two approaches: by increasing the number of pixels of TES array and by making the pulse decay time shorter.

5.2.1 Geometry

We first assume that the maximum count rate per pixels is kept at 200 cps. Then we need 25 pixels to obtain 5 kcps. Allocating a margin of about factor 2, we decided to develop a 8×8 format, 64 pixel array. Our present pixel design requires about 350 μm pitches between pixels (Figure 5.2), thus an 8×8 array requires about 3×3 mm^2 area, We estimated that the spot size of the capillary optics is about 1 mm diameter, but that we can spread X-rays from the STEM over a 3×3 mm^2 area by defocusing the image. The chip size of the detector is limited by the cryogenic stage (see Chapter 6) and it must be smaller than 7×7 mm^2. Arranging the TESs, the membranes and the wirings, the TES chip size was designed within 5.2×5.2 mm^2 as shown in Figure 5.1. We allocated 128 bonding pads of 100 μm $\times$ 400 μm for TES. In addition we allocated four bonding pads at four corners for heat paths between the chip and the chip mount so that the temperature fluctuation of the chip is

Table 5.2 Details designed by TES, ↑ means the same as the above.

Design parameter	material	Item		unit
Chip	Si	Size	5.2×5.2	mm^2
TES	Ti/Au	↑	180×180	μm^2
		thickness	40/108	nm
Electrode wiring	Al	width	10	μm
		pitch	10	μm
		thickness	120	nm
Absorber	Au	Size	120×120	μm^2
		thickness	5	μm
Membrane	SiN_x	Size	300×300	μm^2

reduced.

5.2.2 Material of absorber

For the material of the absorber of the X-ray microcalorimeter, it is preferable that the heat capacity is small and the atomic number Z is large, because the energy resolution becomes better as the heat capacity is smaller from Equation (4.5), and the quantum efficiency of X rays is high as the atom number is large and the thickness of the absorber is large. Since the heat capacity increases when the absorber is thickened, there is a trade-off relationship between the heat capacity and the thickness of the absorber. When choosing the material of the absorber, three must be considered: a specific heat, a thermalization and a thermal diffusion. In order not to degrade the energy resolution by the thickness of the absorber, the specific heat should be small. If the thermalization and the thermal diffusion are slow, the heat escapes from the detector and the energy resolution becomes worse. Also, if the thermalization and the thermal diffusion process fluctuate due to the absorption position, the uneven waveform occurs for each event, and energy resolution is deteriorated. In order to make the thermalization and the thermal diffusion process uniform in the absorber, it is necessary that the thermalization and the thermal diffusion occur uniformly in the absorber before the energy moves to the TES. Thus, it is preferable that the material of the absorber has the large atomic number, the small specific heat, the high thermalization and the thermal diffusion. In many places, tin, bismuth, gold, copper and mercury tellurium are used as absorbers. We selected the absorber of gold, because we have successfully used it before [15].

5.2.3 Designs of the performance parameter

With 2-dimensional design fixed, the remaining design parameters are the thickness of the X-ray absorber and the transition temperature. With a thicker absorber, we obtain a better X-ray detection efficiency and higher saturation energy, thus, a wider energy range. However, the energy resolution will degraded and the X-ray pulse decay constant will be longer. On the other hand, with a higher transition temperature, we obtain a fast X-ray pulse but the energy resolution will be degraded. We estimated the dependencies of those four parameters on the absorber thickness and the transition parameters, and show them in Figures 5.3 - 5.6. In those figures we also show the target values that we would like to fulfill with some margins. For the pulse decay time (Figure 5.3) we have a margin of a factor of two. Thus if all 64 pixels are used, the maximum count rate will be about 20 kpcs. We find the most critical parameter is the saturation energy (Figure 5.5), and we could not allocate margin here. From those figures, we find a solution; a thickness of 5 μm and a transition temperature of 150 mK. The TES is a bilayer of titanium and gold, and the transition temperature of titanium (400 mK) is controlled by the proximity effect of gold. The minimum width and pitch of electrode wire for TES depends on the micro-process,

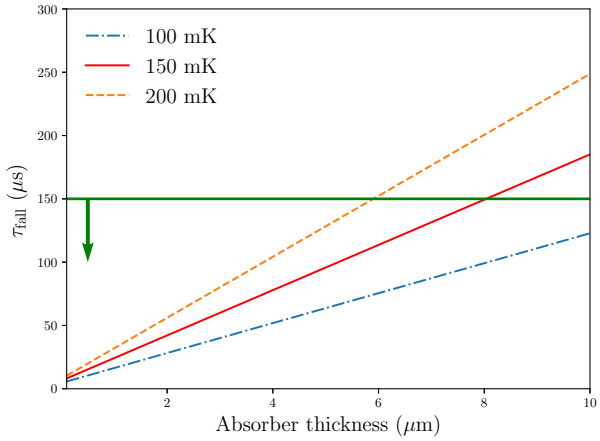

Fig. 5.3 Decay time vs. Absorber thickness

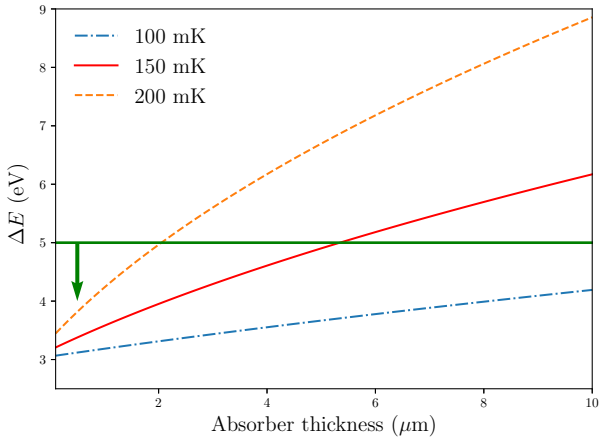

Fig. 5.4 Energy resolution vs. Absorber thickness

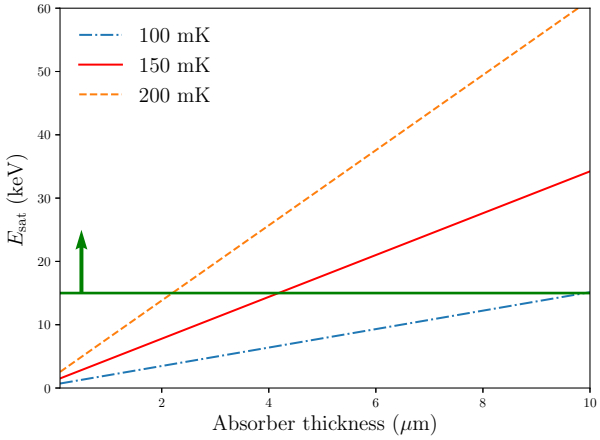

Fig. 5.5 Saturation energy vs. Absorber thickness

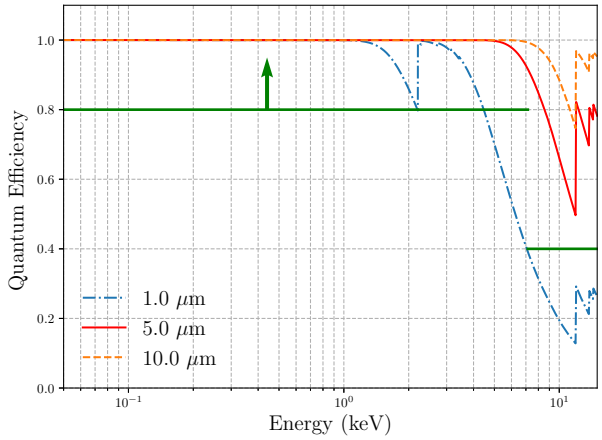

Fig. 5.6 Quantum Efficiency of each absorber thickness

and we selected the minimum width and pitch to 10 μm. Table 5.2 shows the result of designing the TES.

5.3 Optimization of fabrication process

The TES microcalorimeter is fabricated in-house, and Table 5.3 shows a fabrication process of the TES microcalorimeter. We have built the fabrication process with high yield rate and a uniform fabrication. For the first process, an alignment mark for the subsequent process is formed by RIE (Reactive Ion Etching) on the 4 inch silicon wafer. Then, the nitride film on the membrane pattern of the back side is removed by using RIE. It takes about one hour by an isotropic etching to remove the nitride film. Then a 4-inch wafer is cut into 4 pieces each of 35 mm^2, and the oxide film on the membrane pattern of the back side is removed by a hydrofluoric acid. Then, Ti/Au membrane is sputtered on the front side by DC magnetron sputtering. The target thicknesses of Ti and Au are 40 and 108 nm respectively. This Au thickness was selected so that the transition temperature becomes about 150 mK from the relationship between the transition temperature and Au thickness from the previous test fabrications. Ti/Au membrane is patterned by the wet-etching. In order to completely cover with Au, Ti over-etched for 3 hours. Al superconducting electrode/wiring is fabricated with a lift-off and etching mixed process. We first apply resist on a TES with contact area uncovered. The Al membrane is fabricated

Table 5.3 Fabrication process flow of TES microcalorimeter

#	Process	Method
1	Formation of alignment mark in 4 inch wafer	Dry-etching
2	Removal of SiO_2, SiN_x for formation of membrane	Dry-etching + Wet-etching
3	Dicing of 35 mm square	Dicing
4	Ti/Au sputtering (40/108 nm)	DC magnetron sputtering of Ti/Au
5	Formation of TES pattern	Wet-etching
6	Formation of TES protection resist pattern	
7	Al sputtering (120 nm)	RF sputtering of Al
8	Formation of wire pattern	Wet-etching + Lift-off
9	Formation of resist pattern of absorber	
10	Evaporation of Au of absorber (4.0 μm)	EB-evaporation
11	Formation of Absorber pattern	Lift-off
12	Formation of membrane on the backside, chips	Dry-etching

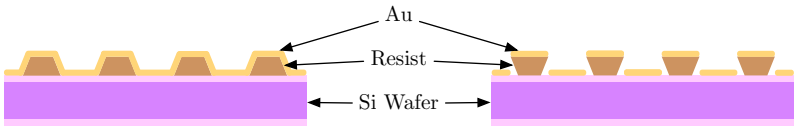

Fig. 5.7 Difference between positive photoresist (left) and negative photoresist (right) in lift-off process, which is a technique in which a metal is vapor-deposited on a pattern made of the photoresist, and then the photoresist is removed later, and a metal pattern remains only in a portion where there is no photoresist.

over the front side of the Si wafer with an RF (Radio Frequency) sputter. Then we protect electrodes with Al and remove Al with etching. The absorber is deposited on the TES by an evaporation process and formed by a lift-off process. Finally, a SiN_x/SiO_2 membrane structure which supports the TES and works as a thermal link to the Si substrate is formed by DRIE (Deep RIE). We arranged 9 chips described in Section 5.2 (Figure 5.1) at the center of 35 mm wafer with a 3×3 format. We thus fabricate eight TES microcalorimeter array chips and one evaluation chip with a single process. 9 chips are extracted from the 35 mm Si wafer using the same DRIE process to form the SiN_x/SiO_2 membrane. For fabrication, the 4 inch silicon wafer with a thickness of 300 μm and with attaching the silicon oxide and nitride ($SiN_x/SiO_2 = 1.0/0.5$ μm) films on a double sided was used. The membrane structure of TES microcalorimeter consists of a 1.0 μm thick nitride film. Its structure has an oxide film as a stopper when it is formed by DRIE of the final process. The silicon nitride is formed by Low Pressure Chemical Vapor Deposition (LPCVD).

In this fabrication process, two types of photoresist were used. Photoresist is a film which is sensitized and changed by UV light. There are two types of photoresist, positive type and negative type. The positive type resist is used in most of processes, whereas image-reversal-resist is a special type of negative resists. It is used for creating absorbers of 5 μm thickness. The absorber must be fabricated by lift off as shown in Figure 5.7 so that the process does not change the superconducting transition properties. It is not easy to form 5 μm structure with a lift off process. We tested many different resists and finally found that the image reversal resist is good for this process. Figure 5.8 shows the schematic view of image reversal resist.

Figure 5.9 shows the TES microcalorimeter chip that completed fabrication, and the micrograph is shown in Figure 5.10. The thickness of the gold absorber is 4.0 μm. The yield was confirmed, and one pixel out of 64 pixels was disconnected.

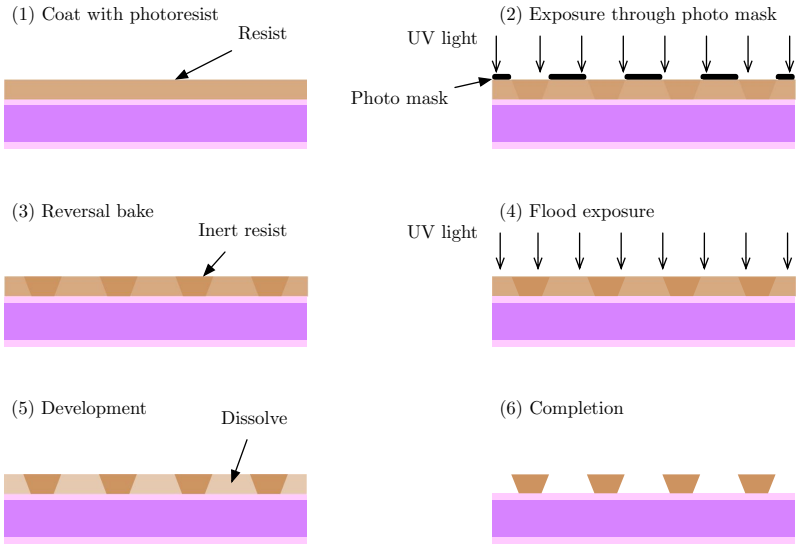

Fig. 5.8 Schematic view of image reversal resist

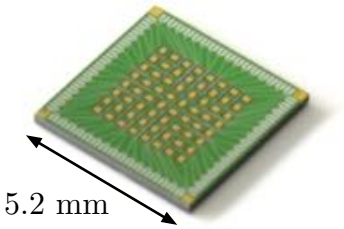

Fig. 5.9 8×8 TES array chip

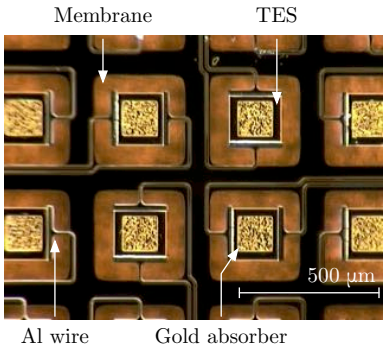

Fig. 5.10 Micrograph of TES microcalorimeter

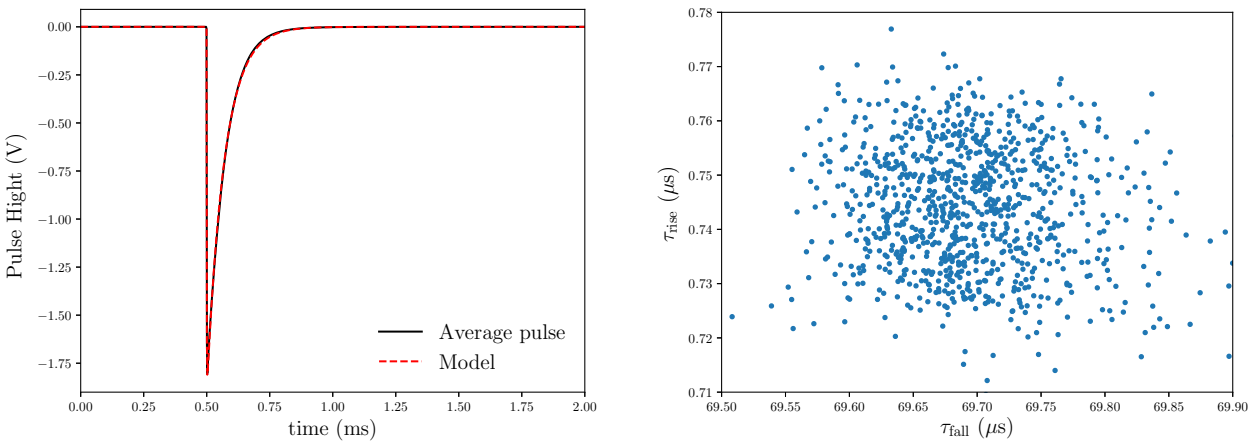

Fig. 5.11 Average pulse fitted by model (left), Distribution map of τ_{rise} vs. τ_{fall} at MnKα (right)

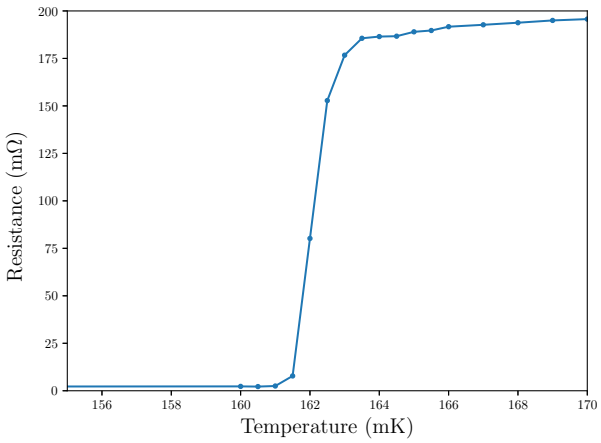

Fig. 5.12 Relationship between resistance and temperature of 1 pixel TES microcalorimeter, transition temperature T_c is 162 mK

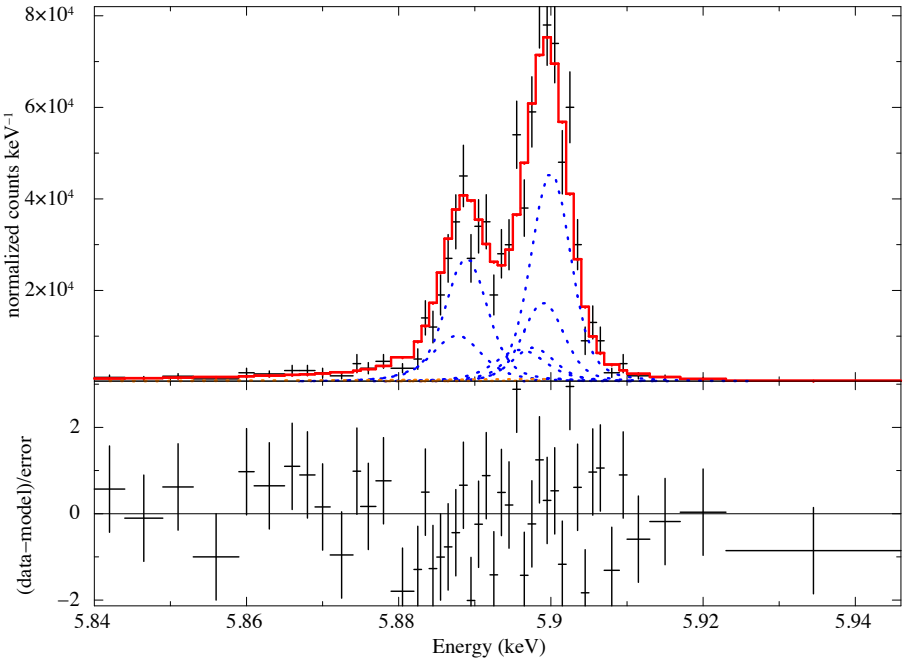

Fig. 5.13 Fit result at MnKα line

5.4 Evaluation and Performance

We confirmed the operation of the TES microcalorimeter fabricated in-house, and the two performances: the pulse decay time and the energy resolution. We performed an X-ray irradiation test. The dilution refrigerator was used, which has a lowest temperature of $\sim$ 50 mK in ISAS/JAXA. The TES chip was set on the cold stage. ^{55}Fe isotopes were mounted above the TES chip as X-ray sources. One 64-pixel array TES was voltage biased and lined to SQUID readout. We measured the TES resistance as a function of temperature at the cold stage, and confirmed the transition temperature (T_c) was 162 mK as shown in Figure 5.12. The bath temperature was set to 90 mK, with a TES bias current of 260 μA. We obtained an X-ray pulse at this operating point and measured the pulse decay time and the energy resolution. The pulse decay time is $\sim$ 70 μs and it was faster than

the general TES decay time as shown Figure 5.11. The energy resolution is $\Delta E = 4.89^{+0.58}_{-0.56}$ (eV), and it is less than 10 eV as shown in Figure 5.13. From the experimental results, the TES microcalorimeter was achieved as designed.

Chapter 6

Development of Detector Head for 64-pixel TES array

6.1 Requirements and Problems

However, the common bias tends to cause the electrical crosstalk. Therefor we performed crosstalk measurements to estimate the degradation of energy resolution, and found the degradation of the energy resolution is 0.6 eV at 5.9 keV [21].

The circuit diagram for reading the TES is shown in Figure 6.1. There are three parts: a TES chip, an SAA chip, a wiring on the stage which connects the TES chip and the SAA chip for reading TES. A shunt resistance for reading with constant voltage bias and a dumping inductance for slowing the rise time of the pulse are put on the SAA chip together with the SQUID and input coil (Figure 6.2). Finally they are separately prepared and usually connected by an Al wire bonding.

We read the signals from the 64-pixel array using 64 parallel signal chains with common TES and common SAA bias schemes, and we decided to mount both the TES microcalorimeter array and the 64 SAAs on the detector head in a 100 mK cryogenic stage so as to develop the detector head. However, the common bias tends to cause the electrical crosstalk. Therefor we performed crosstalk measurements to estimate the degradation of energy resolution, and found the degradation of the energy resolution is 0.6 eV at 5.9 keV [21]. The crosstalk has

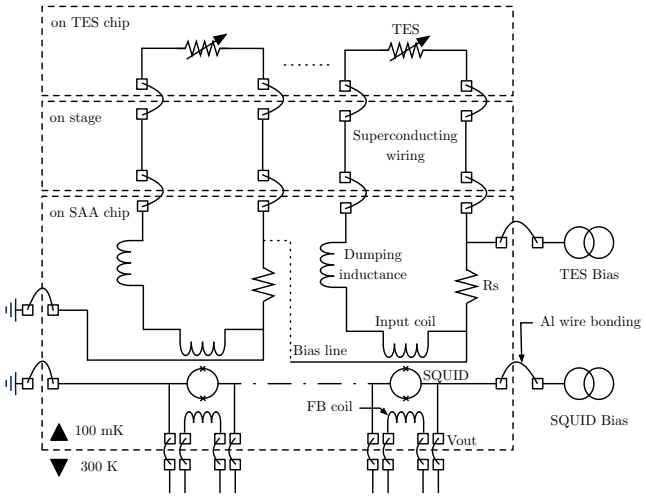

Fig. 6.1 Circuit diagram for reading the TES

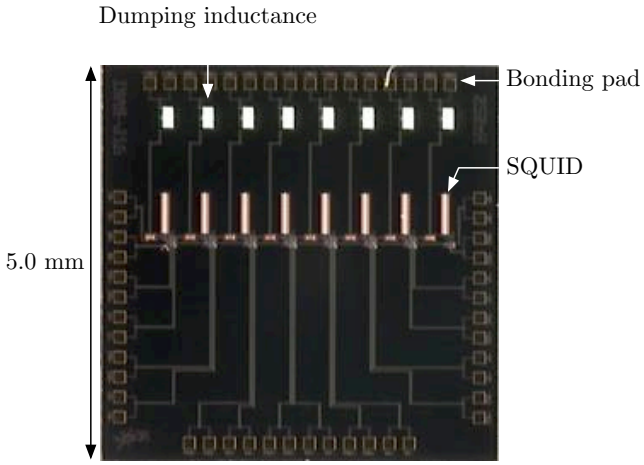

Fig. 6.2 SAA chip of J16 SQUID array

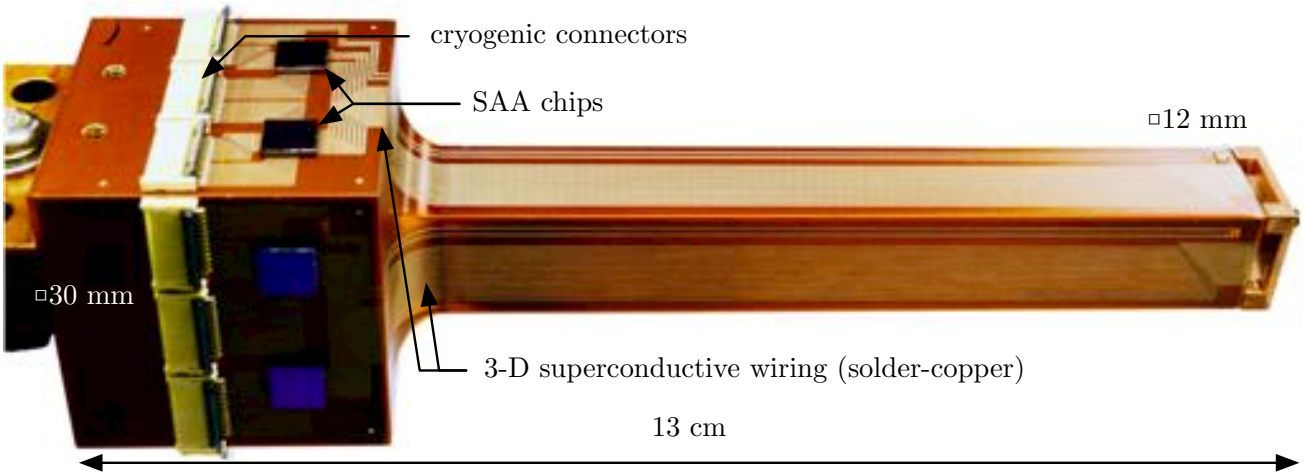

Fig. 6.3 Prototype of the detector head using the 3D superconductive wiring technology and superconductive flip chip bonding technology

little effect to energy resolution of this system.

The size and shape of the detector head is strongly constrained by the geometry of the STEM and the 100 mK refrigerator. We adopted a shape consisting of a 12 mm × 12 mm × 10 cm rod and a 30 mm cube at the bottom of the rod which were machined integrally from a single copper block, as shown in Figure 6.3. The 64-pixel TES array was mounted on top of the rod section, while the SAAs were mounted on the four surfaces of the cubic section. A connector to room-temperature electronics was also mounted on the cube surface. We adopted a three-dimensional superconductive wiring (solder-copper) technology (Figure 6.3, [17]) to connect the TES chip and SAAs chips. To connect the electrodes of TES and the SAAs with the superconducting wirings on the detector head with wire bondings only, we need 768 bondings, even though we adopted the common bias schemes. It is not impossible but not easy to connect 768 wire-bondings manually. Thus we adopted a superconducting flip-chip bonding to reduce the number of wire bondings [12].

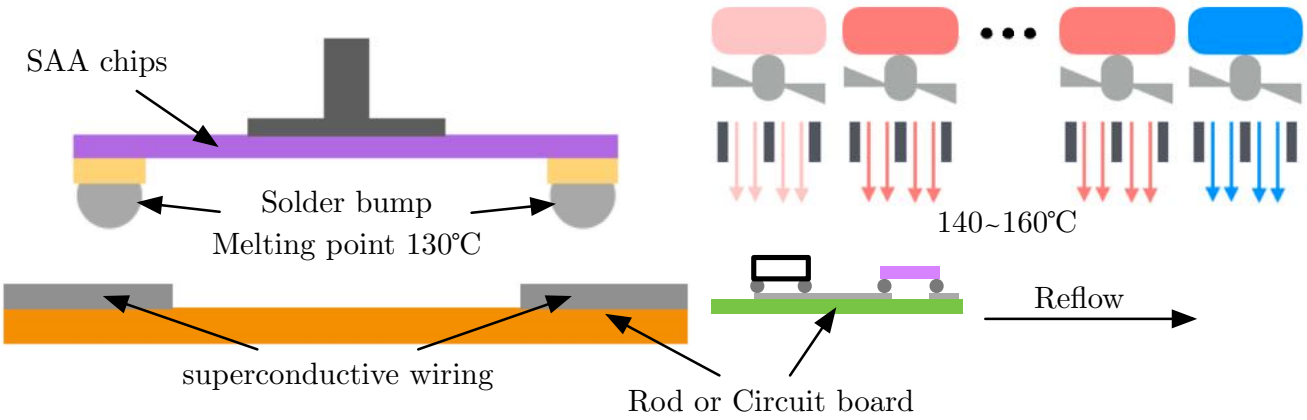

Fig. 6.4 Image aligned with flip-chip bonding to SAA chip and rod (left), Image of reflow (right)

6.2 The wire-bonding reduction technology

In order to make electrical connections among the TES, SQUID chips, and connectors to room temperature electronics, we usually use wire bondings. For the present detector head we need 768 bondings. In industry automatic wire bonders are used. This approach cannot be applied for the present rod structure, and wire bonding must be done manually. However the number of bondings is too large to perform without significant errors. Thus we decided to introduce a method to decrease the number of wire bondings. The flip-chip bonding allows us to connect the electrodes of the SAA to the superconducting wires without wire bonding. It forms a bump on the electrodes pad of the SAA, and contacts to pad of the superconducting wires. Then the whole assembly is heated as shown in Figure 6.4. In the first approach, we directly mounted SAA chips and cryogenic connectors on superconducting wires of the rod with the superconducting flip-chip bonding (Figure 6.3). The bump is a solder ball which is superconductive and melts at a temperature lower than that of the solder superconducting wires on the rod. The number of wire bondings reduces by approximately 80% using the flip-chip bonding. We encountered two problems. First, we need to mount SAA chips and connectors on four sides of the rod, however the flip chip bonding process shown in Figure 6.4 is applied to one surface only at the same time. Thus when we mount chips on the second and later surfaces, chips previously mounted must hung on the vertical and even up-side-down surfaces. This partly broke the connections. Secondly, some of the flip-chip-bondings were broken when we cool down the detector head to 4 K and below. In order to explore the causes of this problem, we performed a simple thermal simulation and identified the stress at the bump because of the different linear thermal expansion (LTE) coefficient of the SAA chips (Si) and the rod (Cu). To reduce stress at the bumps, and to avoid flip-chip-bonding process in vertical and up-side-down directions, we introduced a circuit board which is mounted on the rod and on which both the SAA chips and cryogenic connectors are mounted. The board-to-rod electrical connections are made by wire bondings. Thus we need additional 128 wire bondings.

6.3 Development of the circuit-board

The circuit-board material should have the LTE coefficient close to that of the SAA chips, and at the same time it should have a larger Young's modulus than that of copper so that it does not bend when the copper rod shrinks. We selected Sapphire for the material of the circuit-board (Table 6.1). The size of the circuit board is designed to be 30 mm $\times$ 23 mm in order to attach it to the 30 mm cube of the rod. We select 330 μm thickness of the

Table 6.1 Linear expansion coefficient and Young's modulus of materials

	Linear expansion coefficient at 25 ℃ μm/m · K	Young's modulus GPa
Cu	16.5	140
Si	2.6	100
FR4	21	20
Sapphire	7.0	470

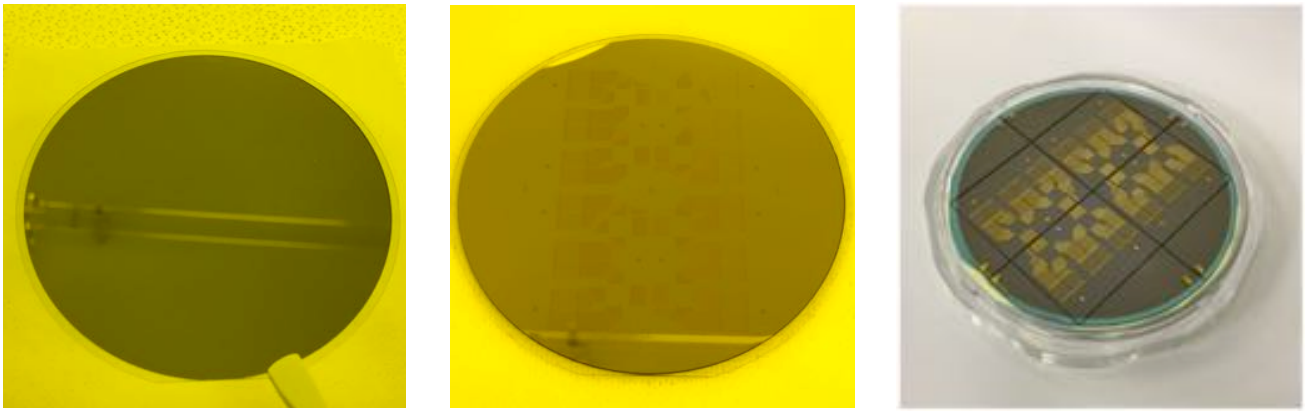

Fig. 6.5 Circuit board fabrication process, after film formation (left), pattern of wiring (center) and cutting by dicing (right)

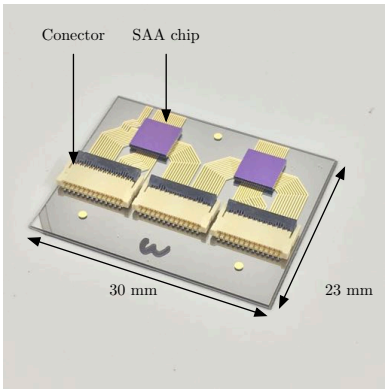

Fig. 6.6 Circuit Board of Sapphire

sapphire wafer. The configuration of the wiring is the same as that of the SQUID. The routing of the wiring was made close to the design on the rod as shown in Figure 6.5. On the back side, a heat path for uniformly diffusing heat was prepared with gold.

The process of fabrication of the circuit-board was as follows: first, we form Ti/Au (= 3/100 nm) as a layer that assists thermal diffusion on the backside. Then, the superconductive wiring is formed by multiple layers of Nb/Ti/Pd/Au (= 500/3/10/300 nm) on the other side and etched by the ion milling. Then a 3-inch wafer is cut into 4 pieces each of 30 mm × 23 mm. Finally two SAA chips and three cryogenic connectors were mounted to the circuit-board using superconducting flip-chip bonding (Figure 6.6). The circuit-board was designed in house. Since we selected Nb as the electrodes but we do not have Nb-process facility in house, we asked the fabrication to the CRAVITY (Clean room for analog & digital superconductivity) foundry service at AIST (national institute of advanced industrial science and technology). We asked a company to reflow flip-chip-bonding process. We used

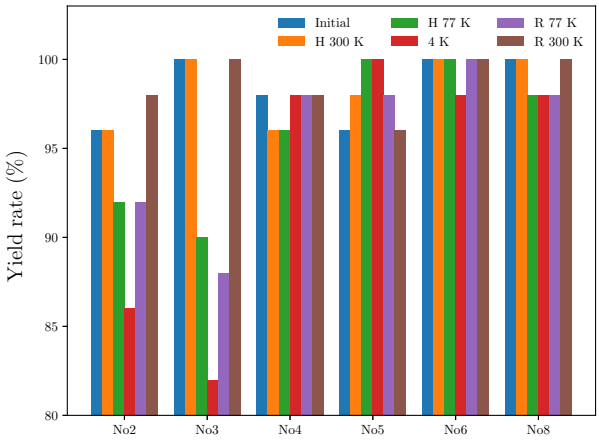

Fig. 6.7 Continuity test result of circuit-boards

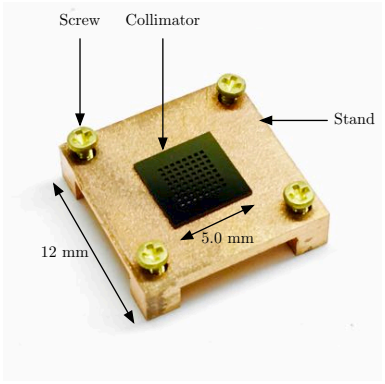

Fig. 6.8 Collimator and stand

a solder bump with a melting point of 130 C° and formed it on the superconductive wiring of the circuit-board. SAA chips and cryogenic connecters were bonded to the circuit board by reflow soldering. The start temperature of the reflow was set to 140 C° and the maximum temperature of the reflow was set to 160 C° with a margin.

We confirmed continuity of 204-pair wiring of six circuit-boards being fabricated in this way and a maximum yield rate was 98.0% at room temperature. In order to investigate the durability of flip-chip-bonding using sapphire board at low temperature, we tested the circuit-boards at between 300 K and 4 K. We used the dilution refrigerator which has the lowest temperature of $\sim$ 4 K in Kyusyu University. The yield rate was 93.0% at 4 K as shown in Figure 6.7.

6.4 Assembly of components

There are three components for the assembly on the rod: the TES chip (Figure 5.9), the four sapphire circuit-boards (Figure 6.6) and a collimator (Figure 6.8). The collimator, which is made of silicon with a thickness of 500 μm and whose hole size is 240 μm is used for preventing an incidence of X-rays into the TES chip substrate, because the X-ray incidence causes the noise of thermal fluctuation. The collimator is mounted on a stand of Cu. The installation process of three components was as follows: first, the TES chip is mounted on the top of the rod using a varnish to attach the top, and the wirings on the TES chip connected to the wirings on the top of the rod by 128 Al wire bondings. Then the sapphire circuit board is mounted on the cube side of the rod by

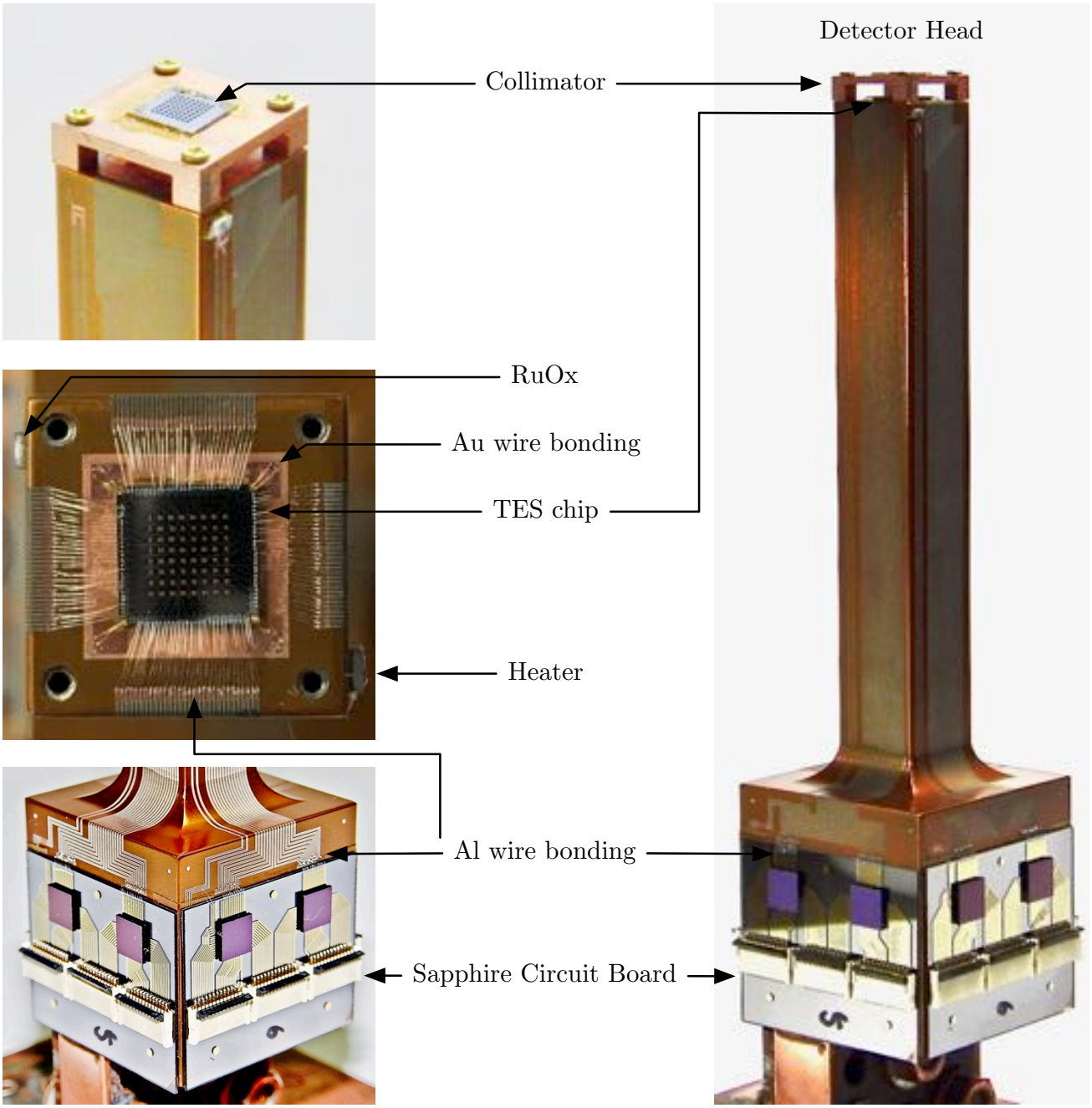

Fig. 6.9 Mounting to the detector head : collimator and stand (left top), TES chip (left center), circuit boards (left bottom), detector head (right)

the varnish, and the wirings on the sapphire circuit-boards connected to the wirings on the cube side of the rod by 128 Al wire bonding. Finally, the stand of the collimator is fixed to the top with screws, and it is fixed to the stand while aligning with an optical microscope. Figure 6.9 shows the photographs of the detector head after the assembly components. The Al wire bondings is about 67% smaller than the number required without flip-chip bondings. After installing the detector head on the STEM-EDS refrigerator, we confirmed a yield rate of 97.8% at 50 mK. By adopting superconducting flip-chip bondings on sapphire circuit-boards we reduce the number of wire bondings significantly.

Chapter 7

System Integration and Evaluation

7.1 System Integration

We described the development of the detector head in Chapter 5 and Chapter 6.

We installed the detector head on the STEM, and confirmed the operation as an STEM-TES-EDS System. The positional relationship between the detector head and the specimen in the STEM is schematically shown

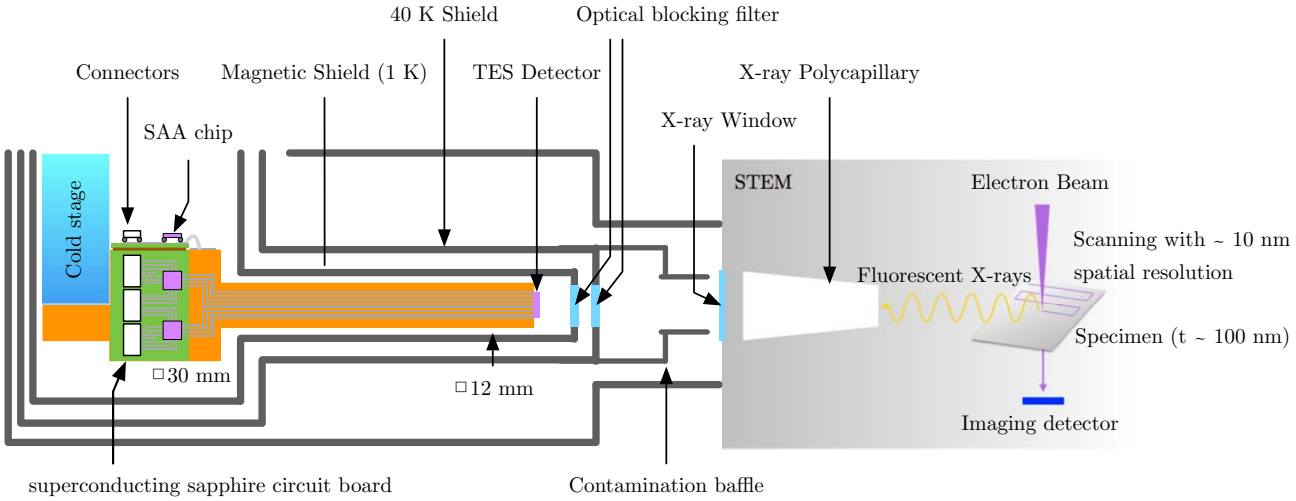

Fig. 7.1 Layout drawing of the detector head (same as Figure 3.3)

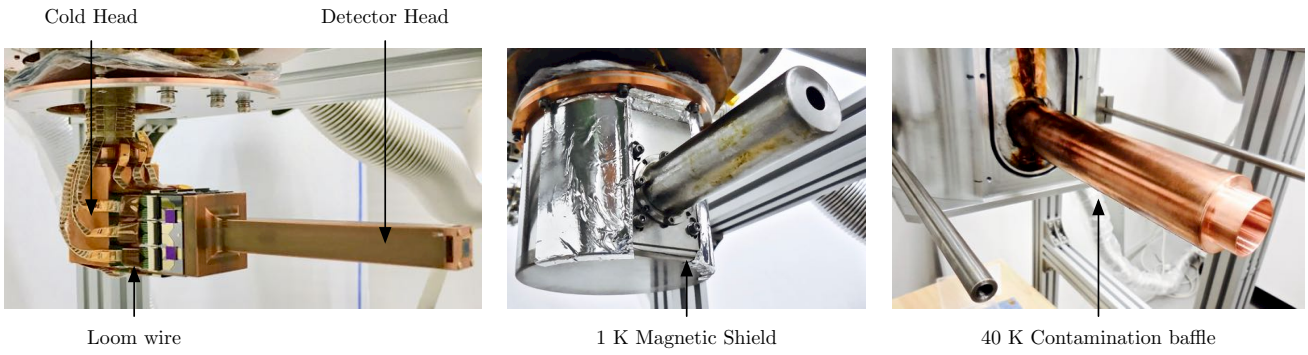

Fig. 7.2 Cold stage of the refrigerator and the detector head and the STEM (left), 1 K Magnetic Shield (center), 40 K Contamination baffle (right)

Table 7.1 Thickness of X-ray windows (Al/Polyimide) attached on each shield

	Al	Polyimide
1 K	100 nm	100 nm
40 K	100 nm	100 nm
Room Temperature (RT)	30 nm	350 nm

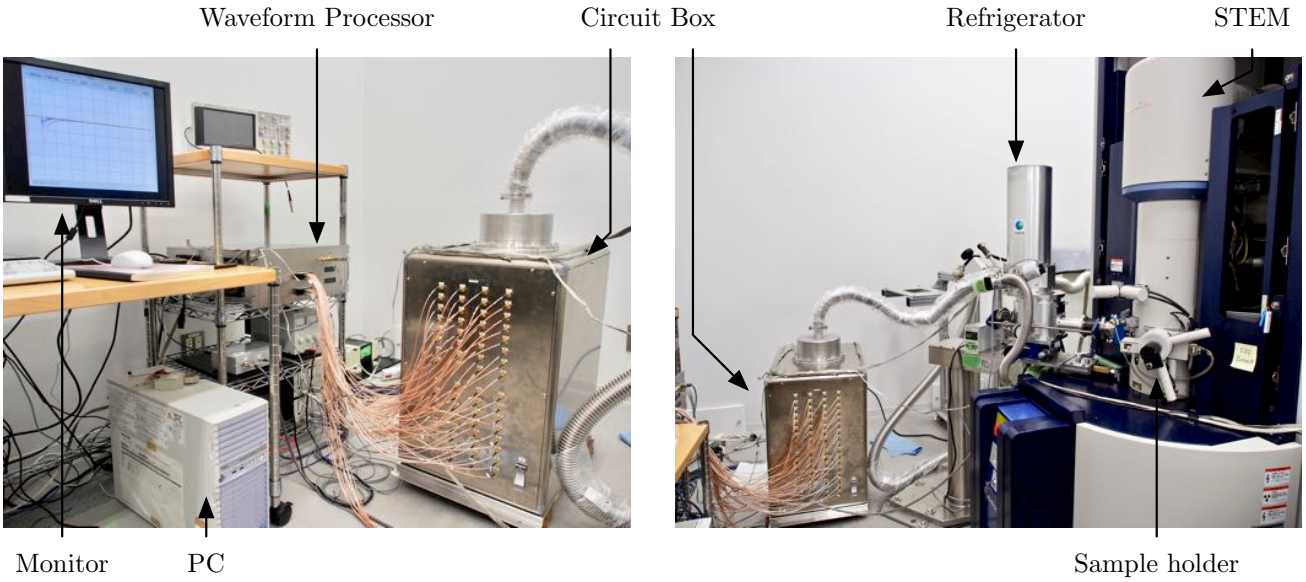

Fig. 7.3 External appearance of STEM-TES-EDS system

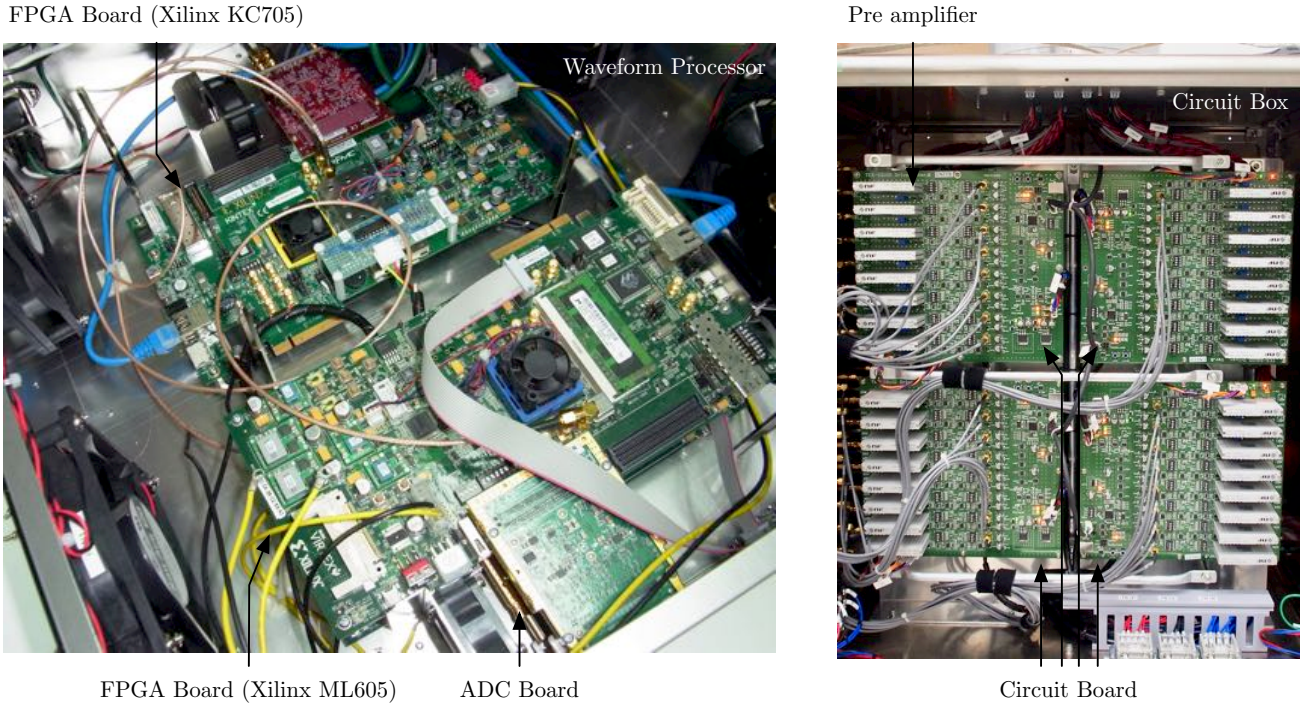

Fig. 7.4 Inside view of FPGA box (left) and Circuit box (right)

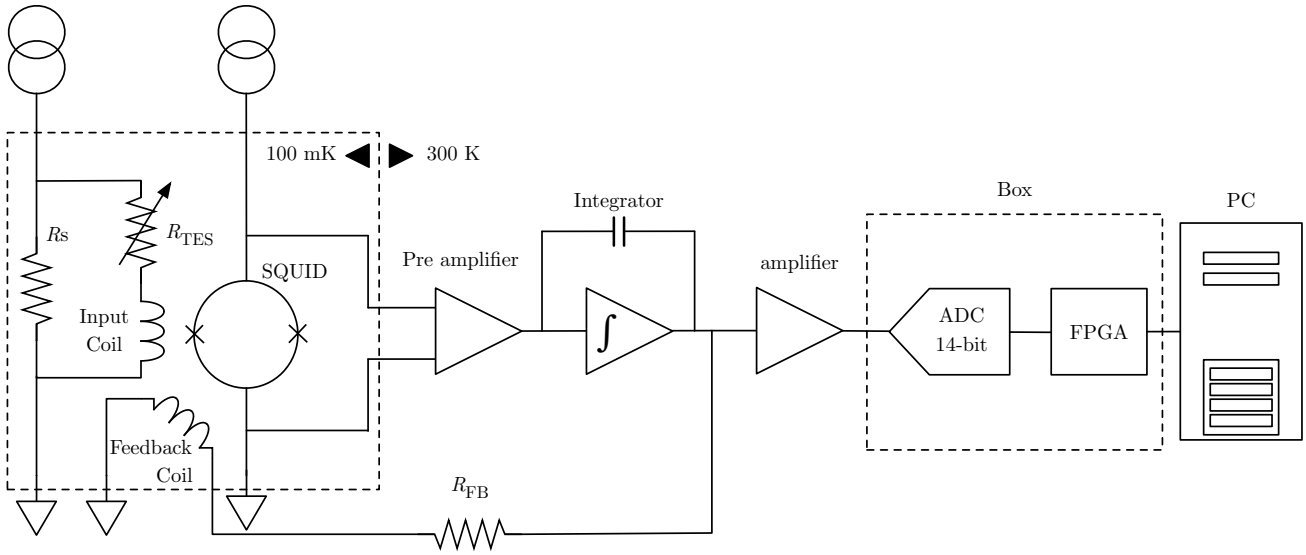

Fig. 7.5 Read out diagram

in Figure 7.1. When an electron beam is applied to the specimen, the fluorescent X-rays are emitted from the specimen. To increase the solid angle to collect X-rays, we use a poly capillary X-ray optics (Chapter 3). We have an X-ray window to separate the vacuum of the STEM and that of the 100 mK refrigerator. Then we have two optical blocking filters (OBF) on 40 K and 1 K thermal shields of the refrigerator, which prevent infrared photons of higher temperature stages from going inside the thermal shield. In Table 7.1 the materials used for the window and filters are summarized. Aluminum has a low emissivity and high reflectivity for infrared photons, and the low transmission. Using the absorption length in a literature, the transmission of Aluminum of a 100 nm thickness is estimated to be smaller than 10^{-5} for photons in a wavelength range of 400 - 900 nm [8].

Hydrocarbon molecules are emitted from the surface of room temperature vacuum shell of the refrigerator. They stick on the surface of 40 K shell including the 40 K OBF, which can reduce the low energy X-ray transmission. In order to reduce the contamination, we installed a 40 K contamination baffle as shown in Figure 7.1 and Figure 7.2 (right). The 1 K shield is made of high permeability material, A4K (Figure 7.2 center), from Amuneal Manufacturing Corporation, and thus it works as a magnetic shield for TESs. The 40K shield is made of copper and provides uniform thermal environment for the lower temperature stages. The detector head is mounted on 100 mK stage. For wire harnesses from room temperature to 100 mK stages, we use cryogenic woven loom wires from the CMR company. A cryogenic woven loom wire contains 12 twisted pairs of electric wires woven with PEEK yarn and we use eight loom wires from the detector head to room temperature. The wires consist of two parts. From 100 mK to 4 K we use loom wires with Nb/Ti, while those from 4 K to room temperature use constantan. All wires are equipped with connectors at both ends, and at 4 K stage we have relay connectors.

Figure 7.5 shows the overall block diagram to read out the signal. The analog signals from the SAAs are transmitted to the ADC (Analog Digital Converter) through a drive-circuit-unit which includes a preamplifier, an integrator, a flux-lock-loop feed-back resister and a post amplifier. The analog signal is converted into a digital signal by the ADC and sent to the FPGA (Field-Programmable Gate Array) (Figure 7.4 left). The driver-circuit-unit which is in the circuit box (Figure 7.4 right) and ADC are connected by using the SMA (Sub Miniature Type A) connectors. ADC and FPGA are connected by using FMC-HPC. FPGA and PC are connected by using GbE (Gigabit Ethernet). To control the drive-circuit-unit, the PC is connected to the drive-circuit-unit by UART of USB connection. The STEM electron beam is controlled by other FPGA which also captures a STEM-Image.

As the ADC board, we selected the Nutaq MI125 board, which satisfies the sampling rate, the bit resolution

Table 7.2 Units and channels of SAAs and TES which are confirmed operation, 'S' : SAAs, 'circle' : the operable 'B' : no response to the TES bias variation

	Unit1		Unit2		Unit3		Unit4		Unit5		Unit6		Unit7		Unit8	
ch	S	TES	S	TES	S	TES	S	TES	S	TES	S	TES	S	TES	S	TES
1	○	○	○	B	○		○		○	○	○	○	○	○	○	B
2	○	○	○	B	○		○		○	○	○	B	○	○	○	○
3	○	○	○	○	○				○	○					○	○
4	○	○	○	○	○										○	○
5	○	○	○	○	○										○	○
6	○	○	○	B	○											
7	○	B			○											
8	-	-			-	-			-	-			-	-		

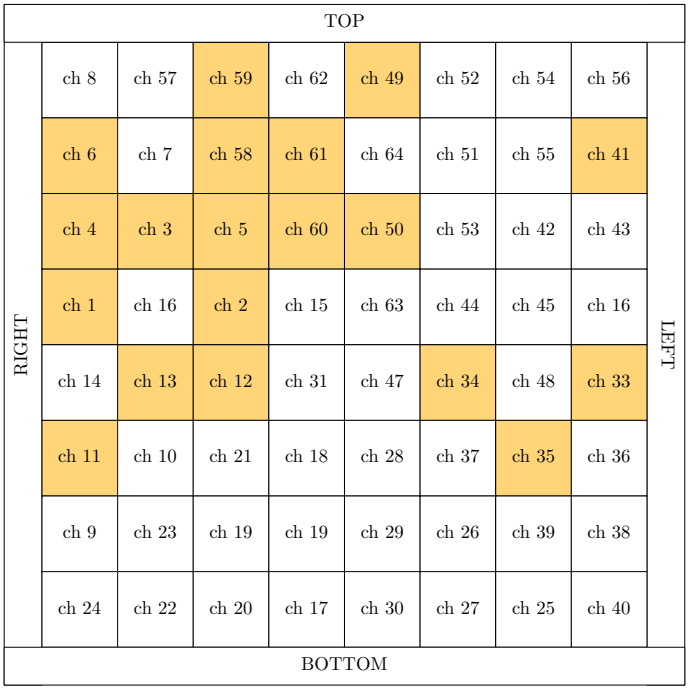

Fig. 7.6 Channel map on the TES chip chip. Colored channels are in operation.

and the input voltage range requirements with 125 Msps, 14-bit and 2 V_{pp}, respectively. The number of input channels is 32 channels, and two ADC boards are prepared to read 64 channels. As the FPGA for the waveform processing, we selected the Xilinx ML605. For the beam control, FPGA is the Xilinx KC705. Although the systems inside the three FPGA boards (ML605×2 and KC705) are driven by independent clocks, in order to share the beam control position, the reference clock output from the KC705 (50 MHz) is supplied to two ML605. In the FPGA, the signal captured by the ADC is decimated to 1/128 (This corresponds to thinning the sampling rate to 125/128 Msps.). The software on the Xilinx ML605 FPGA first identifies an X-ray pulse event, then the pulse record is stored in a onboard memory and transferred to PC for further pulse shape analysis. Figure 7.3 shows that the external appearance of the STEM-TES-EDS system includes STEM, refrigerator, sample holder, circuit box, waveform processor, PC, and monitor.

7.2 Evaluation of performance

In the first cool down test of the detector head, the bath temperature was set to 90 mK because the TES transition temperature was 160 mK. Then we checked the Φ–V curves of the SAAs, and found that only 34 SAAs out of 64 were properly operating (see Appendix C). Then we turned on the TES bias currents and found only 19 TES pixels were operating. In Table 7.2 and Figure 7.6 we summarized the TES channels we could confirm the performance. No TES was operating for units 3 and 4. For these units, when we turned on the TES bias, a temperature increase of the stage was observed. This suggests that the bias current went through a normal resistance instead of TES. For other units, there are channels for which SAA was operating but TES was not. These channels are marked with "B" in Table 7.2. Further tests were performed only on these 19 pixels.

7.3 Experiments under the high counting rate

7.3.1 Objectives

To evaluate the TES behavior under a high count rate environment, and to confirm 5 kcps count rate capability and an energy resolution better than 10 eV, we have performed a radiation test using the developed STEM-TES-EDS system.

7.3.2 Trigger methods

We used Al sample with 0.1% of Si included. We detected an Al K emission line spectrum with the TES device. The sample was irradiated with 200 keV electron beam from STEM and was adjusted an aperture size of the electron beam to obtain a different data of count rate. There are four aperture sizes in the STEM, which we call 'AP1', 'AP2', 'AP3', 'AP4'. The aperture size decreases as the 'AP number' increases and thus the count rate decreases.

We obtained X-ray pulse records with two types of data acquisition methods: a trigger mode and a through mode. When the aperture size was adjusted to 'AP3' and 'AP4', we acquired the pulse using the trigger mode. In order to detect X-ray events, the second derivative of the time series data x_i of the voltage value is calculated, when the derivative exceeds a threshold value, an event trigger is on and an X-ray pulse is considered to be detected, as follows:

$$x_i - 2x_{i-1} + x_{i-2} > \text{Threshold}. \tag{7.1}$$

A pulse record consists of 2000 ADC samples, among which 200 are before the trigger point and remaining 1800 are after the trigger point. A data length was fixed at 2 ms, and we took the first half 1 ms as the pulse data and the second half 1 ms as the noise data. When the aperture size was adjusted to 'AP1' and 'AP2', we acquired the pulse using the through mode. In this mode, all the data for a certain period is saved. We can apply the event detection analysis to the stored data on non-real time bases. It is possible to use time intervals where the pulse does not exist as the noise. In through mode, pulses were extracted according to the following procedure:

1. Calculating the second derivative of all data
2. Setting a flag at the time when the threshold is exceeded
3. Check the time interval for adjacent flags
4. Set the flag to True, if its time interval is longer than the specified length
5. Cut out the specified length at a ratio of 1 to 9 before and after the True flag

In this method, it is possible to take a pure pulse that is not affected by double events. Optimum filter was calculated by using pulse and noise records, then the optimum filter was applied to each pulse record. It then becomes the PHA (Pulse Height Analyzed value by optimum filtering). For conversion from the PHA to the energy equivalent value which we call PI (Pulse Invariant), we used a quadratic function with a constraint that $PHA = 0$ with $E = 0$,

$$PHA = aE^2 + bE, \tag{7.2}$$

fitting to the Al Kα line and Al Kβ line, we obtained the energy E as

$$E\left(PHA\right) = \frac{-b + \sqrt{b^2 - 4aPHA}}{2a}. \tag{7.3}$$

7.3.3 Spectrum analysis

In order to confirm relation between the count rate and the energy resolution, we got data under the four different aperture sizes and analyzed three types of data lengths as shown in Table 7.3. We counted the number of photons incident on TES of 19 pixels between $0.5 - 15$ keV, and calculated the count rate with the exposure time.

To calculate the energy resolution of Al Kα line (1486 eV), we cut out the spectrum in the energy range from $\sim$ 1460 eV to $\sim$ 1530 eV. The emission consists of fine structure and we need to take them into account. Thus as the line model, we use the following model function:

$$F\left(E\right) = N \sum_{i=1}^{n} \sum_{j} G\left(E - E_j, \sigma\right) r_i L\left(E_j, E_{c,i}, \Gamma_i\right), \tag{7.4}$$

where L and E are Lorentzian function and photon energy, respectively. n is the number of fine-structure lines, and r_i, $E_{c,i}$ and Γ_i are the relative intensity, the centroid energy and the natural width of the i th fine structure line respectively. The energy spectrum is described with the convolution of the line spread function which is approximated with a Gaussian function G. Then the Full Width Half Maximum (FWHM) is given by $\sqrt{2\log 2}\sigma$, where σ is the standard deviation of a Gaussian function. We show the details of the fine structure of Al Kα line in Table A.1.

From the residual (=data - model) of the only line model fitting, we found that the energy spectrum contains an excess in the low energy tail as a part of line spread function. Thus we added the following term in the model function;

$$F_{\mathrm{tail}}\left(E\right) = u \sum_{i=1}^{n} r_i \exp\left(-\frac{E_i - E}{w}\right) \theta\left(Ei - E\right), \tag{7.5}$$

where $\theta\left(E\right)$ is the step function, i.e. $\theta = 1$ for $E \geq 0$ and $\theta\left(E\right) = 0$ for $E < 0$. u and w as free parameters (subsection 8.1.2). Moreover we added a constant model for a continuous component.

We fitted the model with N (a normalization factor), σ, u, w as the free parameters by using the maximum likelihood method assuming the Poisson statistics. The statistical errors of the fit parameters were estimated using so-called C-statistics. We define $C = -2\ln\mathcal{L}$, where $\mathcal{L}$ is the likelihood. $\Delta C = C_{\mathrm{true}} - C_{\mathrm{min}}$ follows χ^2 distribution with the degrees of freedom. The errors of this result are estimated by the single parameter errors at a 90% confidence level, which corresponds to $\Delta C = 2.701$ [15].

Table 7.3 Obtainment terms of each count rate.

Aperture size	Trigger mode	Data Length (μs)	total count (count)	Exposure time (s)	throughput rate (cps)	ΔE_{FWHM} (eV)
AP4	Trigger	1000	249817	7200	35	6.84 ± 0.04
AP3	↑	↑	638938	1800	354	6.98 ± 0.03
AP2	Through	↑	181023	120	1509	7.17 ± 0.06
AP1	↑	↑	135122	60	2252	8.50 ± 0.09
AP1	↑	250	271415	↑	4524	9.51 ± 0.08
AP1	↑	150	302464	↑	5041	10.97 ± 0.10

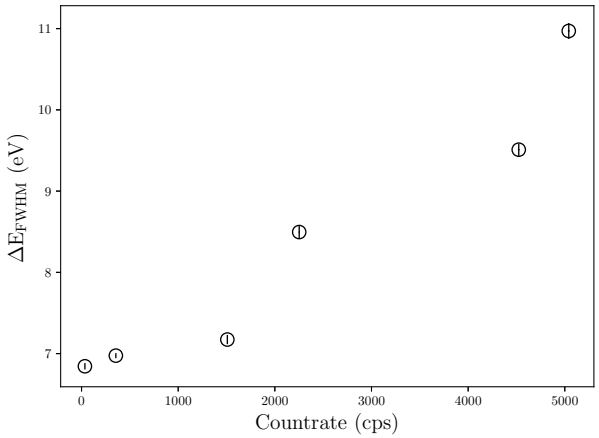

Fig. 7.7 Count rate vs. Energy resolution

7.3.4 Result

In Table 7.3 and Figure 7.8–7.13, we show the best fit values of the energy resolution (FWHM) and the spectrum of Al Kα line. Figure 7.7 shows the relation between the count rate and the energy resolution. We find the maximum counting rate requirement (5 kcps) and energy resolution requirement (10 eV) are simultaneously satisfied.

7.4 Low energy response

7.4.1 Object and Setup

The energy range of the TES EDS system is determined by two factors: the efficiency of the TES microcalorimeter and the transmission of the X-ray window and OBFs. The low energy efficiency could be largely affected if significant thickness of contamination builds up on OBFs. We thus tested low energy response of the TES EDS.

In this test, we decided to use specimen taken from one of our TES device. This sample has a layer structure and is a thin film processed by FIB as shown in Figure 7.14. This sample was radiated with the wide energy range X-ray of Carbon (C Kα : 0.281 eV), Nitrogen (N Kα : 0.394 keV), Oxygen (O Kα : 0.525 keV), Silicon (Si Kα : 1.739 keV), Titanium (Ti Kα : 4.508 keV), and Gold (Au Lα : 9.712 keV).

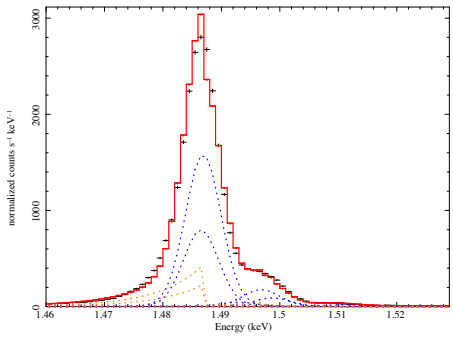

Fig. 7.8 Combined spectrum from all TESs hooked up @AP4, Data Length = 1 ms, $\Delta E_{\mathrm{FWHM}} = 6.84$ eV

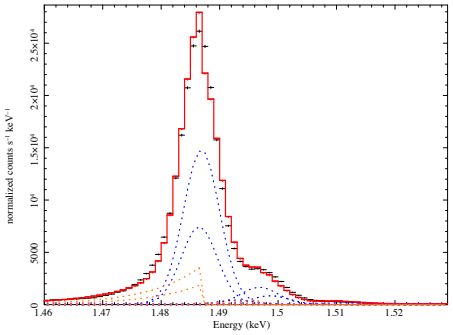

Fig. 7.9 Combined spectrum from all TESs hooked up @AP3, Data Length = 1 ms, $\Delta E_{\mathrm{FWHM}} = 6.98$ eV

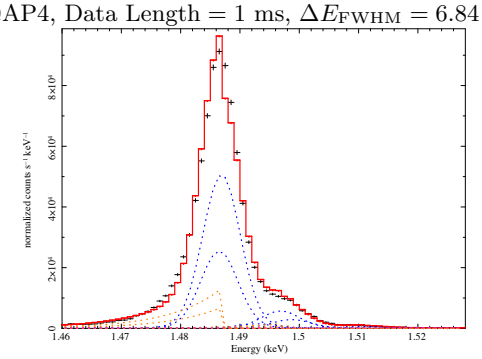

Fig. 7.10 Combined spectrum from all TESs hooked up @AP2, Data Length = 1 ms, $\Delta E_{\mathrm{FWHM}} = 7.17$ eV

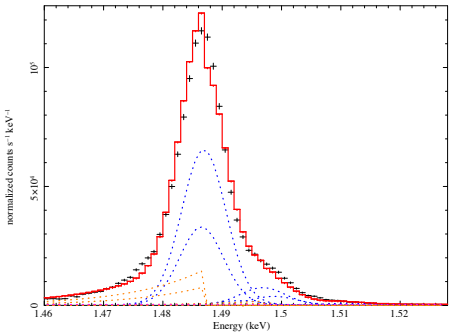

Fig. 7.11 Combined spectrum from all TESs hooked up @AP1, Data Length = 1 ms, $\Delta E_{\mathrm{FWHM}} = 8.50$ eV

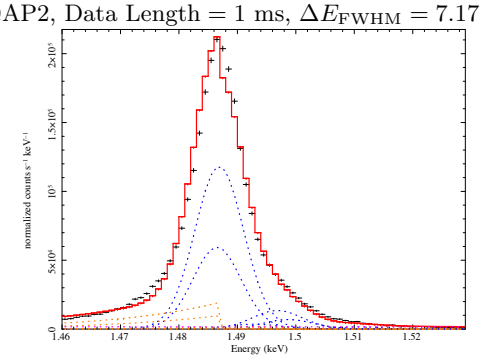

Fig. 7.12 Combined spectrum from all TESs hooked up @AP1, Data Length = 250 μs, $\Delta E_{\mathrm{FWHM}} = 9.51$ eV

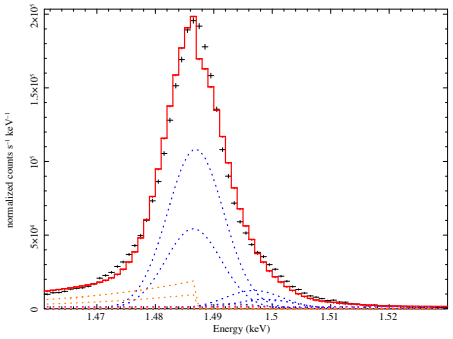

Fig. 7.13 Combined spectrum from all TESs hooked up @AP1, Data Length = 150 μs, $\Delta E_{\mathrm{FWHM}} = 10.97$ eV

Table 7.4 Experiment condition to confirm the energy range

Apeture size	mode	Data Length (μs)	Exposure time (s)	Total count (count)	Unused channel
AP1	Trigger	1000	3600	436484	ch 59

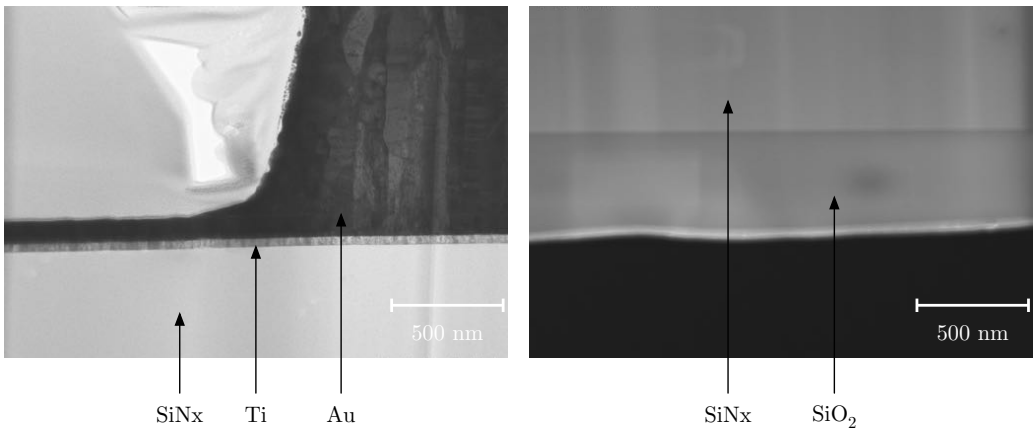

Fig. 7.14 TEM image of the TES surface (left), Below the image on the left (right)

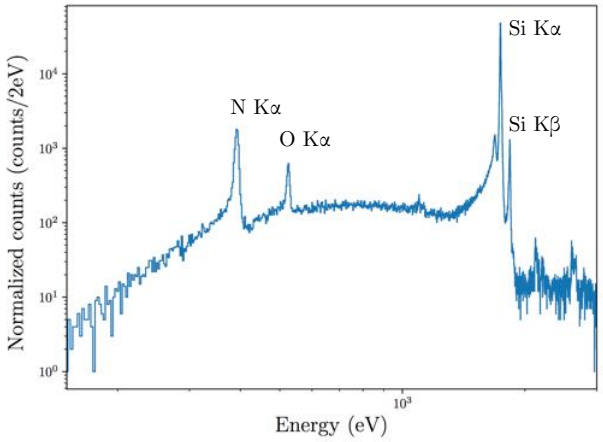

Fig. 7.15 Energy spectrum from the sample of SiN_x/SiO_2

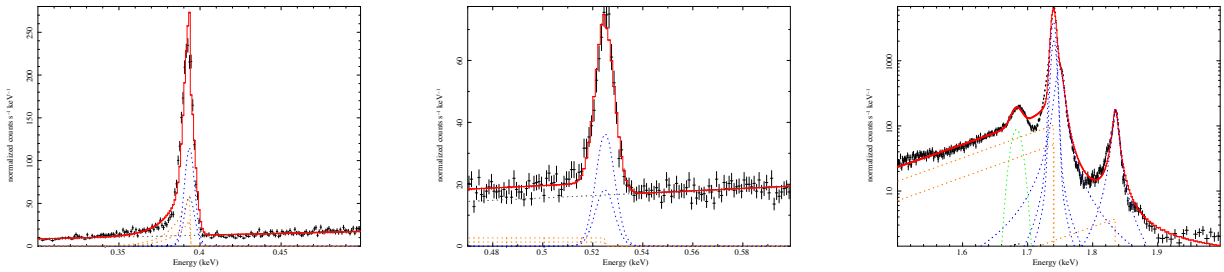

Fig. 7.16 Fit result of each emission line, N Kα (left), O Kα (middle) and Si Kα (right)

7.4.2 Result

An electron beam was applied to the Carbon film which is the SiO_2/SiN_x film which is a membrane of TES to obtain an X-ray spectrum. The measurement conditions are shown in the Table 7.4. Ch 59 was not used because FLL flew midway and energy calibration was misplaced. The figure of 0.15 to 3.0 keV of the obtained spectrum is shown in Figure 7.15. Figure 7.16 shows the fitting result of each emission line, and the emission lines were obtained with the energy range above 0.3 keV.

Chapter 8

Construction and Experiment towards Quantitative Analysis

8.1 Construction of Response function

Our final goal is to estimate the emission line intensity with systematic errors as small as possible. As we discussed in Chapter 2, the top hat filter method introduces uncontrollable systematic errors due to overlap of adjacent lines and continuum emission. This is true even when we improve the energy resolution with TES. In X-ray astronomy a forward method, i.e. a model fitting is widely used. XSPEC is one of the software used for spectral fits in X-ray astronomy. Suppose $\mathcal{M}(E_i)$ is the energy spectrum of the incident X-rays, the spectrum obtained by an X-ray detector $\mathcal{D}(PI_j)$ (count cm^{-2} s^{-1}) is given by

$$\mathcal{D}(PI_j) = \sum_{i=1}^{m} \triangle E_i \cdot \mathcal{S} \cdot \mathcal{ARF}(E_i) \cdot \mathcal{R}(E_i, PI_j) \cdot \mathcal{M}(E_i), \tag{8.1}$$

where $\mathcal{S}$ is the detector effective area (cm^2) of collecting solid angle (in STEM case), $\mathcal{ARF}(E_i)$ is the detection efficiency, and $\mathcal{R}(E_i, PI_j)$ is the detector's response function. $\mathcal{D}(PI_j)$ is given by integrating over energy E. In Equation (8.1) the integration is expressed in discrete form and ΔE_i is the bin width for the integration. In order to use this method, it is necessary to estimate $\mathcal{S}$, $\mathcal{ARF}(E_i)$, and $\mathcal{R}(E_i, PI_j)$ in the STEM-TES-EDS system.

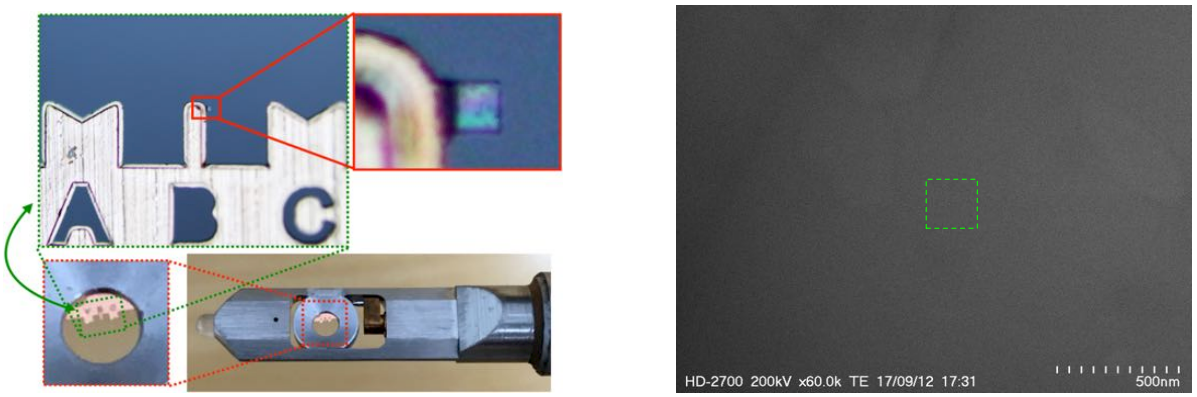

Fig. 8.1 Sample setup for construction of the response function (left), STEM Image of olivine sample (right)

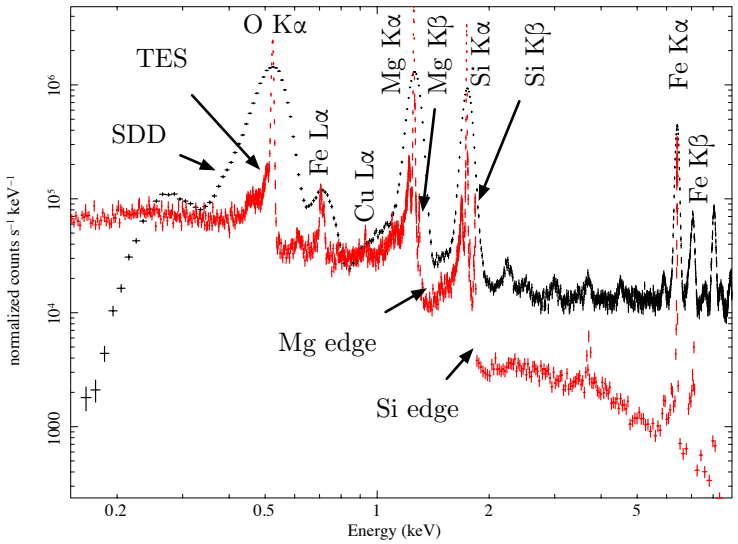

Fig. 8.2 Comparison of spectra obtained by TES (red) and SDD (black)

8.1.1 Observation of sample and acquisition of the data

We conducted experiments using Olivine's thin film samples (not standard sample) in order to construct the response function with setup as shown in Figure 8.1 (left) and to show the advantages of TES for element analysis of minerals. The STEM electron beam was directed to a green area (spot area) of Figure 8.1 (right) with the aperture size of AP2 of STEM, and an X-ray signal was obtained. In acquisition of X-rays, the data was obtained in the through mode, and pulses were extracted as in Subsection 7.3.2. The pulse that was considered to be the oxygen emission line was taken out from the pulse height histogram, and the template for the optimum filter was prepared from that pulse records. We applied the optimal filter using the template to the pulses, and obtained the PHA spectrum. In order to convert PHA to energy, we compared the spectrum obtained by TES with the spectrum obtained by SDD, and identified the lines. Then we constructed PHA to energy calibration curve with 5th order polynomial. Figure 8.2 shows the energy spectra of TES and SDD. TES spectra can detect the CuLα line, Si edge and Mg edge, and can separate SiKβ, MgKβ line, but those lines and edges cannot be detected and separated with SDD spectra.

8.1.2 Construction of Response function for Detector

$$\mathcal{R}\left(E_i, PI_j\right) = \begin{pmatrix} R_{11} & R_{12} & \cdots & \cdots & R_{1n} \\ R_{21} & R_{22} & \cdots & \cdots & R_{n2} \\ \vdots & \vdots & \ddots & R_{ij} & \vdots \\ \vdots & \vdots & & \ddots & \vdots \\ R_{m1} & R_{m2} & \cdots & \cdots & R_{mn} \end{pmatrix} \tag{8.2}$$

We considered $\mathcal{R}(E_i, PI_j)$ of the TES calorimeter. *Redistribution Matrix File* (RMF) is the response function

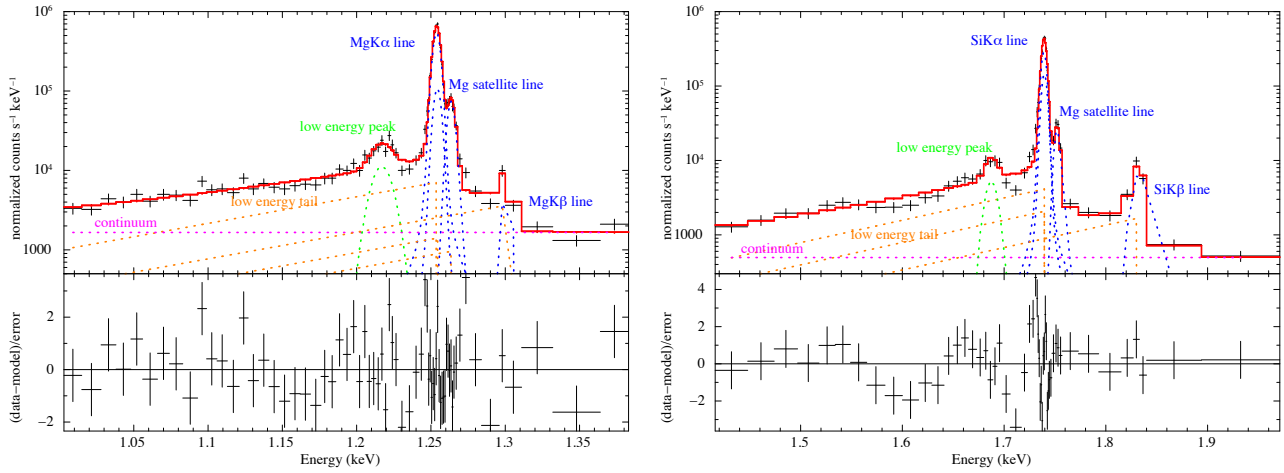

Fig. 8.3 Fit result of line emission of Mg (left) and Si (right)

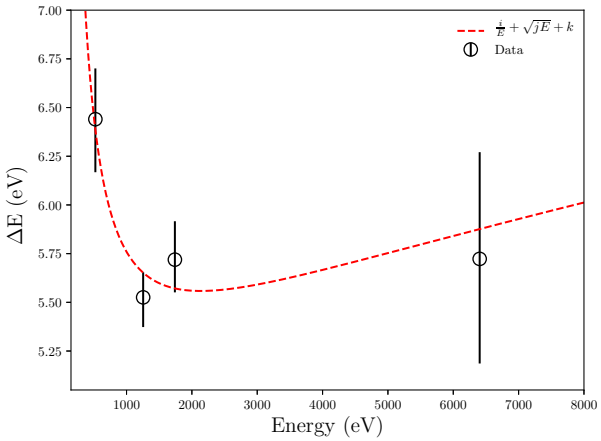

Fig. 8.4 Energy resolution vs. Energy

(matrix) when X-ray is incident on the TES calorimeter. The response function is not a simple Gaussian function, but it contains a low energy tail and a low energy peak as shown in Figure 8.3. The former is due to the loss of electrons from the X-ray absorber before the X-ray energy injected to it has not been thermalized. The latter is likely due to events for which X-ray photon was absorbed outside the X-ray absorber, e.g. TES and SiN_x/SiO_2 membrane. Figure 8.3 shows the spectra in the energy band of MgKα (left) and SiKα (right) when observing Olivine. The three blue curves are MgKα or SiKα line. The purple curve is a model of continuum X-rays. The orange line is low energy tail which seems to be due to electron loss. The green line is low energy peak.

Energy resolution

We investigated the energy resolution for oxygen, magnesium, silicon, and iron. Since the resolution is high in the energy spectrum of TES, we fitted each emission line by using the model containing the fine structure of each element. The values used for the model are shown in Table 8.1. In the fit, we included a low energy tail and low energy peak described below in the model as shown in Figure 8.3. From fit results, we investigated the relation between the energy resolution and energy and show the relation in Figure 8.4. There is no model that adequately

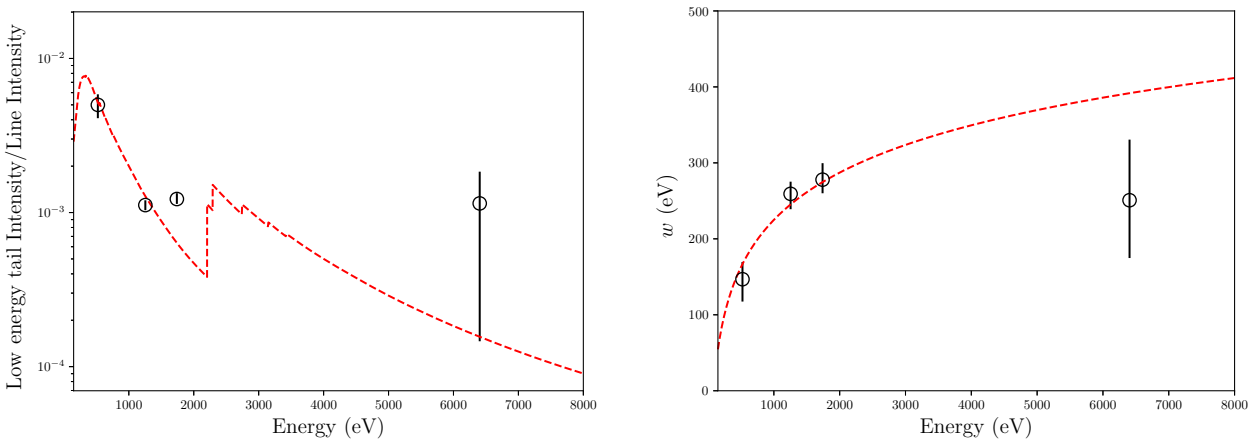

Fig. 8.5 u vs. energy (left), w vs. energy (right)

describes this relationship, so that we introduce the following (Equation (8.3)) model that fits this relationship,

$$F_{\Delta \mathrm{E}}(E) = \frac{i}{E} + \sqrt{jE} + k, \tag{8.3}$$

where i, j, and k are free parameters. The first term is an empirical equation for matching low energy side which is irregular. The second term is introduced from the relationship $\left(\Delta E \sim \sqrt{E_{\mathrm{sat}}}\right)$ between the saturation energy ($E_{\mathrm{sat}} \sim CT/\alpha$) and the energy resolution ($\Delta E \sim \sqrt{k_{\mathrm{B}} T^2 C/\alpha}$). The last term means a certain energy resolution, and originally TES energy resolution is constant until the saturation energy E_{sat}. The fitting results using this Equation (8.3) are shown in Figure 8.4 (red dash line).

Low energy tail

Electrons may jump out from the inside of the absorber by X-rays incident on the TES and are converted into electrons. This is called 'electron loss', and in the composition on the spectrum it is observed as a tail on the low energy side (orange line in Figure 8.3). The intensity and quantity of low energy tail depend on the X-ray energy. The low energy tail can be represented with the model expressed by

$$F_{\mathrm{tail}}(E) = u(E) \sum_{i=1}^{n} r_i \exp\left(-\frac{E_i - E}{w(E)}\right) \theta(E_i - E), \tag{8.4}$$

$$u(E) = A \times \mu(E), \tag{8.5}$$

$$w(E) = a \log(bE) + c. \tag{8.6}$$

The model fit is performed for each energy, and the energy dependence of $u(E)$ and $w(E)$ is investigated (Figure 8.5). With low energy x-rays, the probability that electron loss occurs is high because X-rays are absorbed near the surface of the absorber. It is considered that the energy dependence of the intensity $u(E)$ can be expressed by the depth absorbed in the absorber, that is, the linear absorption coefficient of the absorber material (Equation (8.5)). Also, Figure 8.5 (right) shows the total $w(E)$ vs. energy of each main peak, and the total $w(E)$ has the dimension of energy, which can be thought as the loss rate of energy. For this we assumed Equation (8.6).

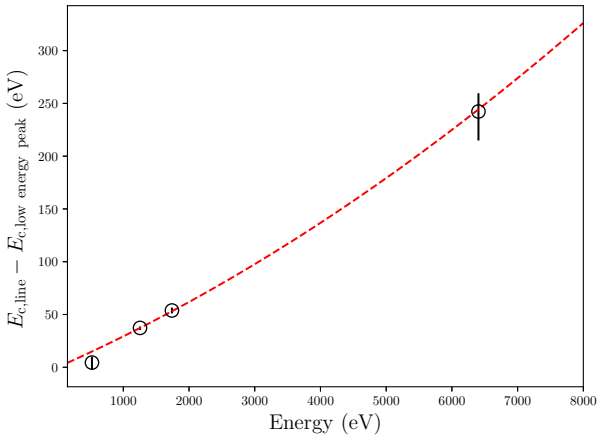

Fig. 8.6 Difference of the center energy of Main peak and low energy peak

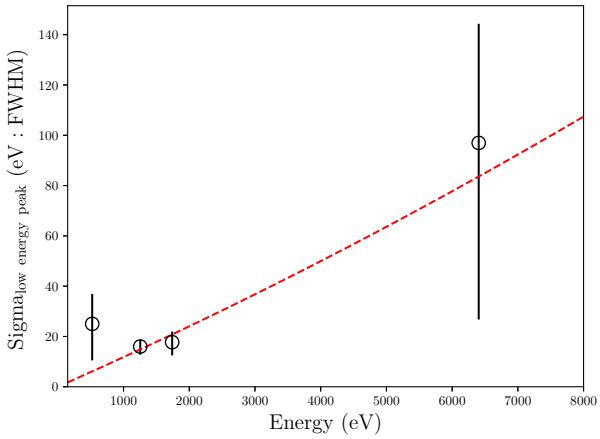

Fig. 8.7 Width of low energy peak (FWHM)

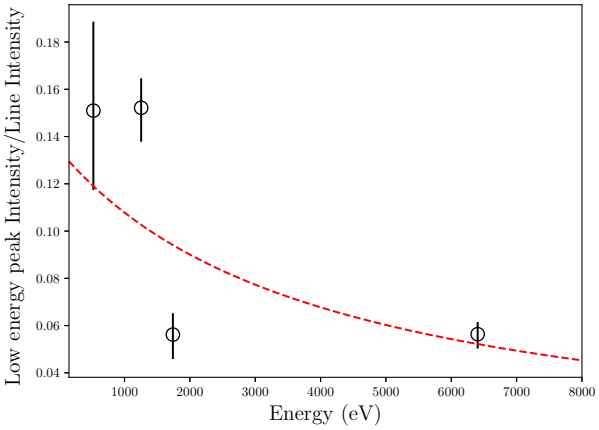

Fig. 8.8 Intensity ratio of low energy peak and Main peak

Low energy peak

As shown in Figure 8.3, the low energy peak shows a peak appearing on the low energy side. It is likely to be caused by absorption of X-ray photons outside the absorber, e.g. TES or membrane. When an X-ray photon is absorbed by the TES, we expect to have a pulse whose rise time is faster and peak is lower, because the TES will detect the temperature rise quickly and thermal energy escapes to the thermal bath quickly. This structure must be included in the response function. Low energy peak was fitted using the Gaussian function as the following equation:

$$F_{\mathrm{lpeak}}(E) = \frac{K(E_{\mathrm{lc}})}{\sigma(E_{\mathrm{lc}})\sqrt{2\pi}} \exp\left[-\frac{(E - E_{\mathrm{lc}}(E_{\mathrm{c}}))^2}{2\sigma(E_{\mathrm{lc}})^2}\right], \tag{8.7}$$

$$E_{\mathrm{lc}}(E) = mE^2 + nE, \tag{8.8}$$

$$\sigma(E) = pE^2 + qE, \tag{8.9}$$

$$K(E_{\mathrm{lc}}) = \frac{r}{E + s}, \tag{8.10}$$

Table 8.1 Fit parameter and results for construction of response function

Model	parameter	O Kα	Mg Kα	Si Kα	Fe Kα
gsmooth	FWHM (eV)	$6.44^{+0.27}_{-0.26}$	$5.53^{+0.15}_{-0.13}$	$5.72^{+0.17}_{-0.20}$	$5.72^{+0.53}_{-0.55}$
lorentz	E_c (eV)	$523.76^{+0.14}_{-0.47}$	$1254.16^{+0.02}_{-0.09}$	$1739.65^{+0.06}_{-0.09}$	$6405.30^{+0.24}_{-0.24}$
(main peak $K_{\alpha 1,1}$)	norm	$0.261^{+0.012}_{-0.013}$	$0.252^{+0.004}_{-0.004}$	$0.355^{+0.009}_{-0.005}$	$0.112^{+0.006}_{-0.006}$
exponential tail	w	$7.34^{+1.47}_{-1.13} \times 10^{-2}$	$12.96^{+1.00}_{-0.80} \times 10^{-2}$	$13.89^{+0.89}_{-1.09} \times 10^{-2}$	$3.58^{+1.14}_{-1.09} \times 10^{-2}$
	u	$2.17^{+0.39}_{-0.37} \times 10^{-3}$	$5.22^{+0.38}_{-0.39} \times 10^{-4}$	$7.34^{+0.50}_{-0.66} \times 10^{-4}$	$2.21^{+1.92}_{-1.34} \times 10^{-4}$
gaussian	Line E (eV)	$519.3^{+6.5}_{-5.5}$	$1216.9^{+1.9}_{-1.3}$	$1685.9^{+2.7}_{-2.7}$	$6162.9^{+1.9}_{-1.3}$
	FWHM (eV)	$25.0^{+14.5}_{-11.9}$	$16.0^{+3.2}_{-2.7}$	$17.7^{+5.2}_{-4.2}$	$97.0^{+70.2}_{-47.4}$
	norm	$6.56^{+3.36}_{-3.76} \times 10^{-2}$	$7.10^{+1.44}_{-1.25} \times 10^{-2}$	$3.37^{+1.04}_{-0.90} \times 10^{-2}$	$1.09^{+0.61}_{-0.51} \times 10^{-2}$

where $K(E_{\rm lc})$ is the intensity of the low energy peak, $\sigma(E)$ is the width of Gaussian, $E_{\rm lc}(E)$ is the centroid energy of the low energy peak, and E_c is the energy of the main peak. We fitted each line including Equation (8.7) in the model function. The energy dependencies of parameters in Equation (8.7) are shown in Figure 8.6, Figure 8.7 and Figure 8.8. We fitted the dependencies empirically with polynomial functions and found Equation (8.8), Equation (8.9) and Equation (8.10) represent them well.

Response function

We constructed a response function from the contents discussed in the energy resolution, the low energy tail and the low energy peak. The response function when a delta function-like line enters is described as follows:

$$\mathcal{R}(E_i, PI_j) = \frac{1}{F_{\Delta E}(PI_j)\sqrt{2\pi}} \exp\left[-\frac{(E_i - PI_j)^2}{2F_{\Delta E}(PI_j)^2}\right] + F_{\rm tail}(PI_j) + F_{\rm lpeak}(PI_j). \tag{8.11}$$

8.1.3 Construction of efficiency function

In this subsection, we consider the function $\mathcal{ARF}(E)$ in Equation (8.1). This function represents the energy dependence of detection efficiency and consists of three parts; throughput of the capillary optics, transmissions of window/filters, and the detection efficiency of the detector. This function is called an *ancillary response file* (ARF) in XSPEC software terminology. For a given thickness of the X-ray window/filter and the thickness of the TES absorber, the transmission (Equation (8.12)) and the absorption probability (Equation (8.13)) are readily given:

$$Tr_m = \exp(-\mu_m y_{th}), \tag{8.12}$$

$$Eff_m = 1 - \exp(-\mu_m y_{th}), \tag{8.13}$$

where μ_m is the linear absorption coefficient $\left(\mathrm{cm}^{-1}\right)$ of the material and y_{th} is the thickness of the material. The line absorption coefficient has energy dependency, and its energy table refers to the database of LBL[*1]. In STEM, the X-ray windows are installed in each shield, each being a thin film of aluminum/polyimide, and the thickness of each X-ray window is summarized in Table 7.1. The transmission efficiency of each window in the $0.05-20$ keV energy band is shown in Figure 8.9. The structure of the TES calorimeter consists of Au absorber (thickness: 4.2 μm) and Ti / Au (thickness: 40/108 nm) of the TES as described in Chapter 5. Using Equation (8.13), the $0.05-20$ keV quantum efficiency of energy band is shown in Figure 8.10. As shown in the previous chapter, we use a capillary X-ray optics to increase the solid angle to collect X-rays from the sample. Figure 8.12 shows the

[*1] Lawrence Berkley national Laboratory : http://henke.lbl.gov/optical_constants/filter2.html

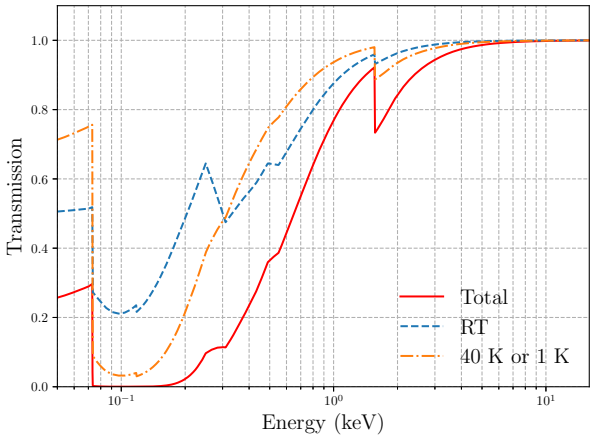

Fig. 8.9 Transmission of X-ray windows

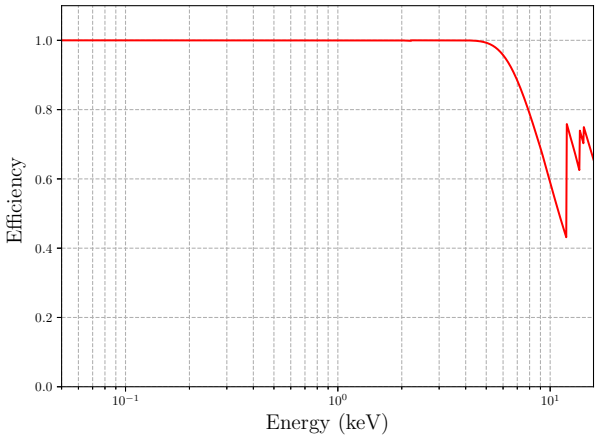

Fig. 8.10 Quantum Efficiency of TES

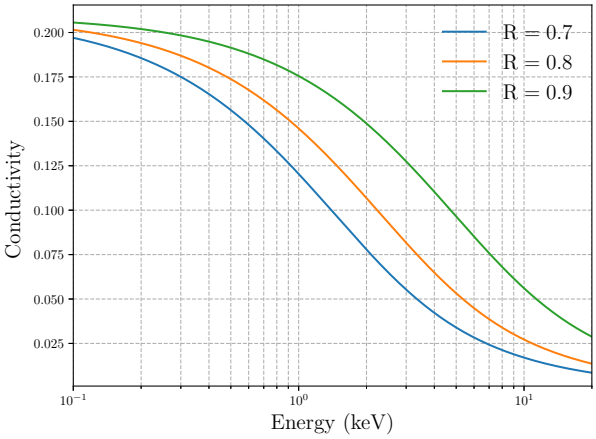

Fig. 8.11 Conductivity S of polycapillary

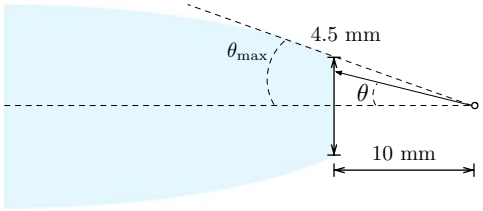

Fig. 8.12 Enlarged view of polycapillary

detail geometry near the inlet side of the polycapillary. Because the detector is placed about 30 cm from the sample and the detector size is about 3 mm, the solid angle increases by 3 orders of magnitude. However, we need to consider the transmission of the optics, which is often called "conductivity." The polycapillary conductivity S can be approximated by the following equations:

$$\theta_{\mathrm{c}} = \frac{0.02\sqrt{\rho}}{E}, \tag{8.14}$$

$$T(\theta) = R^{(\theta/\theta_{\mathrm{c}})}, \tag{8.15}$$

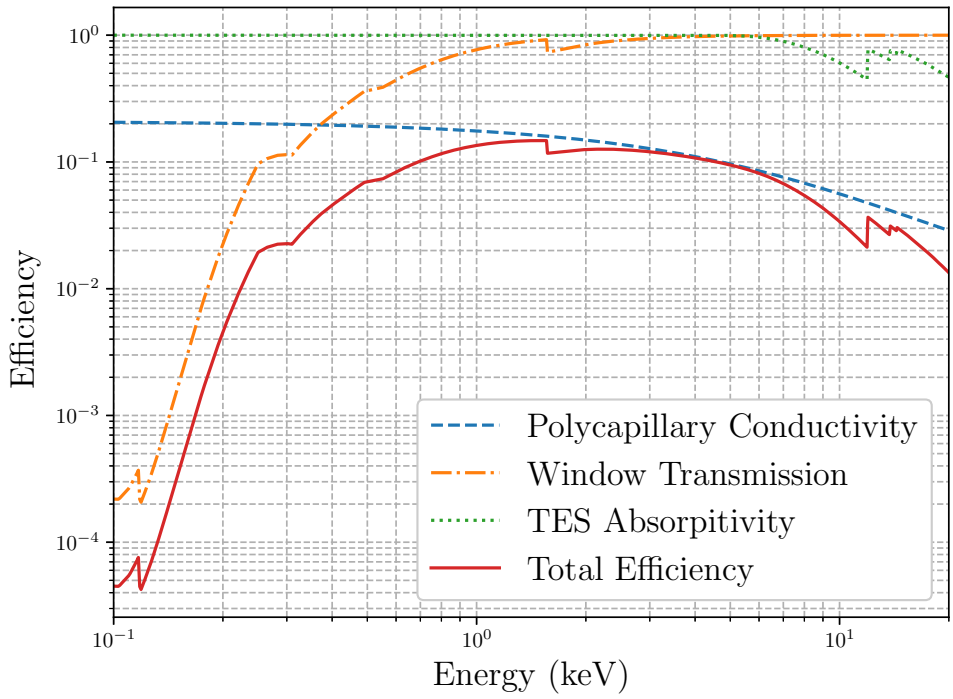

Fig. 8.13 Total efficiency of STEM-TES-EDS system

$$S = \int_0^{\theta_{\max}} T(\theta)\, d\theta, = \frac{2\theta_c}{\log R}\left(R^{\theta_{\max}/2\theta_c} - 1\right), \tag{8.16}$$

where, θ_c is the critical reflection angle (rad.) below which X-rays undergo total reflection. The critical angle is determined by the electron density, thus approximately, the mass density of material, ρ (g/cm^3), and the X-ray energy E (keV). It is approximately represented by Equation (8.14) [10]. The transmission of a photon that enters with an incident angle θ can be roughly approximated by Equation (8.15). Integrating it over incident angles, the conductivity can be estimated with Equation (8.16). The conductivity of polycapillary is shown for $R = 0.7$, 0.8, and 0.9 in Figure 8.11. S is between 0.03 to 0.2 for $E = 1$ to 10 keV. Therefore, the effective solid angle is larger by a factor of 30 to 200 than that without the capillary optics. The efficiency, i.e. ARF is given by multiplying the capillary conductance, window/filter transmissions, and the detector efficiency.

$$\mathcal{ARF}(E) = S(E, \theta_{\max}, \rho, R) \times Eff(E, y_{\text{abs}}) \times Tr(E, y_{\text{Al}}, y_{\text{Poly}}), \tag{8.17}$$

which is shown as a function of energy in Figure 8.13, where we adopted $R = 0.9$. We will determine the value of R from model fitting in section 8.2.

8.1.4 Combination of the Response function and optics model

We performed the spectral fit in the total energy band $(0.15 - 7.0$ keV) from Equation (8.1) using RMF and ARF. A bremsstrahlung due to electrons at a single atom can be empirically approximated by a power function. However, there are many elements in actual samples and it is difficult to express them with a single power function. Therefore we tried several different model functions for the continuum X-ray and found that a double-broken

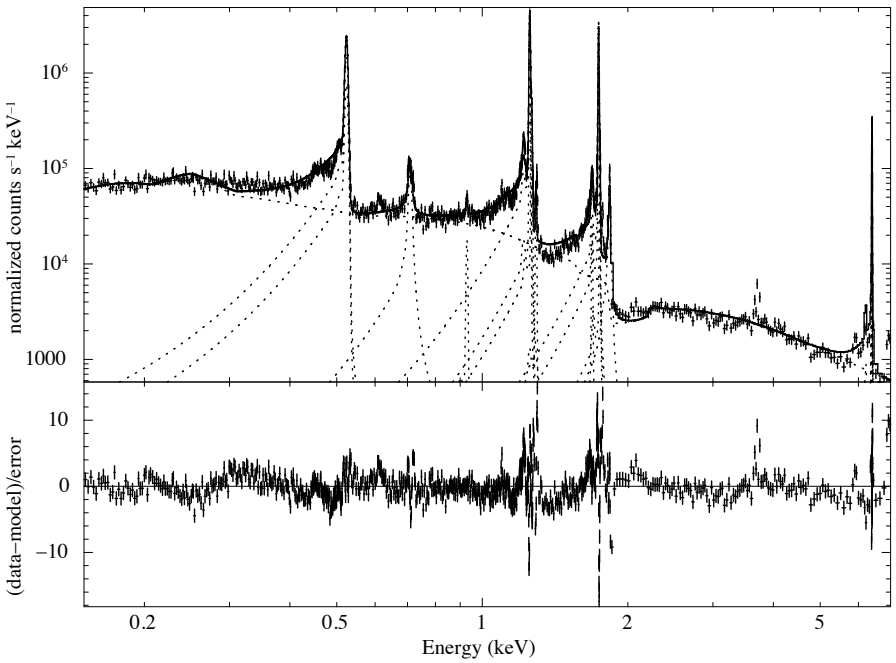

Fig. 8.14 Obtained spectrum, and fit result using ARF model and RMF

power-law function (bkn2pow) defined in Equation (8.18) represent it well.

$$A\left(E;K,\Gamma_1,E_{break1},\Gamma_2,E_{break2},\Gamma_3\right)=\begin{cases}KE^{-\Gamma_1} & \text{if } E\le E_{break,1},\\ KE_{break,1}^{\Gamma_2-\Gamma_1}E^{-\Gamma_2} & \text{if } E_{break,1}\le E\le E_{break,2},\\ KE_{break,1}^{\Gamma_2-\Gamma_1}E_{break,2}^{\Gamma_3-\Gamma_2}E^{-\Gamma_3} & \text{if } E_{break,2}\le E,\end{cases} \tag{8.18}$$

where Γ_1 is power law index for $E\le E_{break,1}$, $E_{break,1}$ is the first break point for the energy in keV, Γ_2 is power law photon index for $E_{break,1}\le E\le E_{break,2}$, $E_{break,2}$ is the second break point for the energy in keV, Γ_3 is power law photon index for $E_{break,2}\le E$, and K is $\left(\text{photons/keV/cm}^2\text{/s}\right)$. The emission lines are fitted with the number of the fine structures expressed with Lorentzian function as follows:

$$L\left(E;K,\Gamma,E_{\mathrm{L}}\right)=K\frac{\Gamma}{2\pi}\frac{1}{\left(E-E_{\mathrm{L}}\right)^2+\left(\Gamma/2\right)^2}, \tag{8.19}$$

where E_{L} is the line energy in keV, Γ is FWHM line width as the natural width in keV, and K is $\left(\text{photons/cm}^2\text{/s}\right)$. In addition, we found that we need to incorporate a model of silicon and magnesium absorption edges to represent the obtained X-ray spectrum well. We consider that they are self-absorption of the sample. Figure 8.14 shows the result of fitting, the absorption structure present in the continuous component and the tail of the line are reproduced.

8.2 Experiments towards Quantitative Analysis

8.2.1 Test for calibration

Towards quantitative analysis, we took a set of calibration data using a standard sample. This standard sample is Olivine and contains oxygen, magnesium, silicon and iron, with mass concentrations of 43.18%, 31.1%, 17.97%, and 7.75%, respectively. As shown in Figure 8.15, the sample is placed on the organic film on the copper grid. The

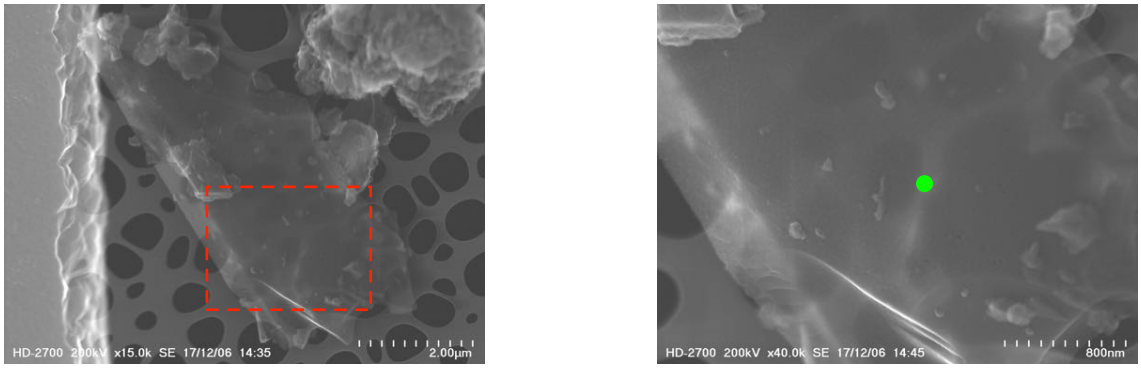

Fig. 8.15 STEM image of Olivine standard sample, $15{\times}10^3$ (left), $40{\times}10^3$ (right)

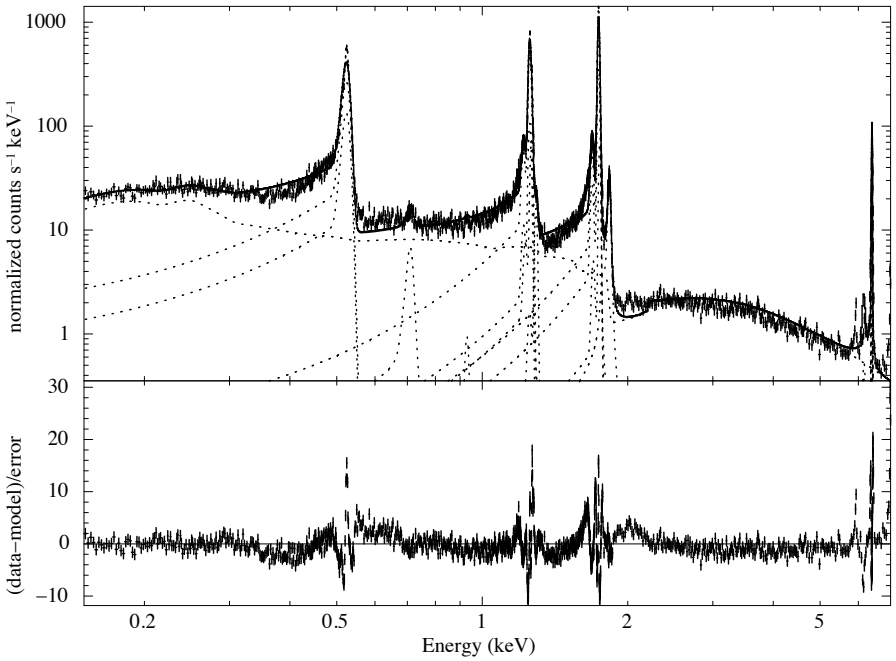

Fig. 8.16 Spectrum of Olivine standard sample

sample was irradiated with electron beams on a spot as shown in Figure 8.15 (a green point of right). The X-ray pulse data were obtained in through mode and pulse records were extracted as described in Subsection 7.3.2. The pulse records were processed with an optimal filter to obtain PHA values, and then PHA values were converted to Pulse Invariant (PI) using the gain calibration function represented with a fifth order polynomial function. We created a spectrum combined 16 channel PI (The removed channel is out of FLL during the measurement). We applied a model fit to the obtained energy spectrum with a model function convolved with ARF and response matrix Equation (8.1). We used the following model:

$$\mathcal{M}(E) = Abs\left(y_{\mathrm{Mg}}, y_{\mathrm{Si}}\right) \times \left[\sum_{j=1}^{m}\left(\sum_{k=1}^{n} L_k\left(K, \Gamma, E_{\mathrm{L}}\right)\right)_j + A\left(K, \Gamma_1, E_{b1}, \Gamma_2, E_{b2}, \Gamma_3\right)\right],$$

where j and m are the numbers of elements, k and n are the numbers of fine structure. The conductance of the capillary optics in the ARF contains an unknown factor, which is R in Equation (8.15). Other parameters of the capillary optics are known as follows: $\theta_{\max} = 0.209$, and $\rho = 2.3$ g/cm. In the next spectral model fit, we treated

Table 8.2 Spectral fit parameters of olivine standard sample

Item	Model	parameter	fit values	Unit
polycapillary	Conductance S	$\theta_{\rm max}$	0.209 (fix)	rad.
		ρ	2.30 (fix)	g/cm
		R	0.995 (fix)	
Detector Efficiency	TES	$y_{\rm abs}$	4.00×10^{-6} (fix)	m
Window Transmission	Polyimid	$y_{\rm Poly}$	530×10^{-9} (fix)	↑
	Al	$y_{\rm Al}$	230×10^{-9} (fix)	↑
Sample absorption	Mg	$y_{\rm Mg}$	$3.97^{+1.02}_{-1.04} \times 10^{-7}$	↑
	Si	$y_{\rm Si}$	$2.48^{+0.10}_{-0.10} \times 10^{-6}$	↑
Emission line	O K$\alpha_{1,1}$	norm	661^{+82}_{-72}	photons/cm^2/s
	Fe L$\alpha_{1,1}$	↑	$13.6^{+2.3}_{-2.1}$	↑
	Cu L$\alpha_{1,1}$	↑	0.519 (fix)	↑
	Mg K$\alpha_{1,1}$	↑	$28.0^{+0.6}_{-0.6}$	↑
	Mg Kβ	↑	$4.10^{+0.34}_{-0.34}$	↑
	Si K$\alpha_{1,1}$	↑	107^{+5}_{-5}	↑
	Si Kβ	↑	$32..4^{+2.2}_{-2.0}$	↑
	Fe K$\alpha_{1,1}$	↑	$17.7^{+0.3}_{-0.3}$	↑
Continuum	bkn2pow	Γ_1	$8.03^{+0.67}_{-0.53}$	-
	$A\,(E; K, \Gamma_1, E_{b1}, \Gamma_2, E_{b2}, \Gamma_3)$	E_{b1}	$0.218^{+0.007}_{-0.008}$	keV
		Γ_2	$3.65^{+0.10}_{-0.10}$	-
		E_{b2}	$1.06^{+0.02}_{-0.02}$	keV
		Γ_3	$1.26^{+0.02}_{-0.02}$	-
		K	$0.136^{+0.038}_{-0.039}$	photons/keV/cm^2/s

R as a free parameter and estimated the best-fit value. The parameter values of best-fit model are shown in Table 8.2. From the best-fit values of line intensities, the K-factors were calculated using Equation (2.5) - (2.7). The results are,

$$K_{\rm O-Si} = 4.17^{+0.55}_{-0.49} \times 10^{-1},$$
$$K_{\rm Mg-Si} = 3.15^{+0.15}_{-0.15},$$
$$K_{\rm Fe-Si} = 2.33^{+0.11}_{-0.11},$$

where $K_{\rm O-Si}$, $K_{\rm Mg-Si}$, and $K_{\rm Fe-Si}$ are the K-factors of oxygen, magnesium, and iron for silicon respectively. We fitted the model with K (a normalization factor), $y_{\rm Mg}$, $y_{\rm Si}$, $\Gamma_1, E_{b1}, \Gamma_2, E_{b2}$, and Γ_3 as the free parameters by using the maximum likelihood method assuming the Poisson statistics. The statistical errors of the fit parameters were estimated using so-called C-statistics. We define $C = -2\ln\mathcal{L}$, where $\mathcal{L}$ is the likelihood function. $\Delta C = C_{\rm true} - C_{\rm min}$ follows χ^2 distribution with the degrees of freedom. The errors of these results are estimated by the single parameter errors at a 90% confidence level, which corresponds to $\Delta C = 2.701$.

8.2.2 Demonstration of the quantitative analysis

To demonstrate the quantitative analysis using the K-factors derived in the previous subsection, we analyzed a material whose chemical composition is simple and well defined. For this purpose we selected a silicon-oxide SiO_2

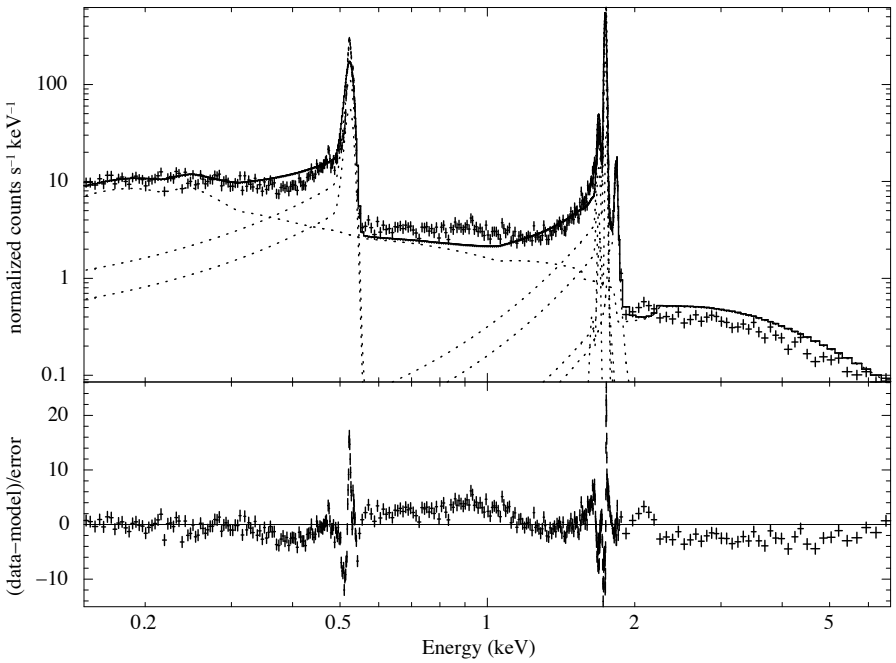

Fig. 8.17 Fit result of SiO_2 spectrum

Table 8.3 Spectral fit parameters of SiO_2 film

Item	Model	parameter	fit values	Unit
polycapillary	Conductance S	$\theta_{\max}$	0.209 (fix)	rad.
		ρ	2.30 (fix)	g/cm
		R	0.995 (fix)	
Detector Efficiency	TES	$y_{\rm abs}$	4×10^{-6} (fix)	m
Window Transmission	Polyimid	$y_{\rm Poly}$	530 (fix)	↑
	Al	$y_{\rm Al}$	230 (fix)	↑
Sample absorption	Si	$y_{\rm Si}$	$2.02^{+0.04}_{-0.04} \times 10^{-6}$	↑
Emission line	O K$\alpha_{1,1}$	norm	$153.4^{+6.9}_{-6.5}$	photons/cm^2/s
	Si K$\alpha_{1,1}$	↑	$45.8^{+0.4}_{-0.4}$	↑
	Si Kβ	↑	$11.8^{+0.5}_{-0.5}$	↑
Continuous	bkn2pow	Γ_1	8.54 (fix)	-
	$A\,(E; K, \Gamma_1, E_{b1}, \Gamma_2, E_{b2}, \Gamma_3)$	E_{b1}	0.218 (fix)	keV
		Γ_2	3.65 (fix)	-
		E_{b2}	1.05 (fix)	keV
		Γ_3	1.26 (fix)	-
		K	$2.63^{+0.07}_{-0.07} \times 10^{-2}$	photons/keV/cm^2/s

film, and the atomic weight percent (at.%) of silicon and oxygen is 1 : 2. The setting of STEM was the same as the calibration and we obtained the data using the same channel. In pulse processing, the template for optimum filter processing and the energy calibration curve were used in the same way as the calibration, and we created X-ray energy spectra as shown in Figure 8.17. We used the model function consisting of O Kα, Si Kα and Si Kβ emission lines and continuum. We used the same model functions for the lines and continuum as those used in the previous subsection. In Figure 8.17 and Table 8.3, we show the results of fits. Using the intensities of lines and the O-to-Si K-factor, we estimate the percent concentration of mass (see Equation (2.5) - Equation (2.7)).

The results are

$$C_{\mathrm{O}} = \frac{A}{1+A} = 56.58^{+3.19}_{-3.30}\ (\mathrm{wt.\%})\,,$$
$$C_{\mathrm{Si}} = \frac{1}{1+A} = 43.41^{+3.30}_{-3.19}\ (\mathrm{wt.\%})\,,$$
$$A = K_{\mathrm{o-Si}}\frac{I_{\mathrm{O}}}{I_{\mathrm{Si}}}.$$

Converting to the number-density ration, we obtain

$$Z_{\mathrm{O}} = 69.59^{+4.98}_{-4.56}\ (\mathrm{at.\%})\,,$$
$$Z_{\mathrm{Si}} = 30.41^{+2.71}_{-2.89}\ (\mathrm{at.\%})\,.$$

And the ratio of the number-density of oxygen to silicon is then,

$$\frac{Z_{\mathrm{O}}}{Z_{\mathrm{Si}}} = 2.29^{+0.32}_{-0.29}.$$

This result is consistent with SiO_2 within the statistical errors.

Chapter 9

Discussion

9.1 STEM-TES-EDS System

We have developed an energy dispersive X-ray spectrometer (EDS) for an STEM using a TES microcalorimeter array. In order to fulfill the requirements of the system with a high energy resolution of 10 eV (FWHM), high counting rate capability of 5 kcps, and a wide energy range of (0.5-15 keV), we developed an 8×8 format 64 pixel TES microcalorimeter array. The high energy resolution and high counting rate capability are contradictory requirement. We carefully designed the superconducting temperature of the TES and size of detectors. The device showed an energy resolution of 4.8 eV in the laboratory and low-counting rate environment. We then developed a detector head which can be installed in the cryostat for the STEM-TES system. On the detector head, not only the TES microcalorimeter array but also the cryogenic-temperature front-end electronics SQUID array amplifiers (SAAs), TES bias shunt resister, and dumping inductors are mounted. Unfortunately, there remains a problem in the superconducting flip-chip bonding technologies used to mount the SAA chip, and we used only 19 pixels. Under such limitations, the 10 eV resolution under 5 kcps environment was almost fulfilled (9.5 eV at 4.5 kcps, and 11 eV at 5.0 kcps for AlKα line). In order to achieve this high counting rate with 19 pixels, we had to reduce the data length of X-ray pulses which are used to determine the pulse height with the optimum filtering. In order to obtain a high throughput of the detector, it was necessary to reduce the data length to 150 μs in high counting rate environment. The nominal value in low-counting rate environment is 1 ms. This is a part of reasons why the energy resolution degrades at high counting rate. By improving the yield of the superconducting flip-chip bonding technology, we can increase the number of pixels by a factor of more than three. We thus expect that we can obtain 10 eV energy resolution even with 15 kcps counting rate.

9.2 Quantitative analysis towards microanalysis of astromaterials

We then studied the calibration and analysis methods. We analyzed an Olivine standard sample whose element concentrations are known with the STEM-TES-EDS system and estimated the values of so-called K factors, which can be used to estimate element concentrations of other samples. We then applied the value to the measurements of SiO_2 to prove that the Si to O ratio could be correctly estimated. Because this result is obtained based on experiment, we consider that the result is highly reliable. However, the present experiment of Section 8.2 is limited by Poisson statistics, and we consider that we can improve by making all 64 pixels available, and/or taking a longer integration time. Thus we would like to investigate what happens when we obtain a higher counting statistics. We also would like to compare the capability of our TES EDS with that of conventional semiconductor-based detectors. For these purposes, in this section, we assume the best-fit model of the Olivine spectrum obtained with the TES EDS as an input spectrum and perform Monte-Carlo simulations.

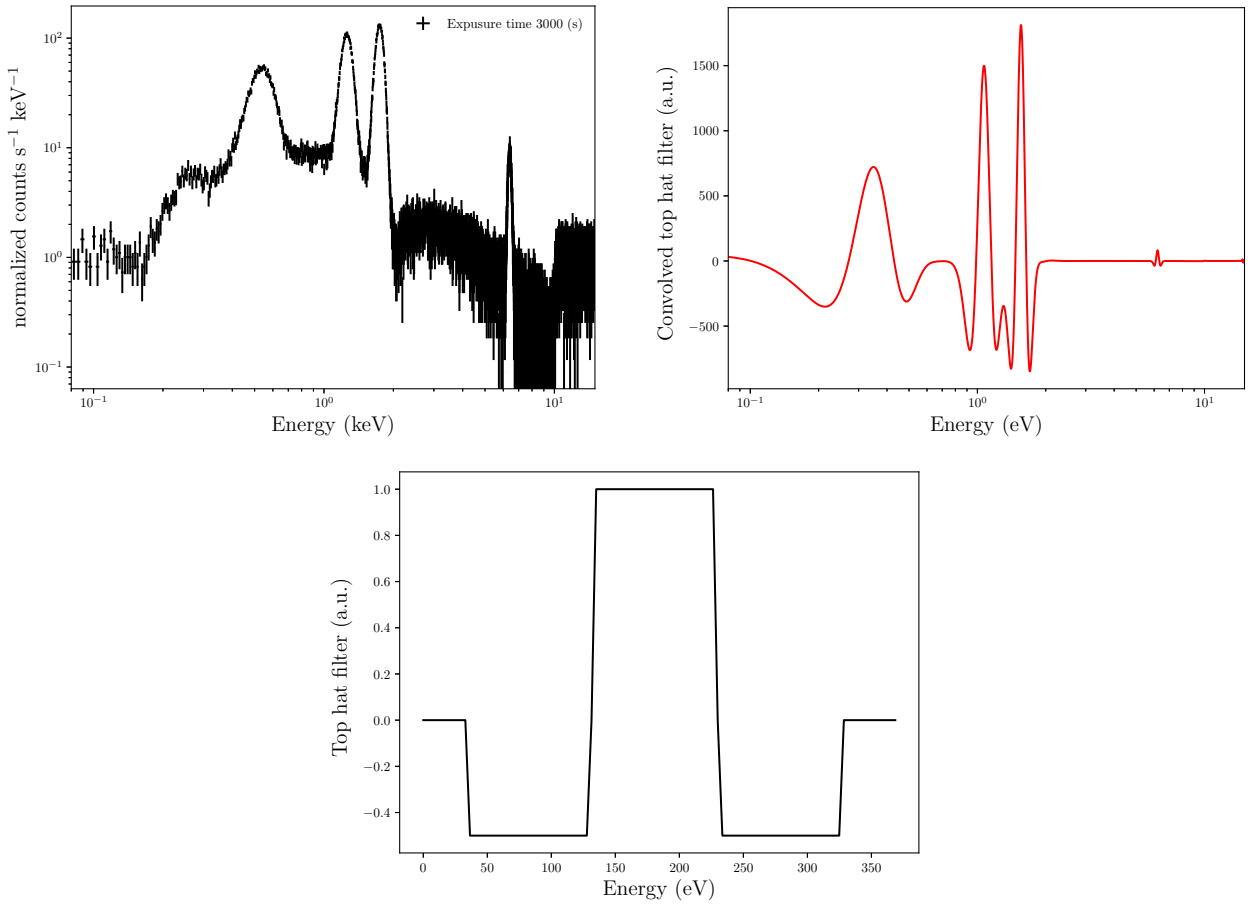

Fig. 9.1 Simulated X-ray spectra in SDD (upper left), Spectrum convolved with top hat filter (upper right), Top hat filter (bottom)

9.2.1 Estimated systematic error for top hat filter method

We first investigated the systematic errors involved in the data analysis of a semiconductor-based detector. In material analysis, a Si Drift Detector (SDD) is widely used. We create simulation spectrum for an X-ray CCD (Charge-Coupled Device) camera named the XIS on board the Suzaku X-ray astronomy satellite, simply because its energy resolution is similar to that of SDD and because we have the response function of the instrument in hand. As mentioned above, we assume the best-fit model parameters of Olivine for the sample self-absorption, emission lines, and continuum shown in Table 8.2.

Figure 9.1 upper left shows the result of simulation, and the top hat filter (Figure 9.1 bottom) was then applied to the spectrum. As shown in Figure 9.1 (upper right), we find that the continuum emission was well removed from the spectrum, and statistical fluctuations have been smoothed out. Thus this method is good when we find emission lines by eyes. Then in order to estimate the counting rates of lines from the top-hat-filter convolved spectrum, we made reference spectra simulating a line with a fine structure for each emission line with XIS response (Figure 9.2). The exposure time of the simulation was set long enough (10^{10} s), in order to reduce the statistical errors small enough. Then the obtained simulation spectra were convoluted with the same top hat filter (Figure 9.2). Then the Olivine simulation spectrum convolved with the top hat filter was fitted with a

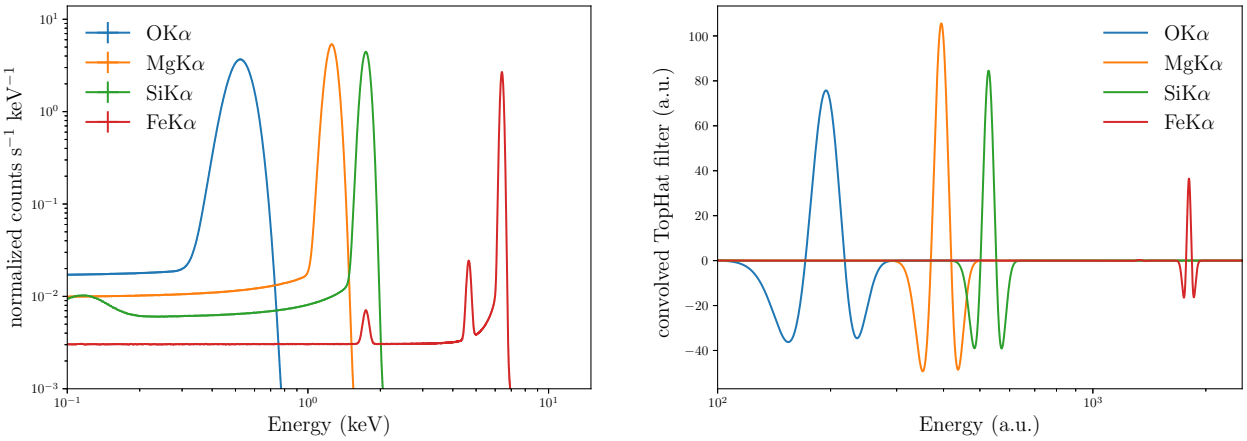

Fig. 9.2 Simulated standard spectrum (left), Standard spectrum convolved with top hat filter (right)

Table 9.1 Results of the SDD simulation using the top hat filter method

*	j_* (a.u.)	$j_*/j_{\mathrm{SiK}\alpha}$ of simulation	$I_*/I_{\mathrm{SiK}\alpha}$ of model	systematic error (|Simulation − Model| /Model × 100)
OKα	12.03	0.409	0.463	11.7%
MgKα	18.77	0.646	0.605	6.78%
SiKα	29.07	1	1	-
FeKα	3.207	0.109	0.0589	85.1%

model function consisting of a sum of the reference spectra by minimizing the value of S defined as

$$S = \sum_{i=0}^{n} \left[D_{\mathrm{s}}\left(\mathrm{PI}_i\right) - \left(j_{\mathrm{OK}\alpha} M_{\mathrm{OK}\alpha}\left(\mathrm{PI}_i\right) + j_{\mathrm{MgK}\alpha} M_{\mathrm{MgK}\alpha}\left(\mathrm{PI}_i\right) + j_{\mathrm{SiK}\alpha} M_{\mathrm{SiK}\alpha}\left(\mathrm{PI}_i\right) + j_{\mathrm{FeK}\alpha} M_{\mathrm{FeK}\alpha}\left(\mathrm{PI}_i\right) \right) \right]^2, \quad (9.1)$$

where D_{s} is the Olivine simulation spectrum convolved with the top hat filter, $\{M_*\}$ the reference spectra of {*} emission line convolved with the top-hat filter, and $\{j_*\}$ fit parameters. We calculated the intensity ratio to Si ($= j_{\mathrm{SiK}\alpha}$) using the obtained $\{j_*\}$ (Table 9.1). We considered the statistical error of the intensity calculated by top hat filter. To estimate this statistical error, the statistical error cannot be estimated simply because each bin is not independent in Equation (9.1), and a method like simulation is necessary. Even if the spectrum passes through the top hat filter and is fitted by the sum of the reference spectrum, the data other than the peak of the line spectrum is hardly involved in improving the statistics. Because the spectrum near the peak is almost made by data which is not statistically independent of the peak. Therefor, since it is equivalent to reading the value of the peak of the line, the peak values convolved with top hat filter are given by

$$P_n = \sum_t w_t C_{n-t}, \quad (9.2)$$

where n is the peak bin number, w_t the weight of top hat filter for t-th bin, and C_{n-t} is the count of t-th bin. If Poisson distribution of C_{n-t} is approximated by a normal distribution, the dispersion σ_{P_n} of P_n is given by

$$\sigma_{P_n}^2 = \sum_t w_t^2 C_{n-t}. \quad (9.3)$$

We performed simulation with the total count number increased and investigated the change of statistical error

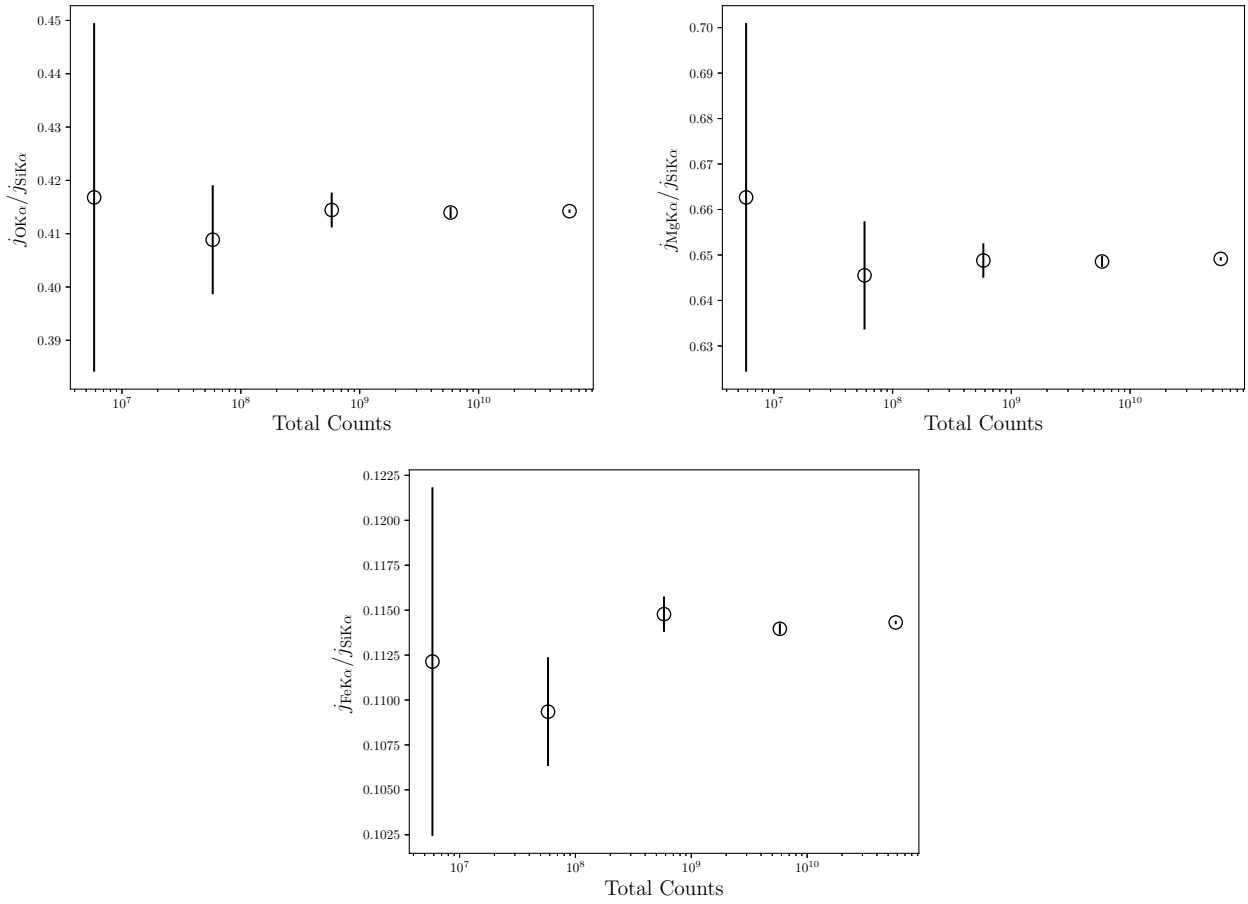

Fig. 9.3 Total counts vs. $j_*/j_{\mathrm{SiK}\alpha}$, O Kα (upper left), Mg K α (upper right), and Fe Kα (bottom)

and systematic error (Figure 9.3). The systematic error converged to roughly 10%-80% as shown in Table 9.1.

9.2.2 Continuum subtraction in TES spectra

In case of SDD spectrum, Fe L and Cu L lines are not resolved. As the result, the continuum spectrum underlying over O line is not correctly estimated. In case of TES, Fe L and Cu L lines are resolved, and we can directly see the continuum spectrum. However, generally, we do not have enough knowledge to model the continuum spectrum precisely. Ambiguity of continuum model may introduce systematic errors. We can reduce the dependence on the choice of continuum models by using narrow energy range in the model fit. We studied this possibility with two simulations. The simulation model was the olivine spectral fit model (Table 8.2). The first simulation simulated the same observation time (3000 s) as Olivine standard sample observation. Making 10000 spectra, we fitted each simulation in narrow energy band including the line as shown in Figure 9.4. The background is modeled with a power law function as given by

$$A\left(E, K, \Gamma\right) = KE^{-\Gamma}. \tag{9.4}$$

We fitted the spectra using these parameters of Equation (9.4) and the line centroid energy and the normalization factor of the line as free parameters. In Figure 9.5, a histogram of the intensity ratio to Si intensity was obtained by fitting 10000 spectrum. The histogram was fitted using a Gaussian function to find the center value μ and width σ_{FWHM} of the histogram. As a result of comparing the center value and the intensity ratio of the model,

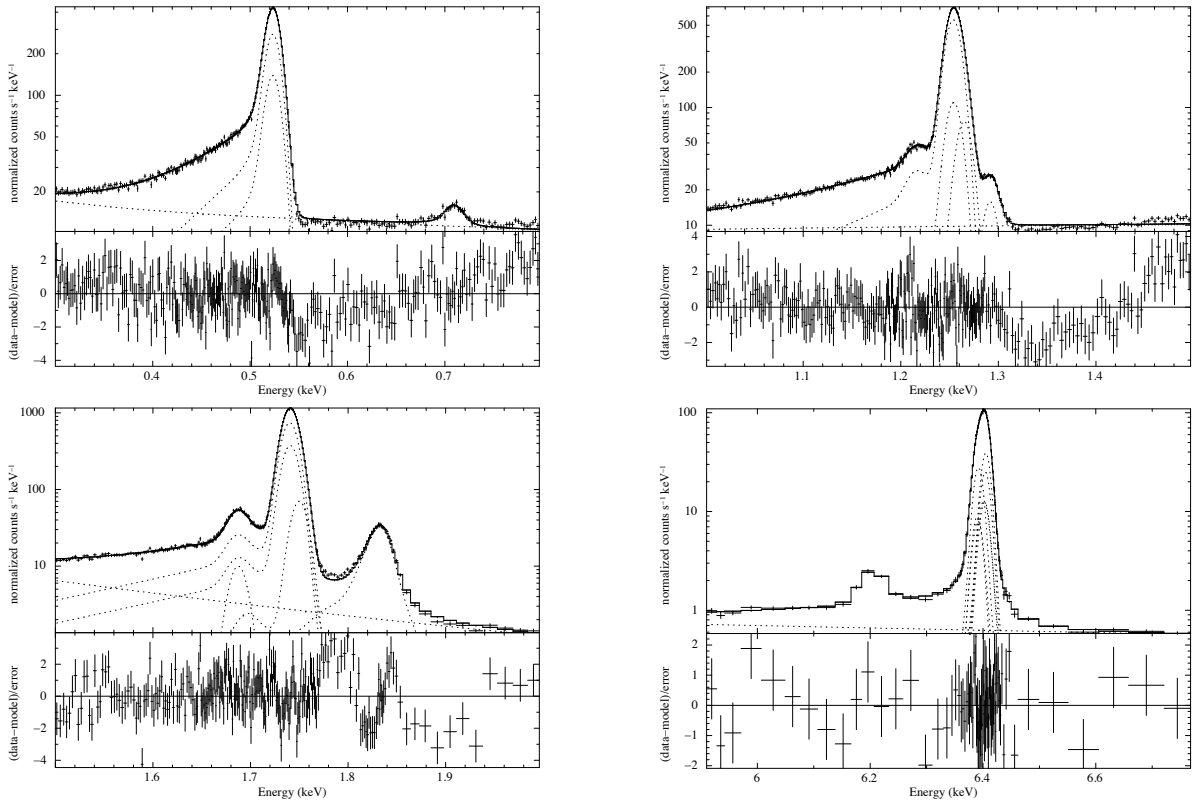

Fig. 9.4 Results of spectrum fit, OKα (upper left), MgKα (upper right), SiKα (bottom left), and FeKα (bottom right), dash line are models, see p.61

Table 9.2 Results of TES simulation, comparing simulation intensity and model intensity of the fit parameter of each line, matching within 1%

Line	Intensity ratio to Si Kα Fit results of simulation	Model Intensity ratio to Si Kα	Systematic error (|Simulation − Model| /Model × 100)
OKα	5.75	5.79	0.81%
MgKα	0.550	0.552	0.40%
SiKα	1	1	-
FeKα	0.187	0.186	0.04%

they matched within 1%. The spread of the histogram is due to the statistical error of the intensity when fitting the spectrum of 3000 s. In the second simulation, the simulation was performed by increasing the number of photons for a sufficiently long time to eliminate the influence of this statistical error as shown in Figure 9.6. We confirmed that the deviation (systematic error) between model and simulation result is less than 1% under the condition that it is not affected by statistical error (Table 9.2). From this result, we conclude that taking advantage of the superior energy resolution, we separate an emission line, e.g. O K emission line, from its adjacent lines, e.g. Fe L and Cu L lines for O K, and that we determine the line intensity without systematic errors arising from the ambiguity of underlying continuum, Fe L and Cu L emission lines.

9.3 Summary

We compared the systematic error by analysis method between SDD and TES using simulation which is the comparison assuming ideal SDD and TES situations. As a result, the systematic error of the existence ratio of

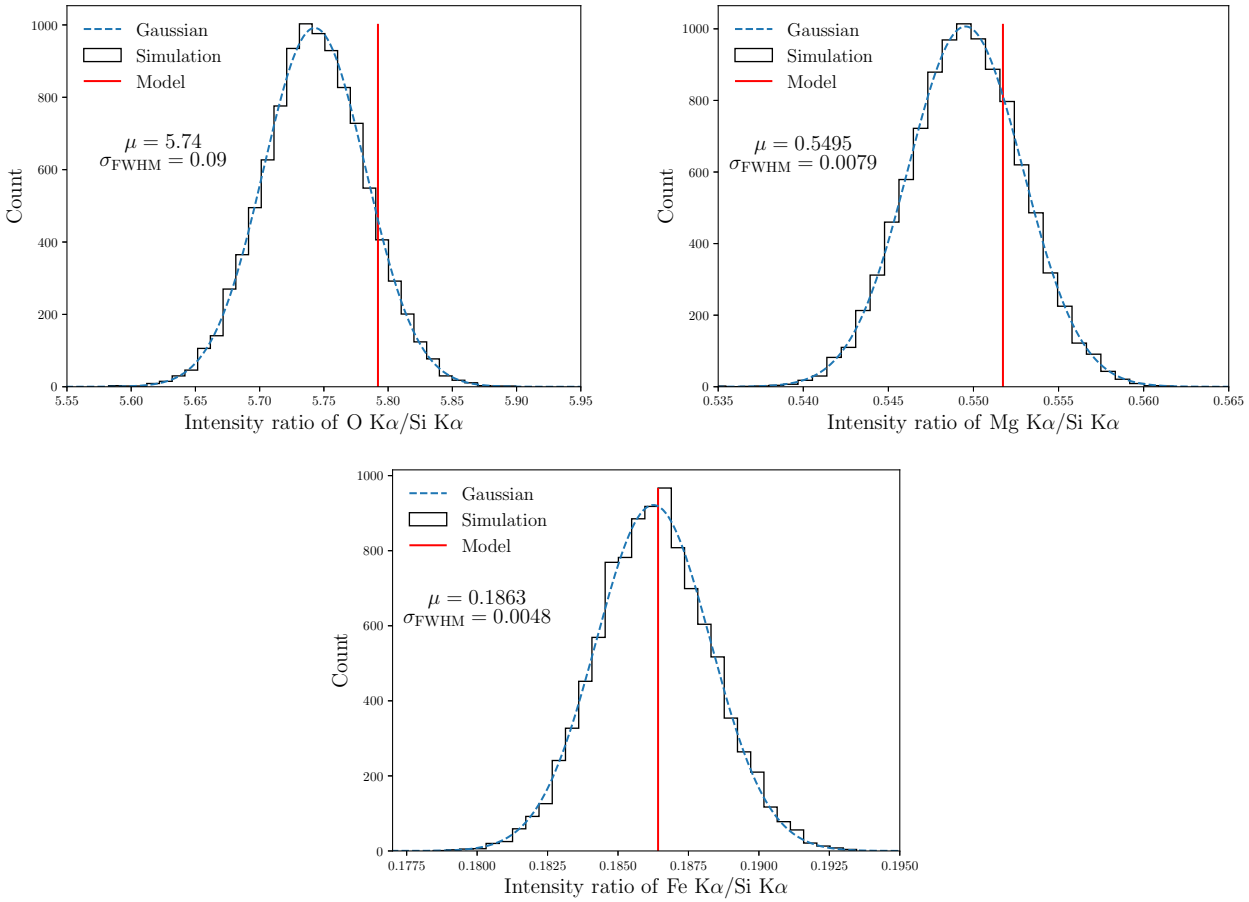

Fig. 9.5 Results of 10000 simulation events. The histogram is the simulation results, the red solid line is the ratio of the line intensity of each model to the line intensity of Si model, and the dash line is Gaussian function of the center μ and the width σ_{FWHM} after fitting to the histogram.

oxygen and silicon is about 10% as shown in Table 9.1. On the other hand, in the spectrum obtained by TES, it was shown that the systematic error can be determined with less than 1% for the ratio of oxygen to silicon, even if we do not know the exact spectral shape of the background.

This simulation does not consider influence of the shift of the response function, and of shift of energy calibration of each pixel. In order to reduce these factors, it is necessary to improve the precision of the response function and the accuracy of energy calibration.

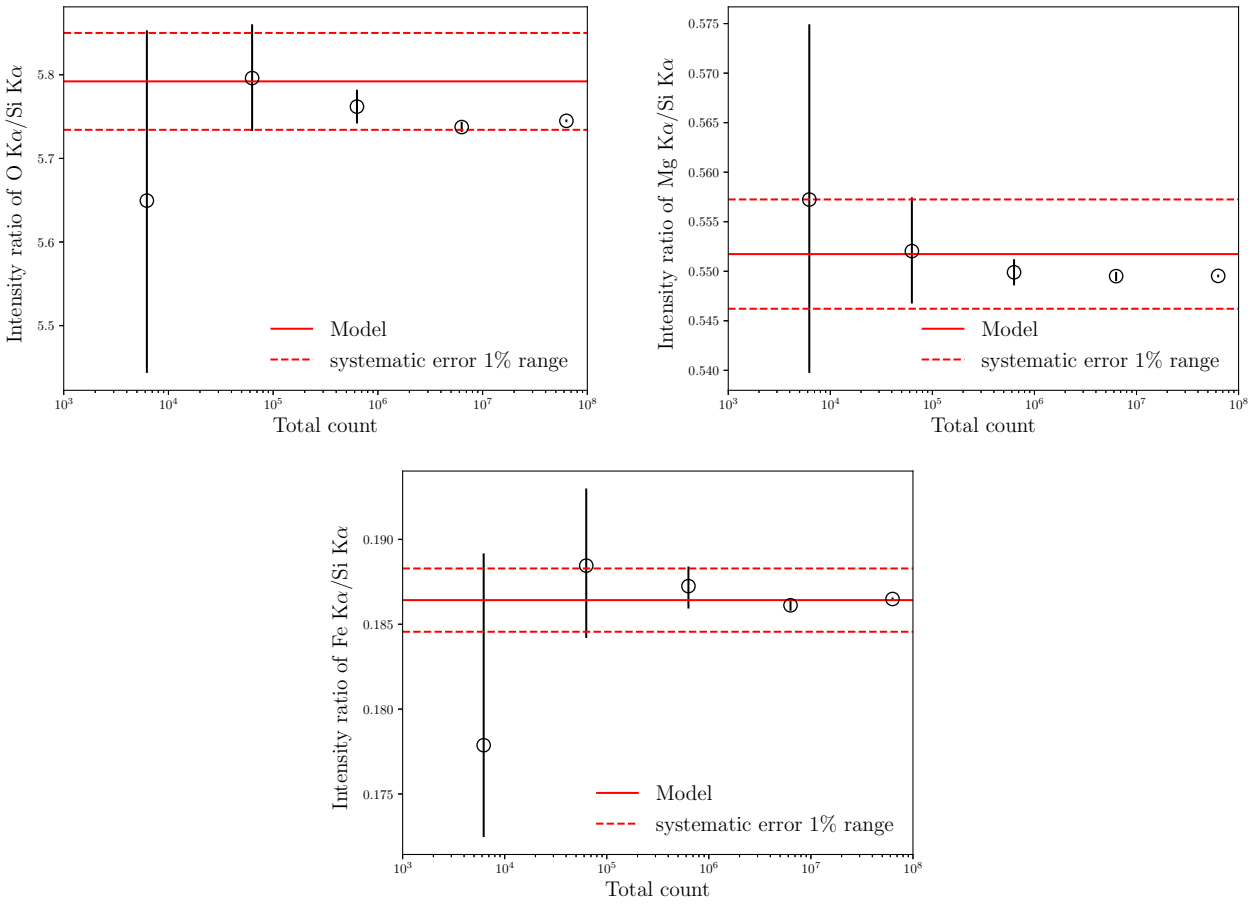

Fig. 9.6 Intensity ratio vs. total count for each model from the simulation. The red solid line is the ratio of the line intensity of each model to the line intensity of Si model, and the red dashlines show ± 1% range for the red solid line.

Chapter 10

Conclusions

10.1 Conclusions

In this thesis, we have developed a high energy-resolution EDS system for an STEM utilizing a TES microcalorimeter array. Although the system is useful for wide varieties of material analysis, our main target is an application to astromaterials, where precise determination of O to Si ratio is one of the key parameters for the understanding of history of silicates in planetary formation. Requirements for the STEM EDS are a high energy-resolution of < 10 eV FWHM, high counting rate capability (> 5 kcps), and a wide energy range (0.5-15 keV). Through the researches of this thesis, we obtained the following achievements:

1. A good energy resolution, a fast response, and wide energy coverage are contradictory requirements for a TES X-ray microcalorimeters. Adjusting the superconducting temperature, thickness of the X-ray absorber, we found a solution which mitigates all the requirements with margin adopting an 8×8 format, 64-pixel array.
2. The TES microcalorimeter array designed and fabricated in house showed a good energy resolution of 4.8 eV in the laboratory under low counting-rate environment.
3. The superconducting flip-chip bonding technology used to mount 64 SQUID array amplifiers on the detector head had problems and we did not solve them thoroughly. As the results, we operated only 19 pixels on STEM.
4. The energy resolution was found to degrade with increasing counting rate. By optimizing the record length used for pulse shape analysis, we obtained a FWHM energy resolution of 9.5 eV with a throughput counting rate of 4.5 kcps, and 11.0 eV at 5.0 kcps, even with 19 pixels.
5. In the energy spectrum of the Olivine standard sample obtained with the STEM-TES-EDS, we detected Cu Lα line and separated Mg Kβ and Si Kβ lines. We further detected Mg and Si absorption edge structures in the continuum spectrum. All of these were impossible with conventional semiconductor-base EDS. These results prove that spectroscopy with TES has a high potential that opens up a new window for material analysis.
6. Detection of X-ray from 0.5 keV (O Kα) to 8.0 keV (Cu Kα) was confirmed using the TES sample and Olivine sample. We cannot confirm the high energy range of 9 keV - 15 keV.
7. For quantitative analysis of TES spectra, we constructed a response function of the detector system. We found we need three components in the response matrix (= pulse height re-distribution function); a main peak, sub peak, and low pulse height tail. The first two components are modeled with a Gaussian function, while the latter with a power-law function multiplied with a theta function. The sub peak is considered to arise from the X-ray absorption by the TES, while the low pulse height tail is likely due to electron loss from the absorber. For the efficiency function of the detector, we take into account the throughput of the

capillary optics, X-ray transmissions of entrance window and optical blocking filters and the absorption efficiency of the Xray absorbers. In order to calibrate the response function, we utilized the X-ray spectrum of Olivine standard sample obtained with the STEM-TES-EDS. Some of the parameters in the response function, e.g. reflectivity parameter of the capillary optics, were determined by spectral model fitting to the Olivine spectrum.

8. The K factors were estimated using the X-ray spectrum of the Olivine standard sample. By utilizing the K factors to the SiO_2 spectrum obtained with the STEM-TES-EDS, we obtain an O to Si ratio which is correct within the statistical errors of the experiment.
9. From Monte-Carlo simulations, we found an EDS analysis using a conventional semiconductor-based detector ($\Delta E \sim 120$ eV), e.g. SDD, and a conventional method which is the top hat filter will contain about 10% of systematic error in O/Si ratio for Olivine. This is due to contaminations of Fe L and Cu L lines, and underlying continuum emission.
10. From Monte-Carlo simulations, we found that the systematic error in O to Si ratio is at most 1% with TES EDS ($\Delta E \sim 10$ eV) for Olivine independent of the continuum models, assuming ideal conditions.

For the first time in the world, we have developed a high-energy resolution EDS system and proved its high potential for qualitative analysis of astromaterial. Presently only 19 pixels are operating. If we make all 64 pixels to operate, the system will be more than 3 time faster, and becomes more useful. The problem is in flip-chip bonding process, and thus it can be fixed in near future. Then we will start using the system for various real applications, in particular, analysis of silicate in astromaterial.

A

Lines included in the model fits

[*1] Energy, Natural width, and intensity are not found in literature

Table A.1 Energy, Natural width, and intensity of K lines of O, Mg, Al, Si, Fe, Cu

Element	Peak	Energy (eV)	Natural width (eV)	Intensity
O	α_1	523.09	0.13	0.334
	α_2	523.13	0.13	0.666
Mg	α_1	1254.39	0.33	0.149
	α_2	1254.14	0.33	0.749
	satellite[*1]	1265.20	0.33	0.102
Al	α_1	1486.94	0.43	0.578
	α_2	1486.52	0.43	0.289
	α'	1492.94	1.34	0.019
	α_3	1496.85	0.96	0.069
	α_4	1498.70	1.25	0.036
	α_5	1507.4	1.5	1.07×10^{-10}
	α_6	1510.9	0.9	0.008
Si	α_1	1739.98	0.49	0.312
	α_2	1739.38	0.49	0.620
	satellite[*1]	1749.18	0.49	0.058
Mn	α_{11}	5898.853	1.715	0.353
	α_{12}	5897.867	2.043	0.141
	α_{13}	5894.829	4.499	0.079
	α_{14}	5896.532	2.663	0.066
	α_{21}	5899.417	0.969	0.005
	α_{22}	5887.743	2.361	0.229
	α_{23}	5886.495	4.216	0.110
	β_a	6490.89	1.83	0.254
	β_b	6486.31	9.40	0.234
	β_c	6477.73	13.22	0.234
	β_d	6490.06	1.81	0.164
	β_e	6488.83	2.81	0.114
Fe	α_{11}	6404.148	1.613	0.278
	α_{12}	6403.295	1.965	0.182
	α_{13}	6400.653	4.833	0.106
	α_{14}	6402.077	2.803	0.094
	α_{21}	6391.190	2.487	0.207
	α_{22}	6389.106	2.339	0.066
	α_{23}	6390.275	4.433	0.065
	$L_{\alpha 1}$	708.38	1.87	0.5277
	$L_{\alpha 2}$	707.46	1.87	0.4723
Cu	α_{11}	8047.837	2.285	0.579
	α_{12}	8045.367	3.358	0.080
	α_{21}	8027.993	2.666	0.236
	α_{22}	8026.504	3.571	0.105
	β_a	8905.532	3.52	0.485
	β_b	8903.109	3.52	0.248
	β_c	8908.462	3.55	0.110
	β_d	8897.387	8.08	0.100
	β_e	8911.393	5.31	0.055
	$L_{\alpha 1}$	929.71	5.06	0.517
	$L_{\alpha 2}$	929.38	5.06	0.483
	$L_{\beta 1}$	1019.1	5.19	0.502
	$L_{\beta 2}$	1022.0	5.19	0.498

B

Fabrication Process

In this appendix, the fabrication process of the TES microcalorimeter is detailed. Table 5.3, Figure B.1 and Figure B.2 show the fabrication process flow of the TES microcalorimeter. We describe the details of the resist and each process from the selection of the Si wafer.

B.1 Silicon wafer

In order to fabricate a semiconductor process, it is necessary to select an optimal Si wafer. Si wafers have various sizes and thicknesses. In the semiconductor IC (integrated circuit) process, in order to improve productivity, an 8- to 12-inch size is mainstream. However, in the fabrication of the TES microcalorimeter, we selected 4-inch wafers, due to the limitations of the equipment used for fabrication, and a thickness of 300 μm, due to past experience. Since the TES microcalorimeter has a thermal link, it is necessary to form a silicon nitride film ($SiN_x = 1$ μm) on the Si substrate as a membrane structure.

We selected a 4-inch silicon wafer with 300 μm thickness and $SiO_2/SiN_x (= 0.5/1.0$ μm) films formed on the

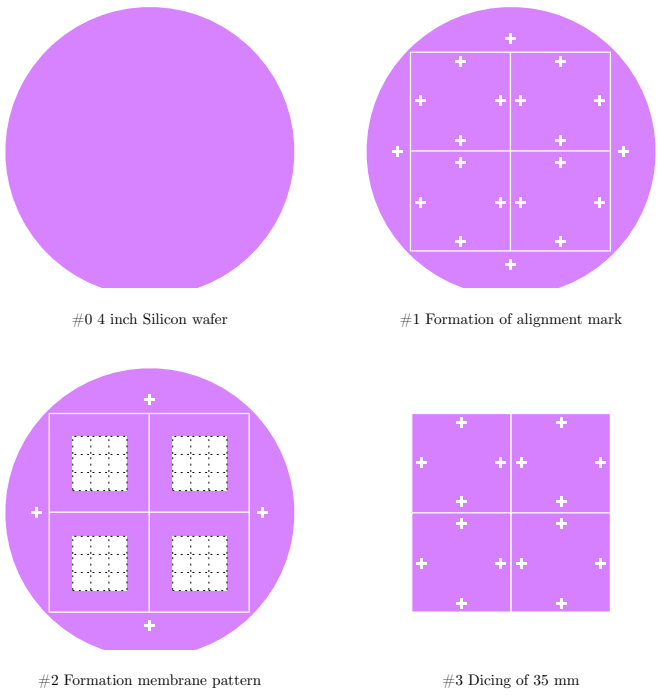

Fig. B.1 4 inch silicon wafer process (#0 - #3)

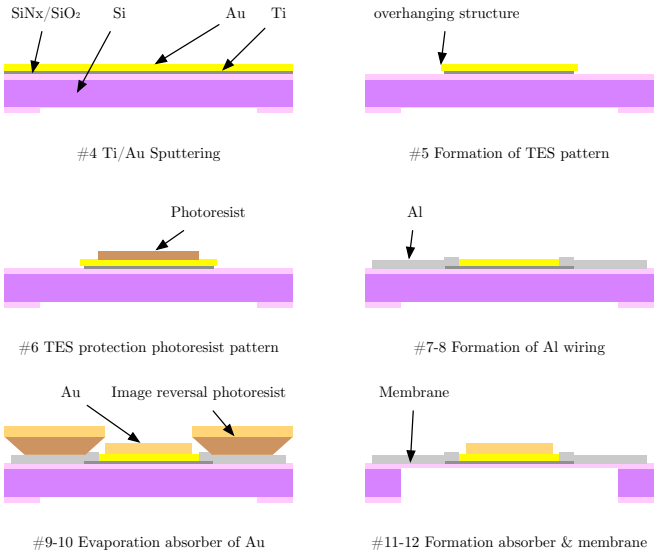

Fig. B.2 Fabrication process (#4 - #12)

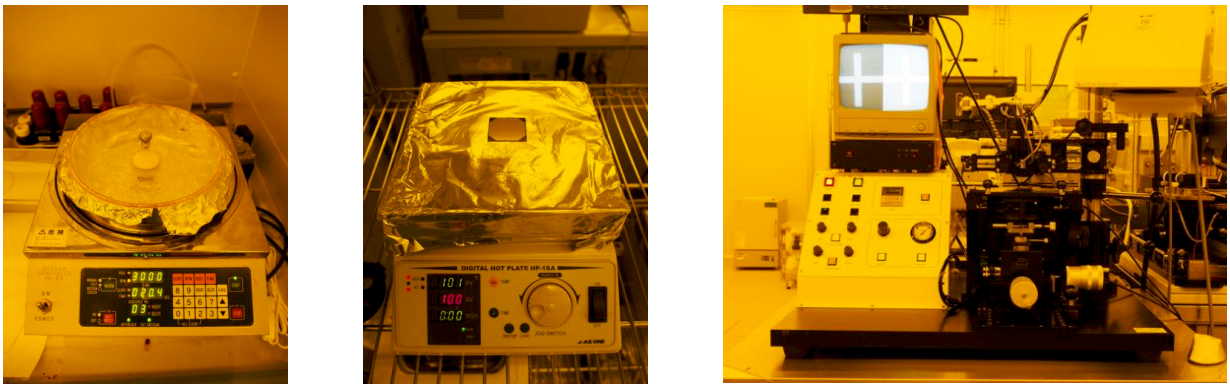

Fig. B.3 Spin coater (left), Hot plate (center), Contact aligner of MISAKA MA-101 (right)

both sides of the silicon wafer. The SiO_2 film serves as a stopper for dry etching in the final process (see Sub-Section B.3.5). The SiN_x film plays the role of forming a weak thermal link between the calorimeter and the thermal bath. It is formed by the thin-film growth method by chemical reaction in gas phase under low pressure, i.e., Low Pressure Chemical Vapor Deposition (LPCVD). In the growth of the SiN_x film by this process, the reaction with dichlorosilane and ammonia is generally used at a temperature of $700 - 800$ ℃, and the advantage of good film homogeneity is an advantage. The chemical equation is given by

$$3SiCl_2H_2 + 4NH_3 \rightarrow Si_3N_4 + 6HCl + 6H_2.$$

B.2 Photo-lithography

Photolithography is a technique used in semiconductor processing technology to transfer a pattern such as a circuit by irradiating a pattern (photomask) as an original onto a Si substrate coated with a photosensitive agent (resist). Photolithography is used to process fine patterns such as IC and LSI. Currently, super-LSI technology produces patterns of 0.1 μm or less. Photolithography is used in processes such as substrate cleaning, resist

Resit type	Average thickness	Used process
Shipley series S1818G	1.8 μm	Formation of alignment, TES pattern, Al wiring pattern
Shipley series S1830G	3.0 μm	Formation of back side pattern
AZ5200NJ	7.0 μm	Formation of absorber pattern

Table B.1 Average thickness of each resist

Table B.2 Photolithographic process conditions of "S1818G"

	Time		Rotation speed (rpm)	Temperature (℃)
Spin coater	$0 \rightarrow 5$	s	$0 \rightarrow 500$	Room Temperature (RT)
	$5 \rightarrow 10$		500	
	$10 \rightarrow 15$		$500 \rightarrow 3000$	
	$15 \rightarrow 45$		3000	
	$45 \rightarrow 50$		$5000 \rightarrow 0$	RT
Leaving	5	min		RT
Post-bake	2.5	min		100
Exposure	7	s		
Developing	3	min		RT

Table B.3 Photolithographic process conditions of "S1830G"

	Time		Rotation speed (rpm)	Temperature (℃)
Spin coater	$0 \rightarrow 5$	s	$0 \rightarrow 500$	Room Temperature (RT)
	$5 \rightarrow 10$		500	
	$10 \rightarrow 15$		$500 \rightarrow 3000$	
	$15 \rightarrow 45$		3000	
	$45 \rightarrow 50$		$5000 \rightarrow 0$	RT
Leaving	5	min		RT
Post-bake	2.5	min		100
Exposure	13	s		
Developing	4	min		RT

Table B.4 Photolithographic process conditions of "AZ5200NJ"

	Time		Rotation speed (rpm)	Temperature (℃)
Pre-bake	10	min		100
Leaving	5	min		
Spin coater	$0 \rightarrow 5$	s	$0 \rightarrow 300$	RT
	$5 \rightarrow 45$	s	300	
	$45 \rightarrow 46$	s	2000	
	$46 \rightarrow 51$	s	$2000 \rightarrow 0$	
Post-bake	15	min		100
Leaving	15	min		RT
Exposure	4	s		
Reversal bake	1	min		80
	1	min		90
	1	min		100
Leaving	15	min		RT
Flood exposure	18	s		
Leaving	2	min		RT
Developing	5	min		RT

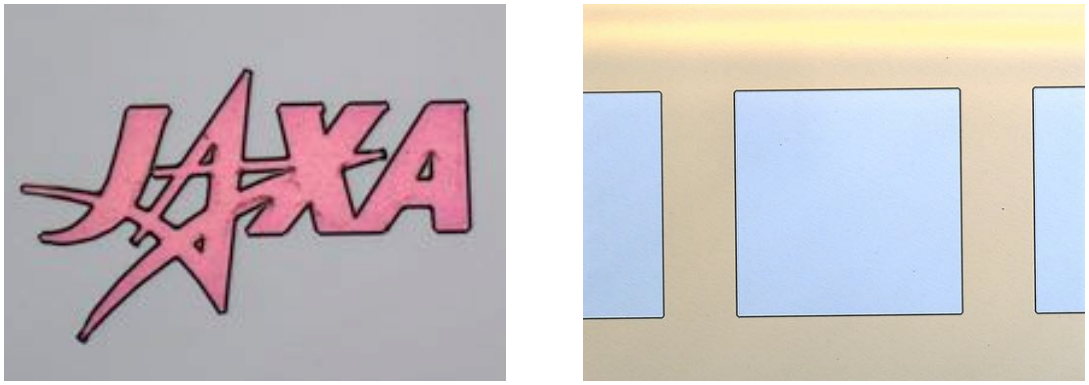

Fig. B.4 JAXA mark which is etched on SiN_x (left), membrane pattern which is etched on SiN_x (right)

coating pretreatment, resist coating, pre-baking, exposure, and development.

It is important to apply the resist with a uniform thickness. Therefore, we use a spin coater (Figure B.3 left), apply resist to the wafer, and rotate the substrate at high speed to form a uniform resist film. Since the wafer reacts with moisture in the atmosphere and is hydrophilic, adhesion with a hydrophobic resist is poor. To remove moisture from the substrate and improve adhesion to the resist, baking is performed using a hot plate (Figure B.3 center) before resist application. After that, HMDS (hexamethyldisilazene, $[(CH_3)_3Si]_2NH$) is first applied, then the OH group (hydroxyl group) on the Si surface is substituted with a methyl group (CH_3), and the wafer is changed from hydrophilic to hydrophobic. In this fabrication process, three types of photoresist ("S1818G," "S1830G," and "image-reversal resist") are used. The photoresist is a film that is sensitized and changed by UV light. There are two types of photoresist: positive type and negative type. The positive type resist is used in most processes, whereas image-reversal resist is a special type of negative resist. The conditions of each resist are shown in Table B.2, Table B.3, Table B.4, and Table B.1 shows the average thickness of each resist. The wafer coated with the resist is lightly baked in a process called "prebake." This is done to evaporate the solvent dissolved in the resist to form a dense film. For exposure, a double-sided mask aligner (Figure B.3 right) is used. Tetramethylammonium hydroxide (TMAH) is used for development after exposure.

B.3 Fabrication process flow

B.3.1 Formation of alignment mark in 4-inch wafer

Alignment marks are formed on both sides of a 4-inch wafer. Alignment marks are cross marks and are necessary at the stage of advancing the process on both sides. Four types of marks are formed in this process: triangle marks that allow you to see the top and bottom of the wafer, 35 mm square guidelines for dicing the board, the "JAXA" mark defining the orientation of the element (Figure B.4 left), the alphabet defining the position on the 35 mm square board, and the matrix number of each element in the chip. Since the size of the membrane does not have a margin as compared with the size of the element as the element becomes finer, alignment between the front side and the back side needs to coincide with precision of several μm. Therefore, the position of the alignment marks formed on both sides is set as far as possible within the range where it operates with the camera of the double-sided aligner device, so the accuracy of alignment is improved.

The alignment mark is formed by a protective resist patterning with photolithography and a dry etching process with a reactive ion etching (RIE). In this process, the nitride film is removed by using an inductively coupled plasma (ICP) type RIE apparatus manufactured by Sumitomo Precision Industries, Ltd. Since the basic reaction

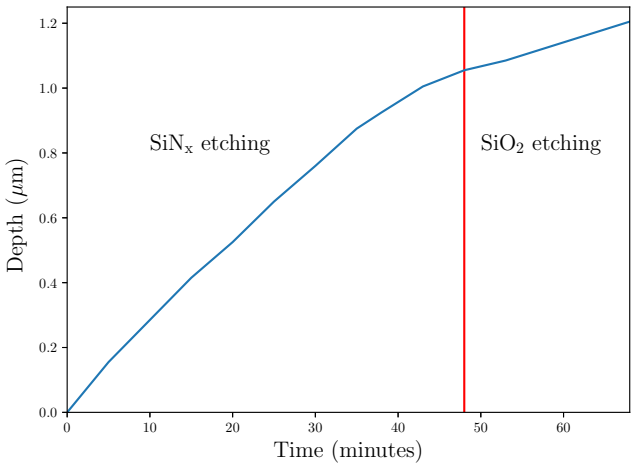

Fig. B.5 Etching rates of isotropic etching

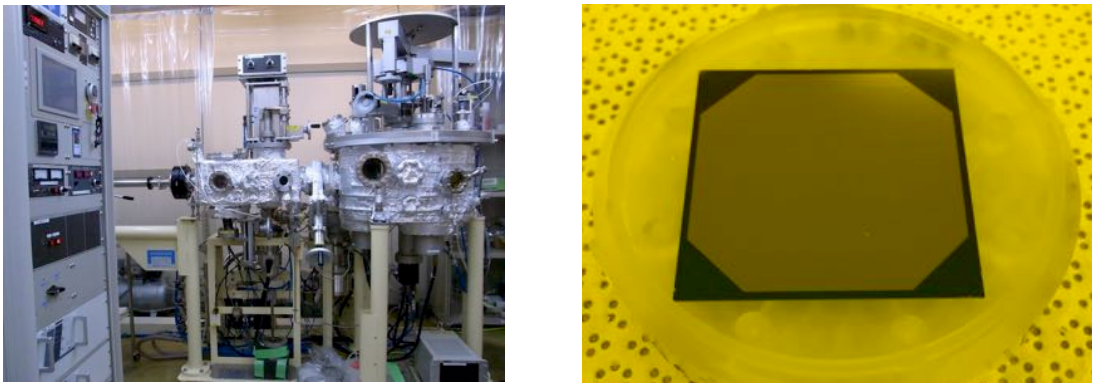

Fig. B.6 DC magnetron sputtering for Ti/Au sputtering (left), Ti/Au deposited on SiN_x (right)

mechanism is based on Si, details are described in subsection B.3.5.

In this process, the depth of the alignment mark is about 0.5 μm, and a process cycle is 20 cycles using the ICP process recipe "TES_HIGH_SPEED" (see subsection B.3.5 for details). And we remove the SIN_x film and the SIO_2 film on the back surface. SiN_x is removed by isotropic etching with the ICP using S1830G as an etching mask. The duration of isotropic etching by ICP is about one hour. Figure B.5 shows the etching rates of SINx and SIO2 by isotropic etching. Then, in order to reduce the waste liquid of the subsequent process (Figure B.4 right), a 4-inch wafer is cut into four pieces each of 35×35 mm^2. And we put the cut substrate on "Pure Etch ZE255," which is a hydrofluoric acid type, for about 7 minutes to remove the SiO_2.

B.3.2 Formation of TES pattern

The TES is the bilayer of Ti and Au, deposited on SiN_x by high-vacuum DC magnetron sputtering with exhaust pressure kept at 10^{-8} Pa in at the Tokyo Metropolitan University (Figure B.6 left). In this apparatus, after depositing Ti, the substrate is manually moved just above the target of Au to deposit Au. Because of this, the time to move is about 120 to 180 s. The sputtering rates of Ti and Au are 60 nm/min and 172 nm/min, respectively. Figure B.6 (right) shows the wafer after the Ti and Au are deposited on SiN_x.

The pattern of TES is formed by wet etching using resist S1818G. For the etchant (etching solution) of Ti and Au, a hydrogen peroxide-water solution heated to 60 ℃ and Aurum (iodine solution, manufactured by Tokyo

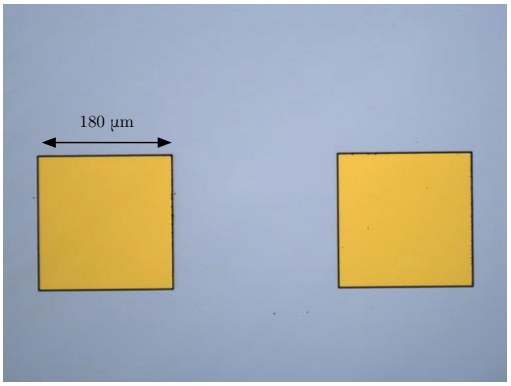

Fig. B.7 Formed TES pattern, the TES pattern size is 180 μm

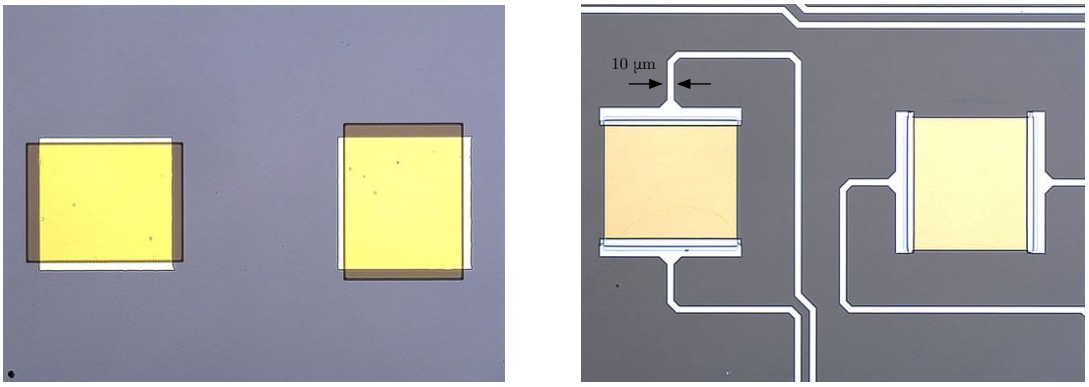

Fig. B.8 Protection resist pattern (left), Al wiring pattern (right)

Ohka Kagaku Co., Ltd.) are used. The etching rate of Ti is 3 nm/min, and the etching rate of Au is 500 nm/min. Since the etching rate of Au is fast, it takes 10-15 seconds. In order to suppress the excess component noise coming from the boundary condition of TES, the etching time of Ti is set to 3 hours, and side over-etching is performed to make an overhang structure (Figure B.7).

B.3.3 Formation of wire pattern

The Al wiring for the TES readout is formed by sputtering, and pattern formation of the wiring is performed by a minimizing process of wet etching and lift-off. As shown in Figure B.8, patterning with a resist of S1818G is performed to protect the area other than the wiring area on the TES. Then, in order to prevent the Al/Au/Ti (Super/Normal/Super:SNS bond) structure considered from being the cause of the two-stage transition of TES, Au is scraped and Ti is bared, with removal of dust on the substrate by reverse sputtering. The scraped rate of Au with reverse sputtering is 1 nm/s. Then, Al is deposited on the substrate by RF magnetron sputtering (Figure B.9). In our apparatus, the Al film deposition rate is 115 nm/min at an applied voltage of 300 W. After Al is deposited, a wiring pattern is formed using resist S1818G, and wet etching is performed. For etchant, Al is etched as it is after development using the TMAH, which is a developer for resist. Then, removal of protective resist and lift-off of Al are performed at the same time (Figure B.8 right). If it is difficult to remove by resist alteration, O_2 ashing is applied by RIE to remove residual resist.

Fig. B.9 RF magnetron sputtering (CANON ANELVA L-210S-FH)

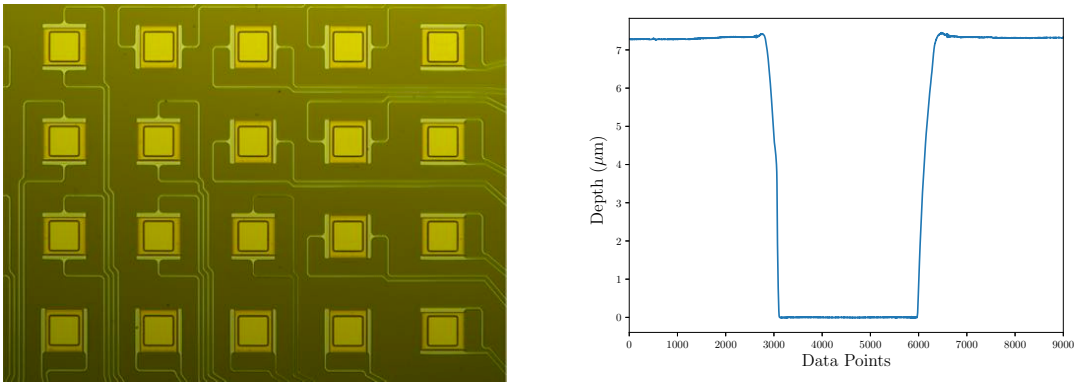

Fig. B.10 Deposition of image reversal resist (left), depth measured using the stylus type film thickness meter (right)

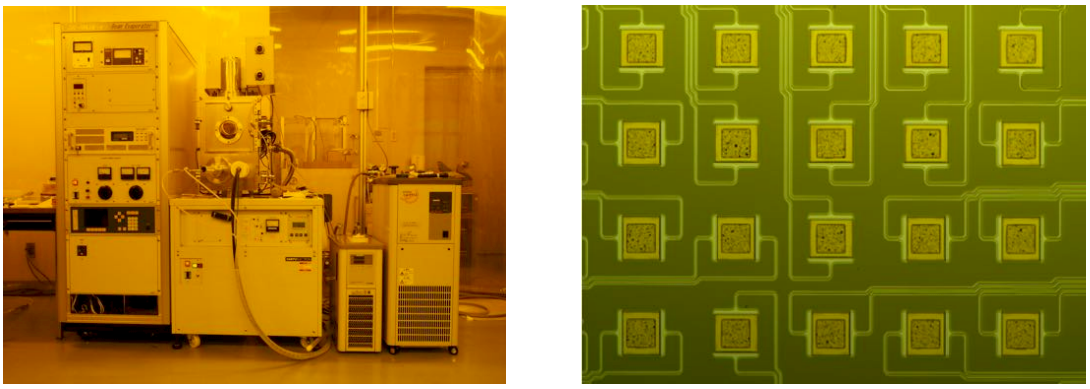

Fig. B.11 EB evaporation apparatus (SANYU Electron SVC-700LEB), deposition of Au (right)

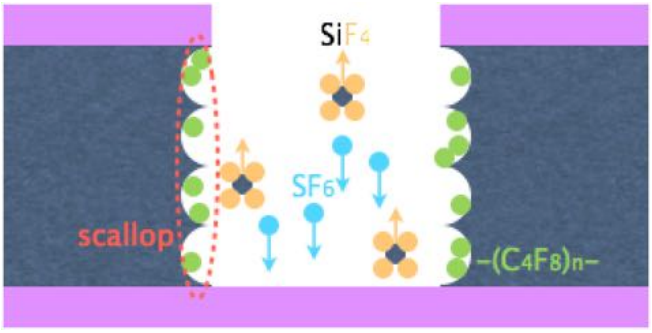

Fig. B.12 Conceptual diagram of the Bosch process (left), External view of DRIE (left)

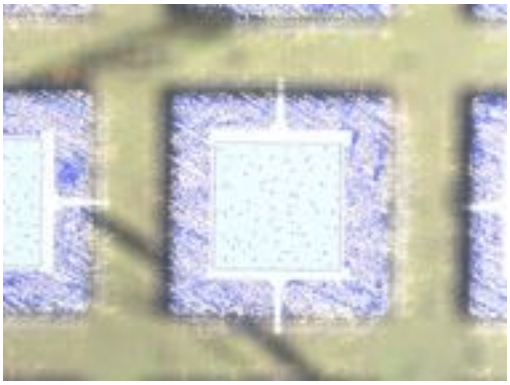

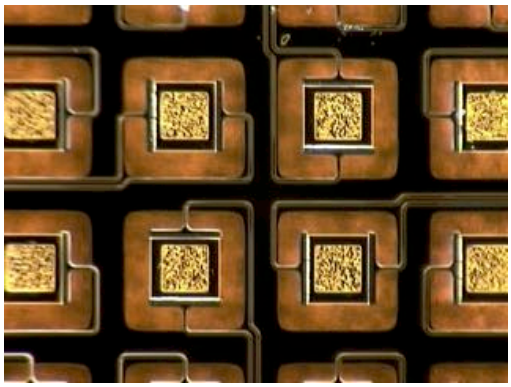

Fig. B.13 Microphotograph from the back side after DRIE (left), Microphotograph from the front side (left)

B.3.4 Formation of absorber

An Au absorber is formed by electron beam (EB) evaporation apparatus (Figure B.11 left), and a pattern is formed by lift-off process. The thickness of the absorber formed by the lift-off process is limited by the thickness and the shape of the resist. The shape is preferably reverse tapered, and it is desirable that the thickness is larger than the target film thickness. From a number of tests, we found the image reversal resist to be optimal. In addition, we successfully formed an about 7 μm thick image reversal resist from many tests, as shown in Figure B.10 (see Figure 5.8 for details). Then, the Au absorber was deposited by EB evaporation apparatus, as shown in Figure B.11 (right). In order to suppress the thermal load, evaporation was deposited by divided into four times.

B.3.5 Formation of membrane on the backside of chips

Finally, a membrane structure is formed to connect the thermal bath and the TES with a weak thermal link. For membrane formation, Deep-RIE (DRIE) is used to perform anisotropic etching (high-aspect etching), which keeps the verticality of the Si side face. SF_6, serving as a reactive gas for etching, generates a radical F^* when a variable magnetic field is applied due to high voltage and high frequency in the chamber. The generated radical

Table B.5 "TES-High_Speed" one-cycle recipe

	Gas	Power (W)	Time (s)	Flow rate (sccm)	Pressure (Pa)
Etching	SF_6	2600	3.0	550.0	9.0
Etching (boost)	SF_6	2600	6.4	550.0	18.0
Passivation	C_4F_8	1000	3.0	400.0	8.0

Table B.6 1 cycle recipe for isotropic etching

	Gas	Power (W)	Time (s)	Flow rate (sccm)	Pressure (Pa)
Etching	SF_6	1500	free	200.0	-

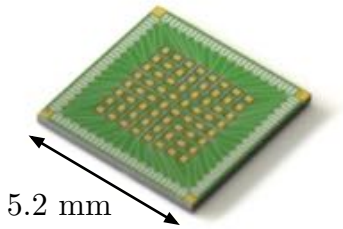

Fig. B.14 Fabricated 64 pixel TES microcalorimeter chip

F^* is accelerated by the potential difference from the substrate at the cathode and collides with the substrate. Si atoms fly due to the collision with the F^* atom, and the hand of bonding between Si atoms reacts with F^* to become SiF_4 and vaporize. In order to prevent side etching of the side face of Si, C_4F_8 polymer is introduced as protective film, or alternately, SiF_4. A method of simultaneously performing etching and protection is a process capable of realizing a deep aspect with a high aspect ratio, as shown in Figure B.12. Since the reaction rate of SF_6 is different from that of Si and SiO_2 by an etching selectivity ratio of 50-200 times or more, SiO_2 is used as a stopper. In the element to be fabricated, since the region to be etched is dispersed in the substrate, a difference in reaction rate occurs in each part. However, owing to the oxide film, excessive etching can be applied, eliminating the difference in reaction rate. Since SiN_x and SiO_2 in the membrane forming region are excluded at the beginning of the process, SiN_x and SiO_2 on the surface are used as etching masks. We are performing etching using two types of recipes. One is the isotropic etching recipe used for etching SiN_x, and the other is "TES_High_Speed" used for Si etching. Table B.5 and Table B.6 show the setting of DRIE. The recipe of "TES_High_Speed" can etch Si at a rate of 3.7 nm/cycle. Since Si of TES is 300 μm, after 75 cycles, the dry etching is performed up to 300 μm under observation with an optical microscope. A microphotograph after DRIE is shown in Figure B.13.

In this production, at the same time as the membrane is dry-etched, the groove between the 64-pixel TES chips is also dry-etched to separate the chips. At the time of etching, the 35 mm-square substrate is placed on the base, and oil is dropped between the pedestal and the substrate to improve heat conduction. The chip is detached in acetone, and cleaning is carried out with first with IPA and secondly with pure water to complete the process. The overall view of the fabricated chip and the enlarged view of the microscope are shown in Figure B.14.

C

Details of each pixel

C.1 Set up of Experiments of TES and SQUID

Table C.1 Experimentally set SQUID and TES bias current, voltage offset and feedback back current, an operating point (FB current or voltage offset) that stabilizes the FLL was chosen at 90 mK of bath temperature

Unit	channel	SQUID bias (μA)	TES bias (μA)	V offset (mV)	ϕ offset (μA)
1	1	17.0	175	29.0	118.1
	2			35.0	111.3
	3			27.0	123.6
	4			25.0	112.3
	5			23.0	125.0
	6			35.0	106.1
2	3	17.0	200	35.0	116.3
	4			35.0	127.0
	5			35.0	116.1
5	1	16.0	210	28.0	135.1
	2			28.0	105.9
	3			22.0	126.6
6	1	17.0	175	22.0	115.8
7	1	17.0	175	34.0	133.0
	2			30.0	129.0
8	2	18.0	170	35.0	105.8
	4			40.0	124.5
	5			40.0	100.0
	6			35.0	106.6

C.2 Φ–V

ch1

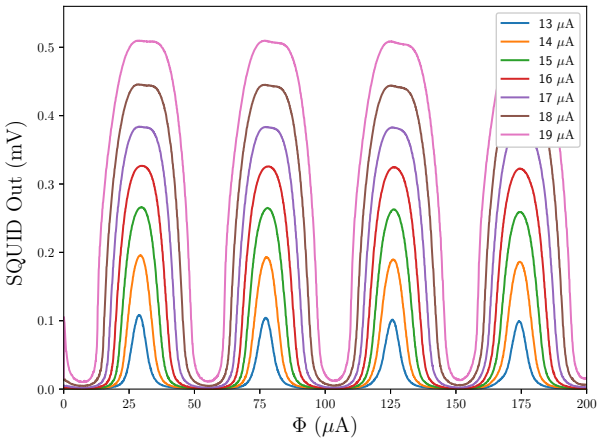

ch2

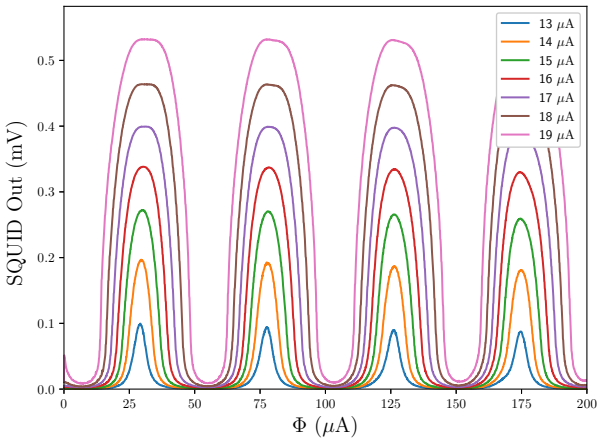

ch3

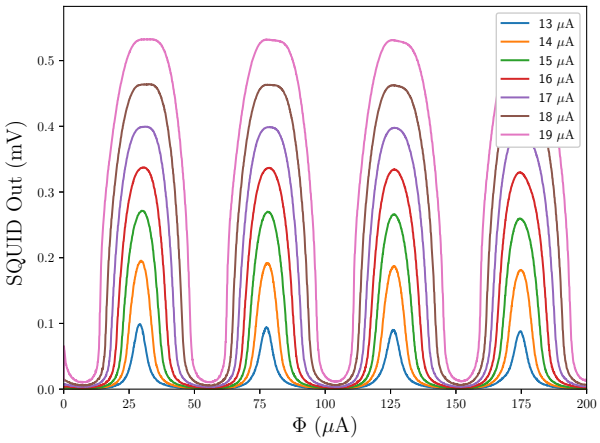

ch4

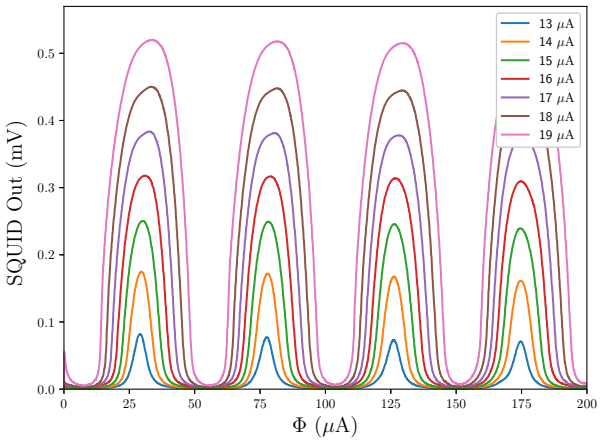

ch5

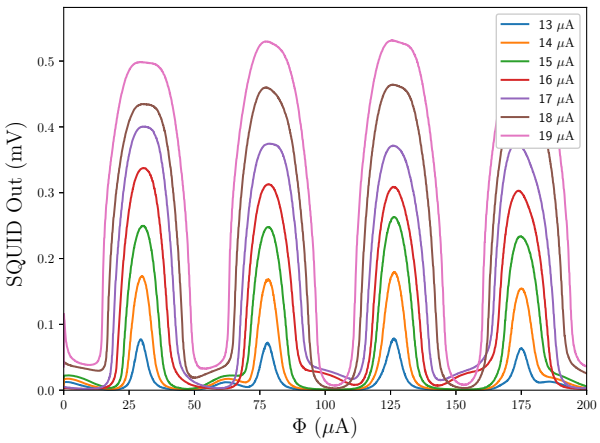

ch6

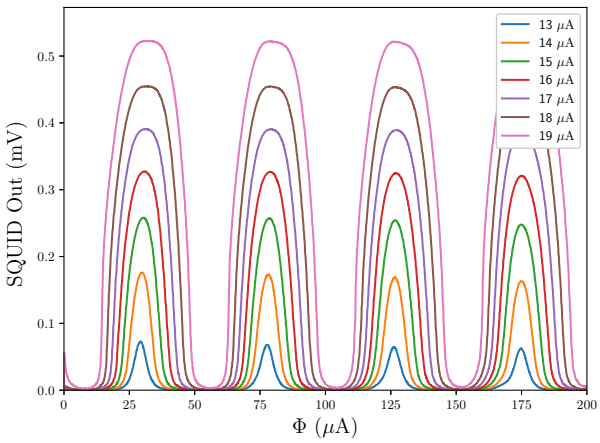

ch7

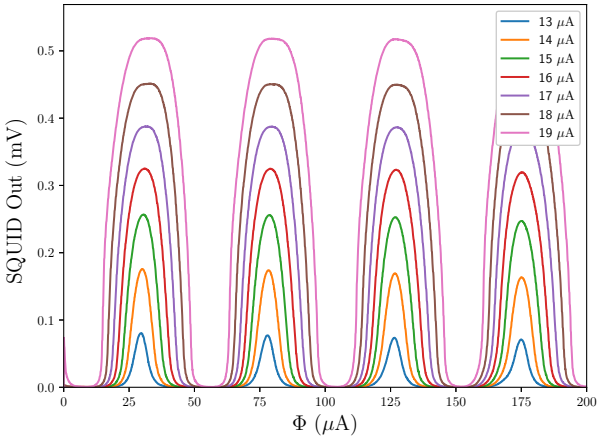

ch9

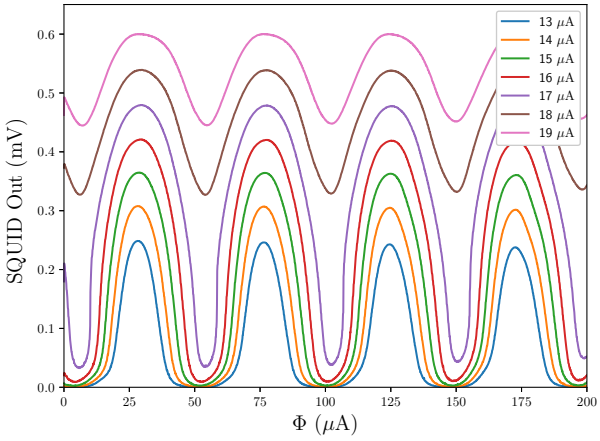

ch10

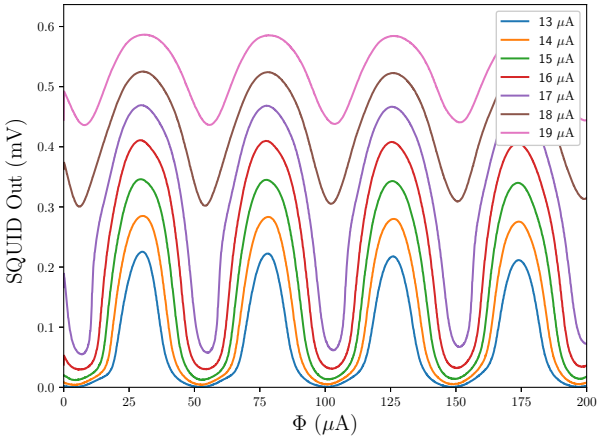

ch11

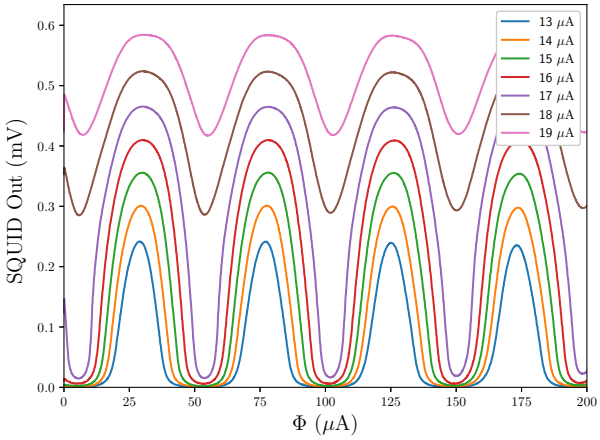

ch12

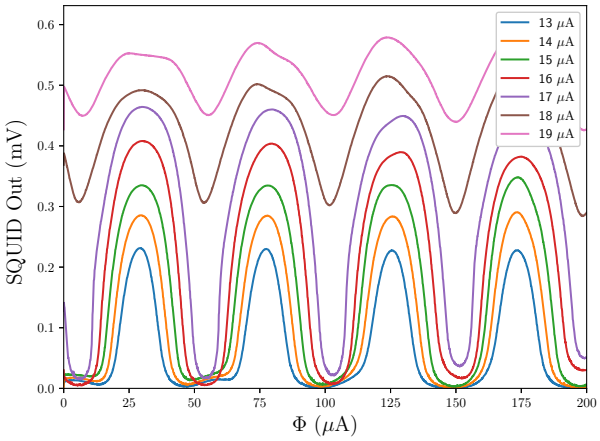

ch13

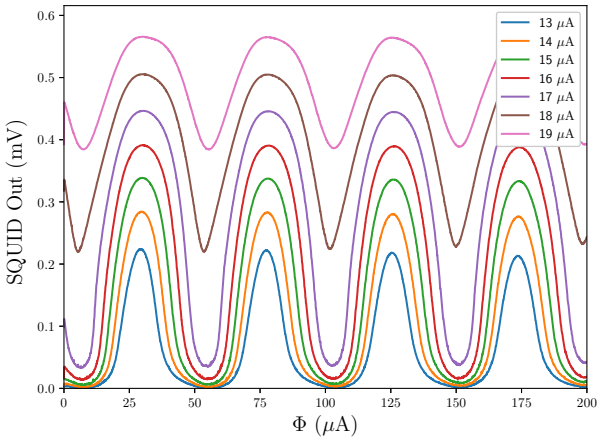

ch14

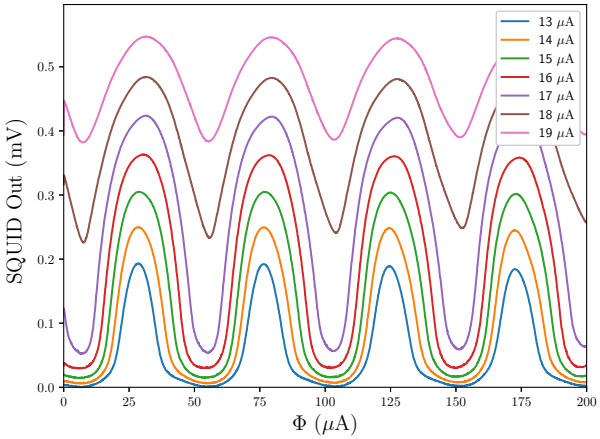

ch17

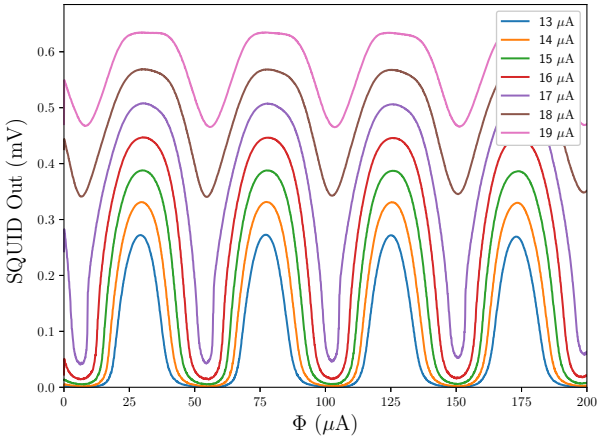

ch18

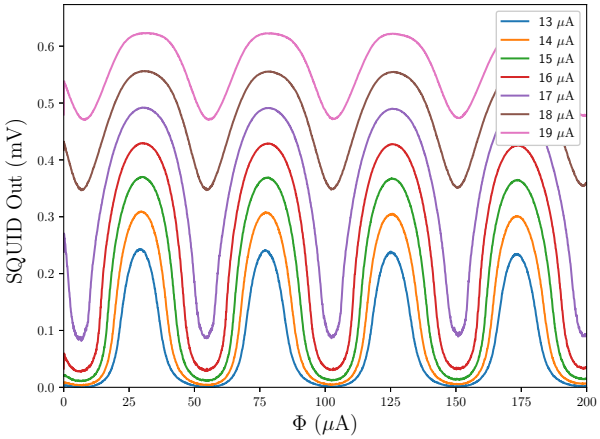

ch19

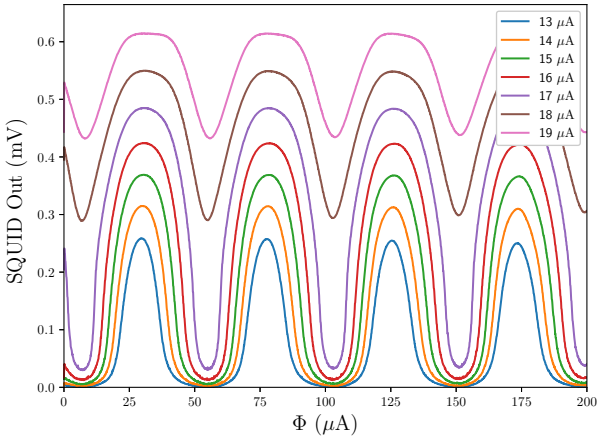

ch20

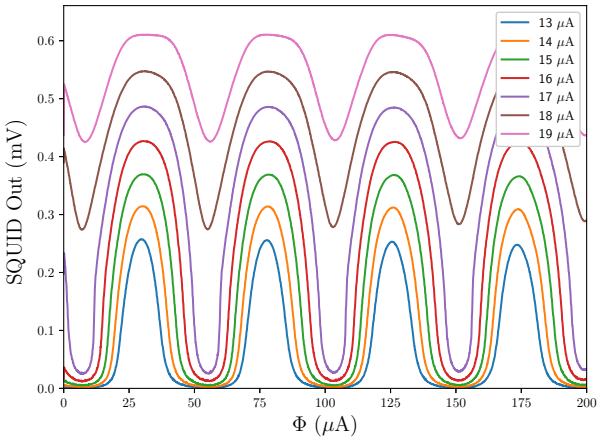

ch21

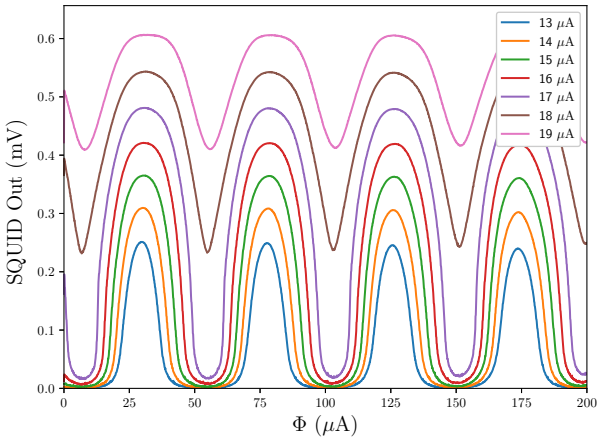

ch22

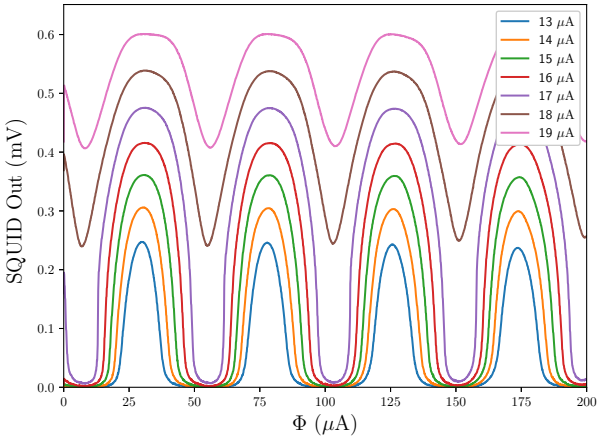

ch23

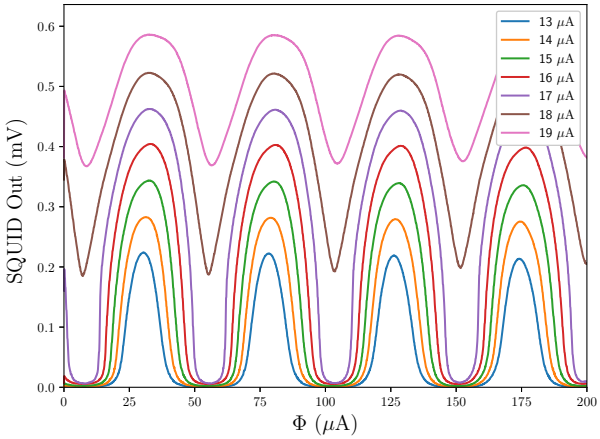

ch25

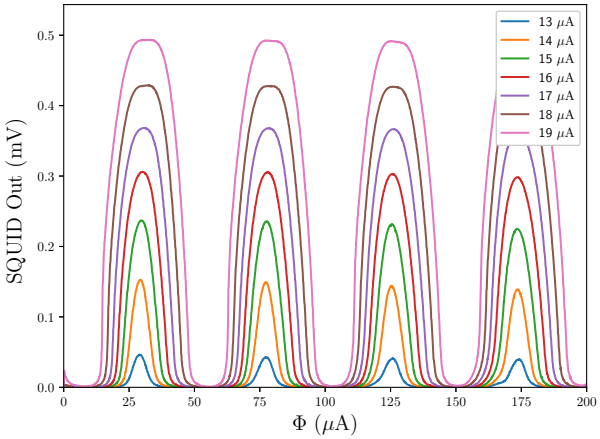

ch26

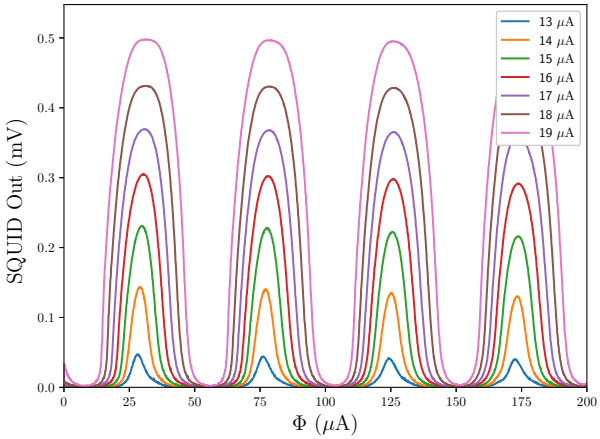

ch33

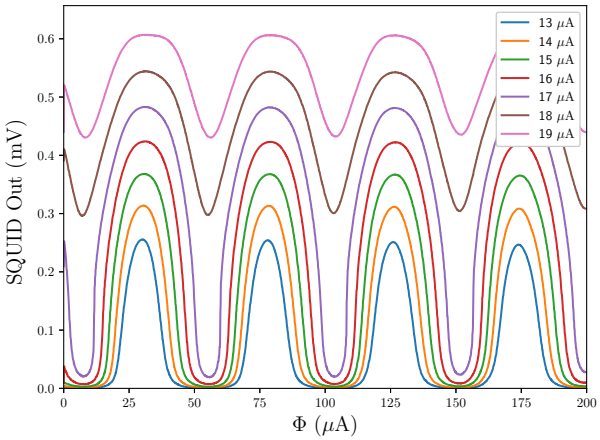

ch34

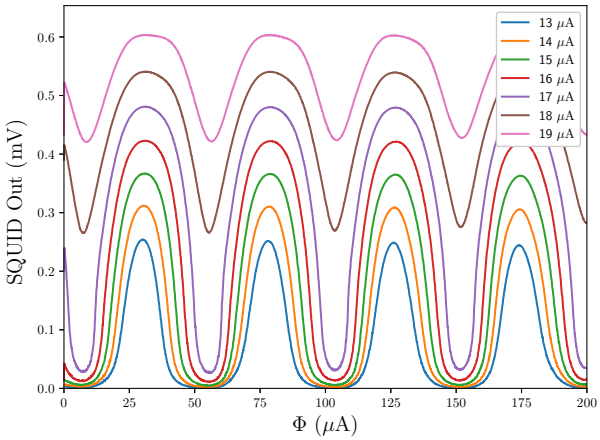

ch35

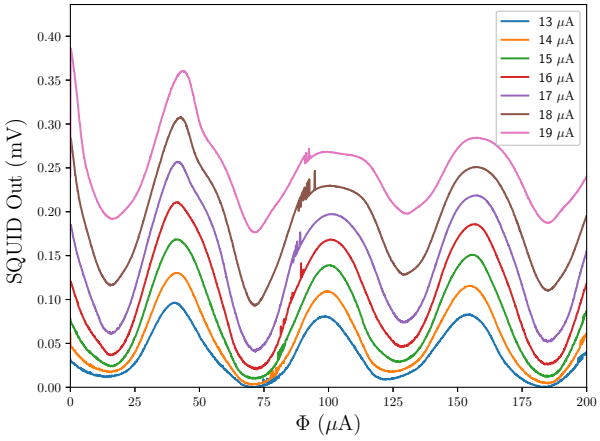

ch41

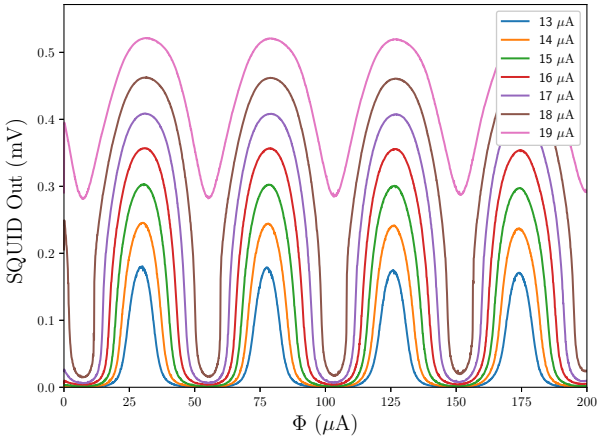

ch42

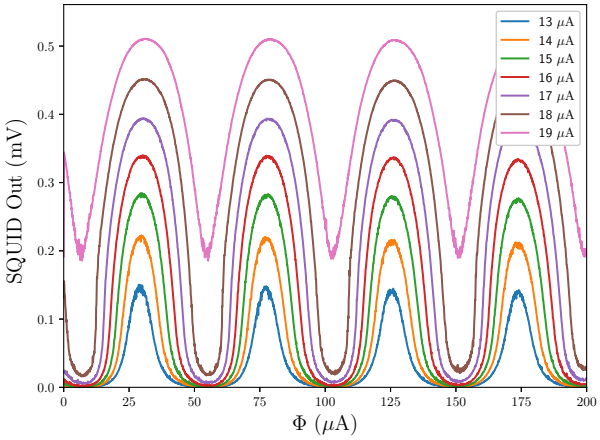

ch49

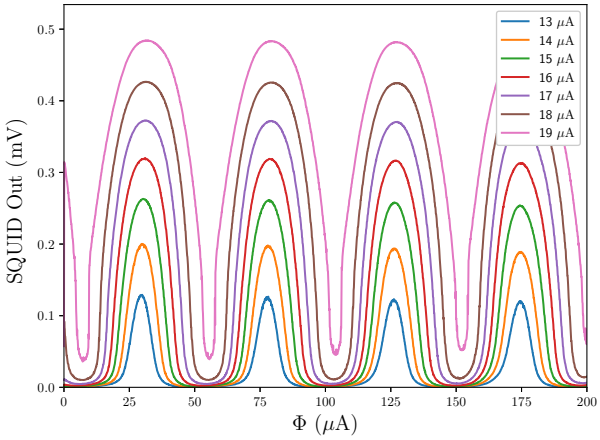

ch50

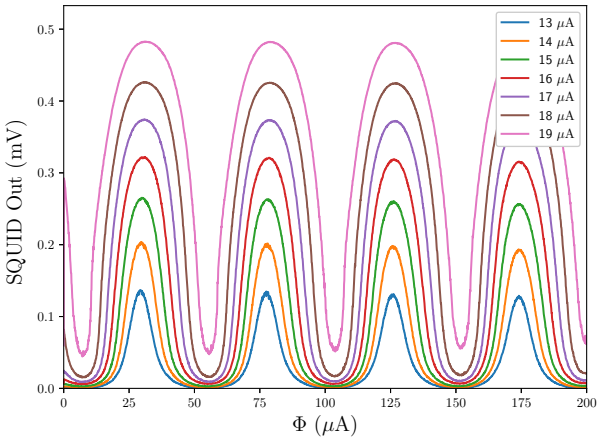

ch57

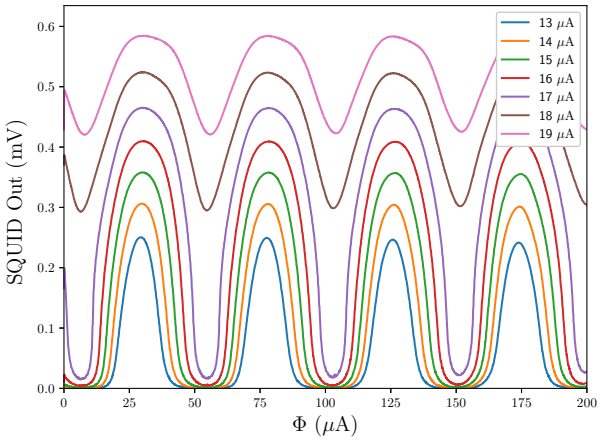

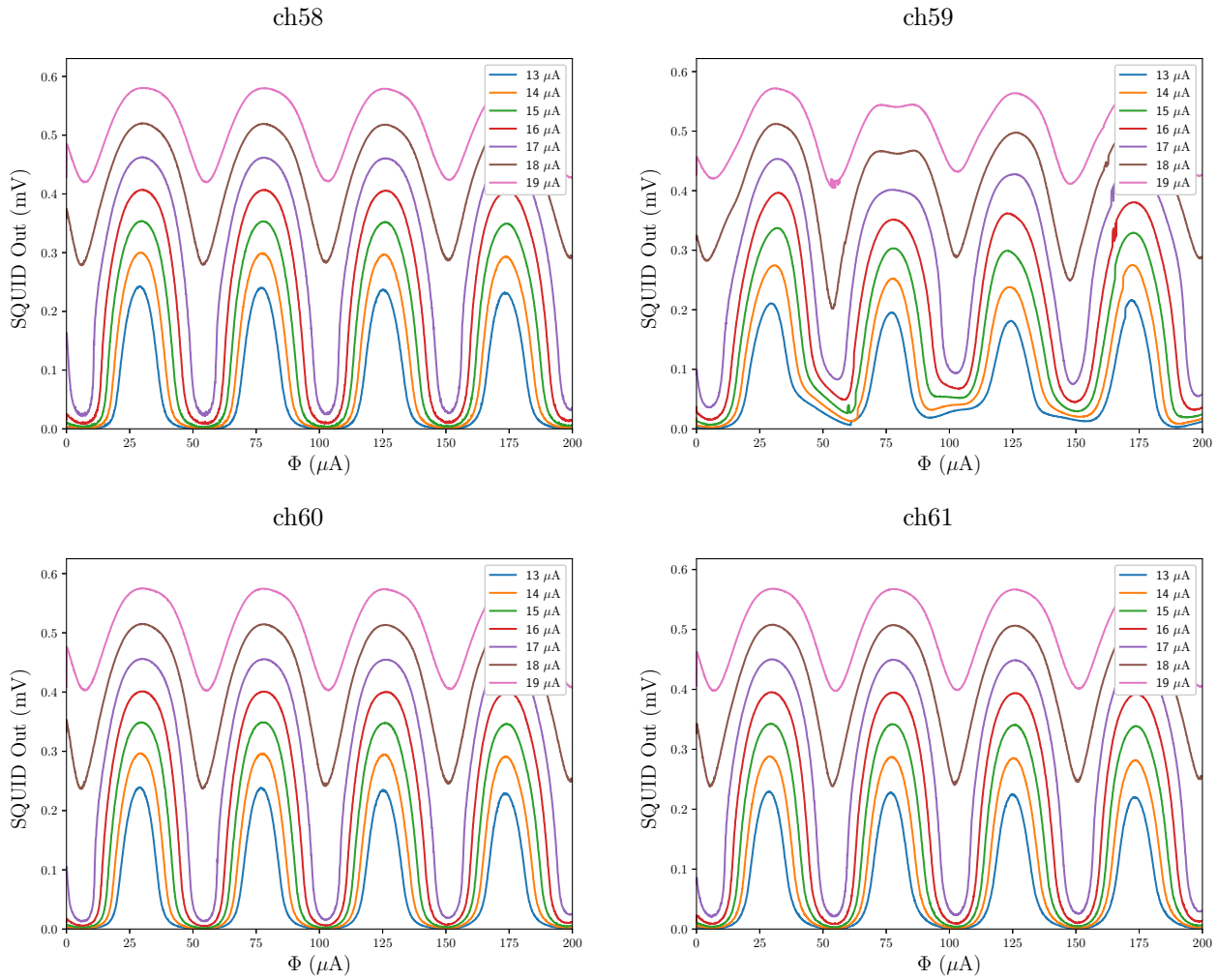

Fig. C.1 Results of relationship between the input magnetic flux Φ and output voltage V as described in Chapter 4. For example, ch 35 and ch 59 are distorted because they have trapped magnetic flux of the residual magnetic field inside the refrigerator.

C.3 Template

ch1

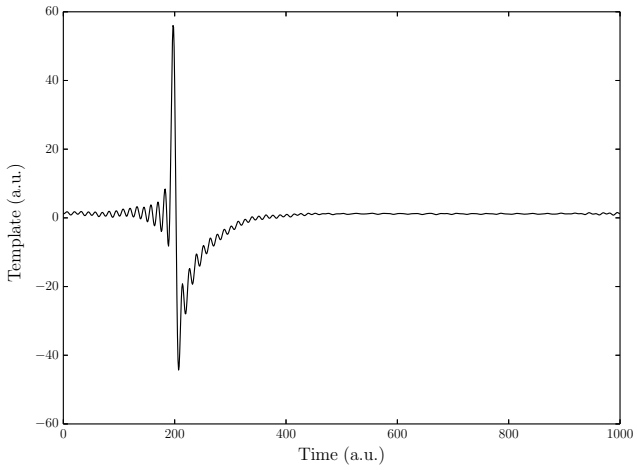

ch2

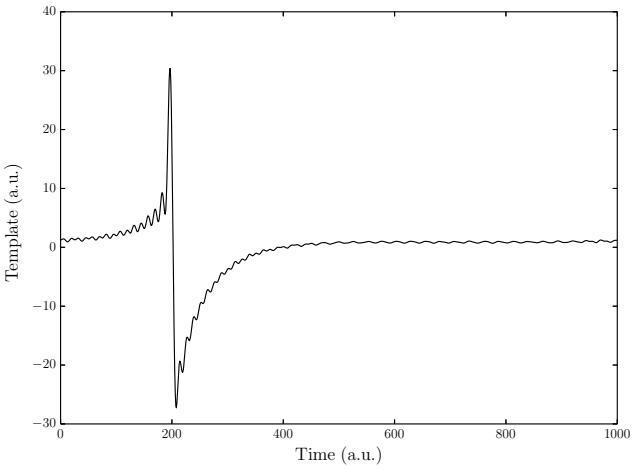

ch3

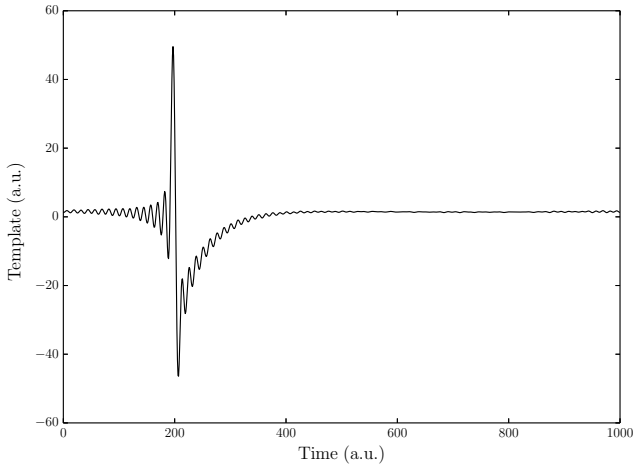

ch4

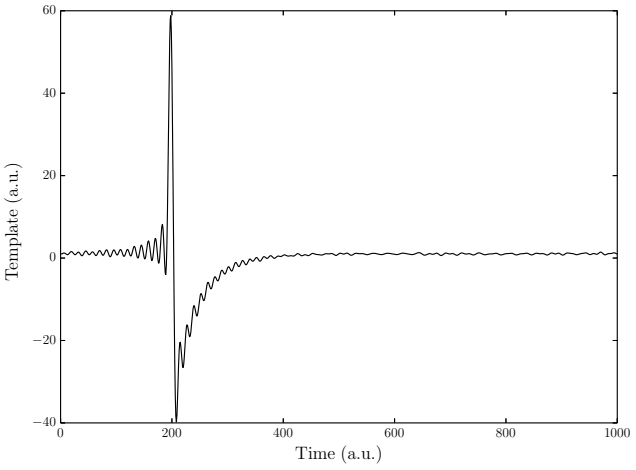

ch5

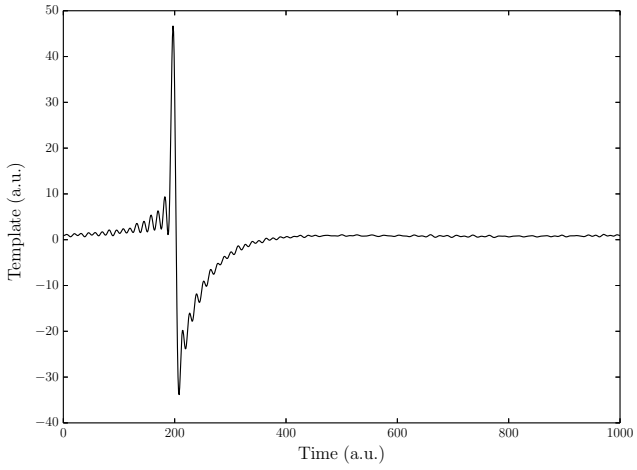

ch6

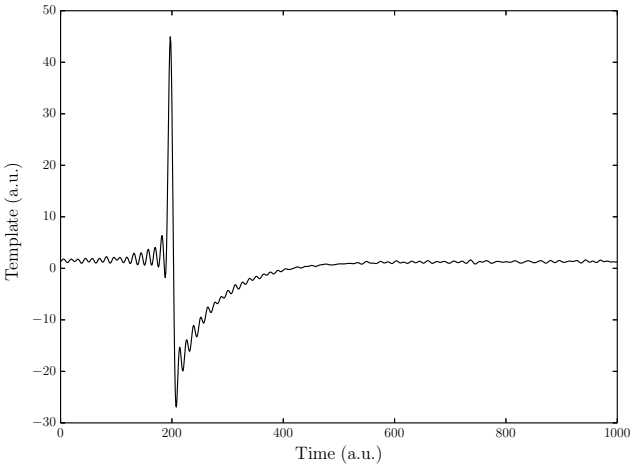

ch11

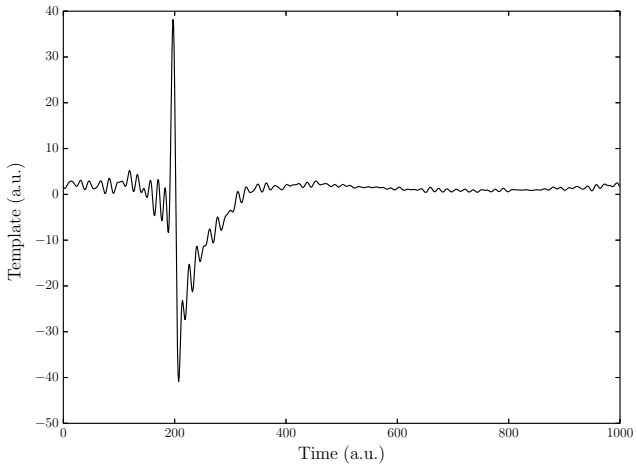

ch13

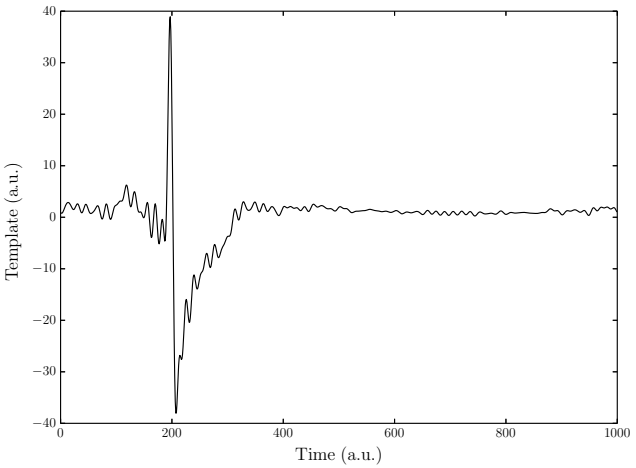

ch33

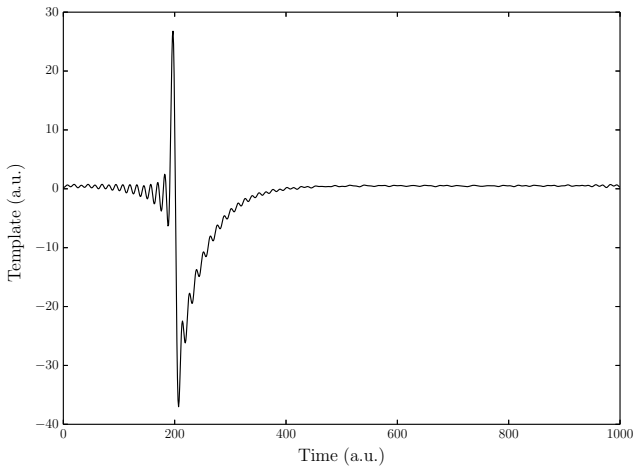

ch34

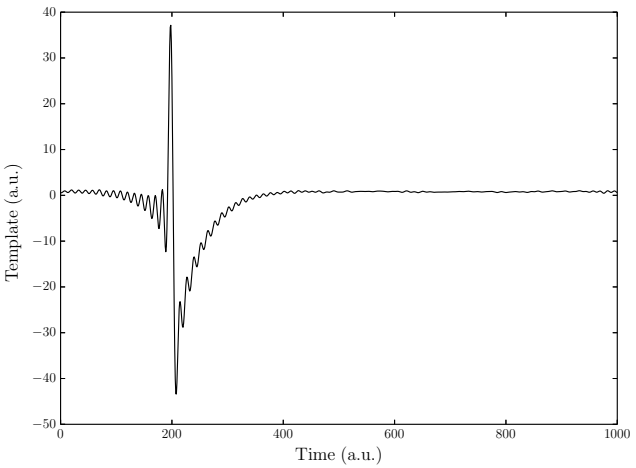

ch41

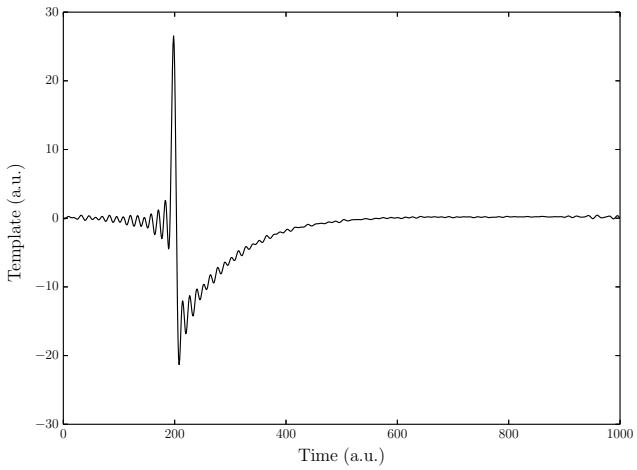

ch49

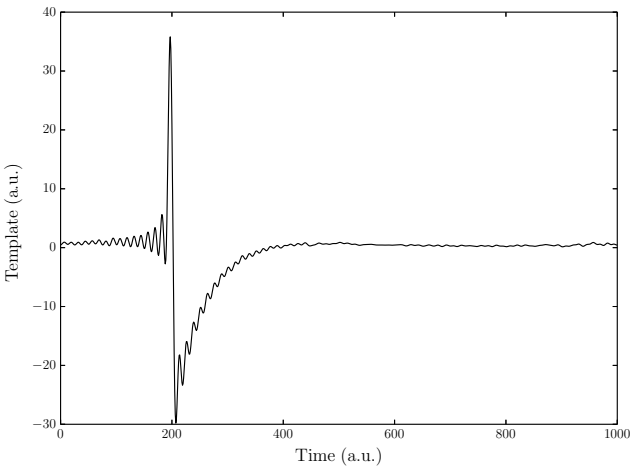

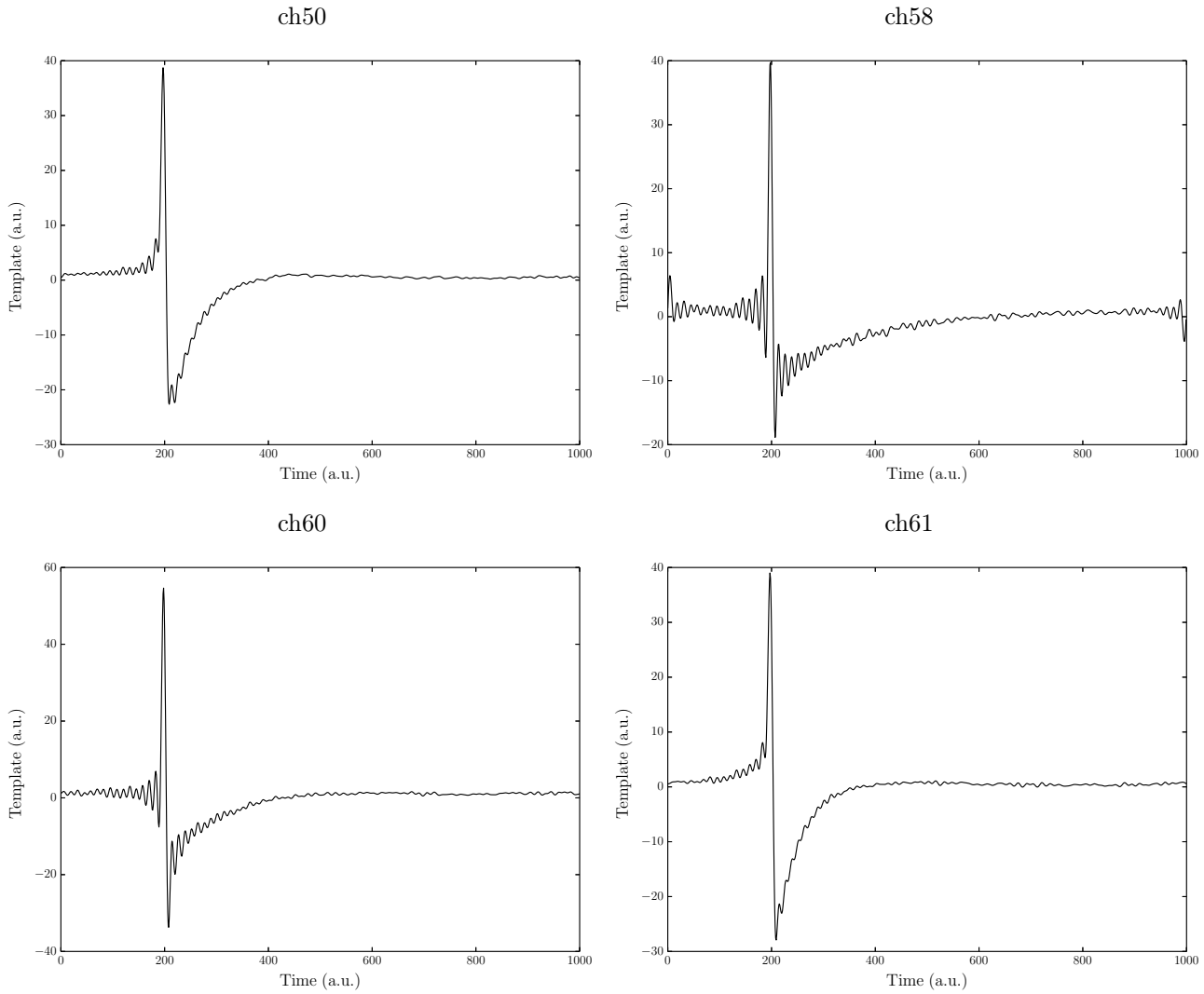

Fig. C.2 Template for optimum filter created from average pulse of the oxygen line

C.4 Gain curve

ch1

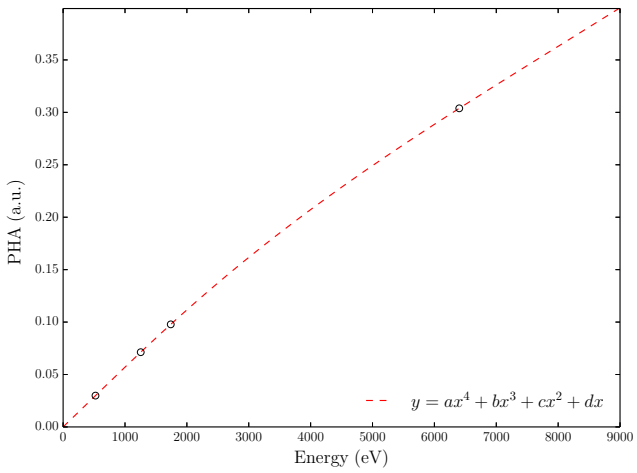

ch2

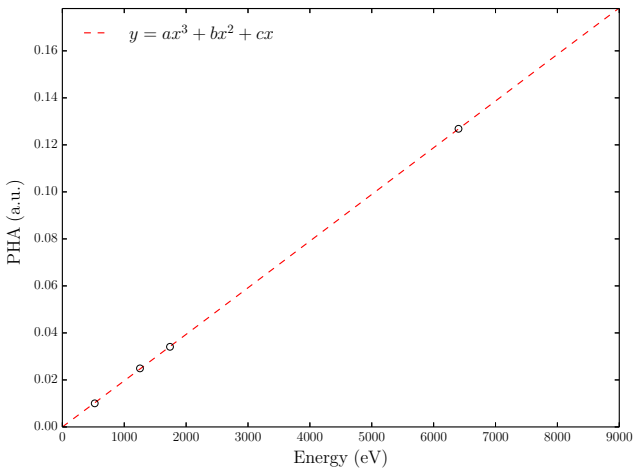

ch3

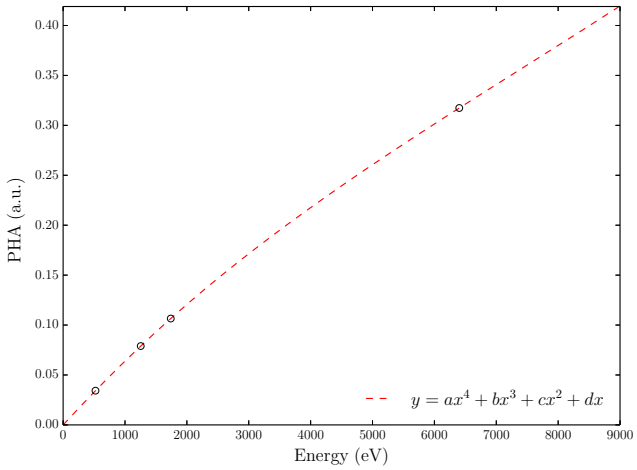

ch4

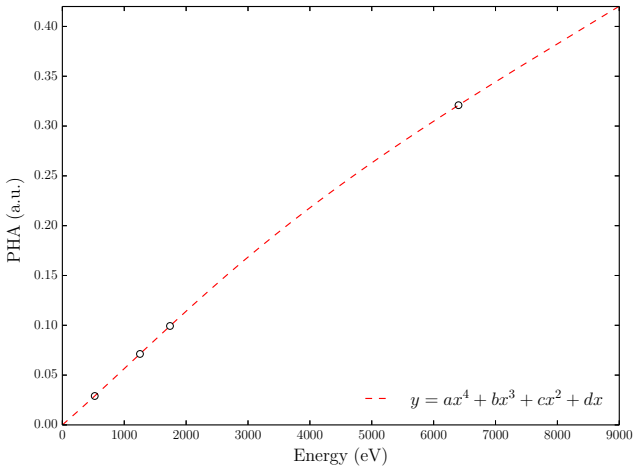

ch5

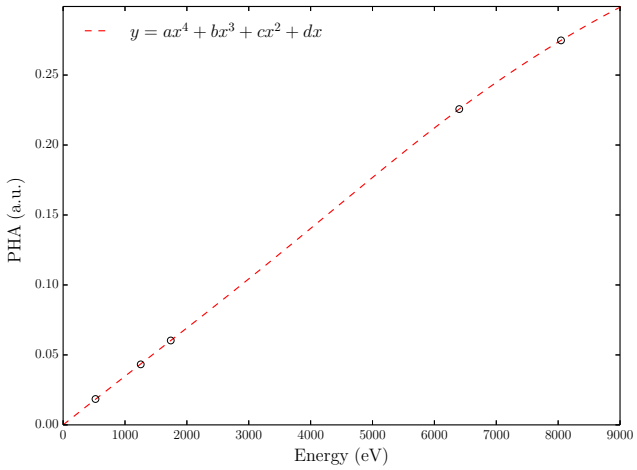

ch6

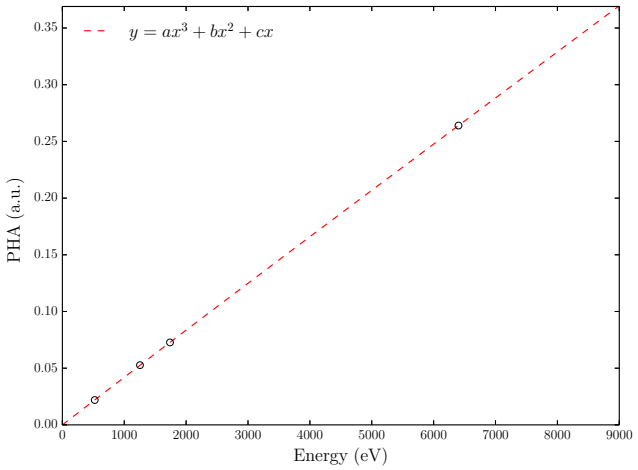

ch11

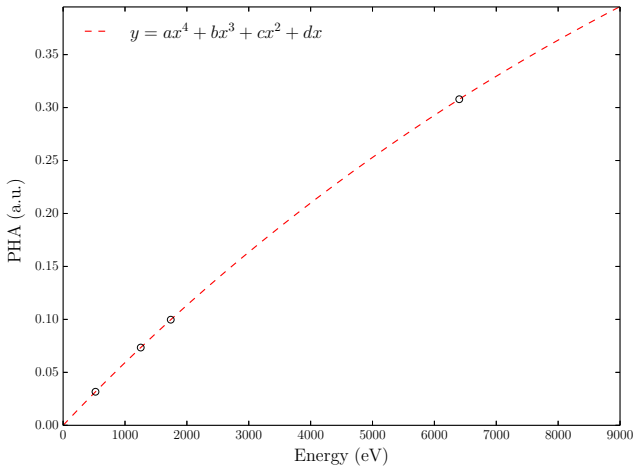

ch13

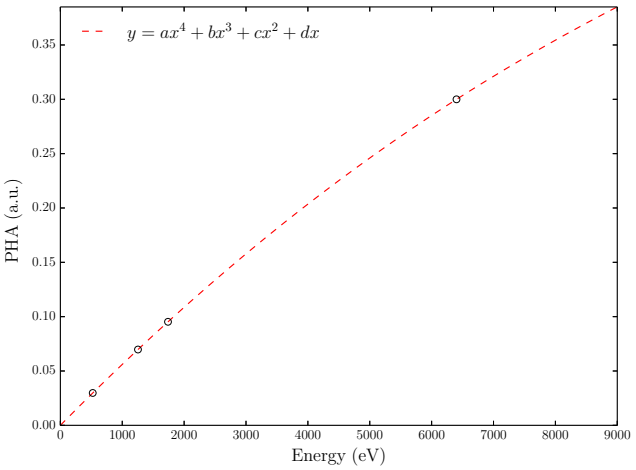

ch33

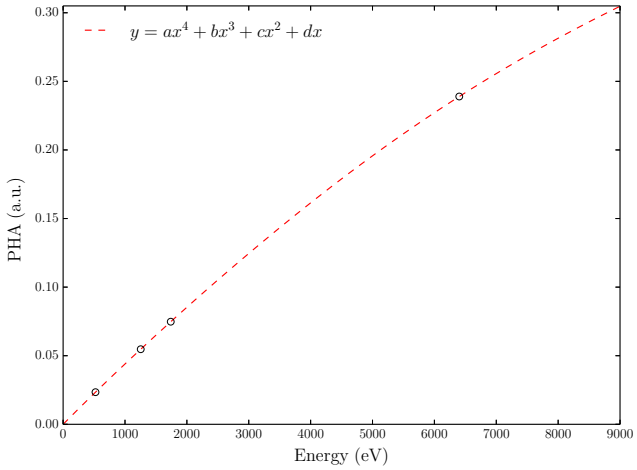

ch34

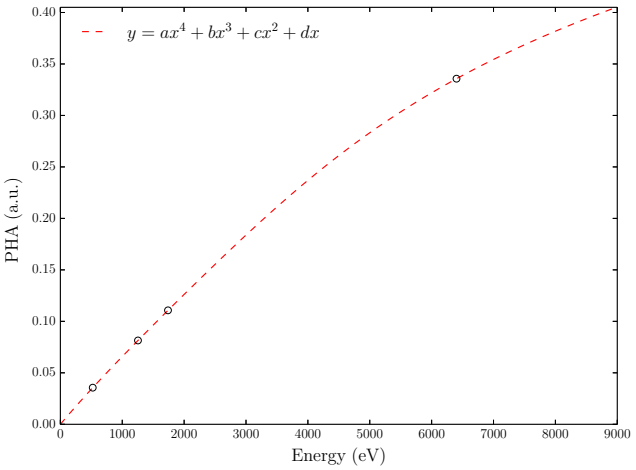

ch41

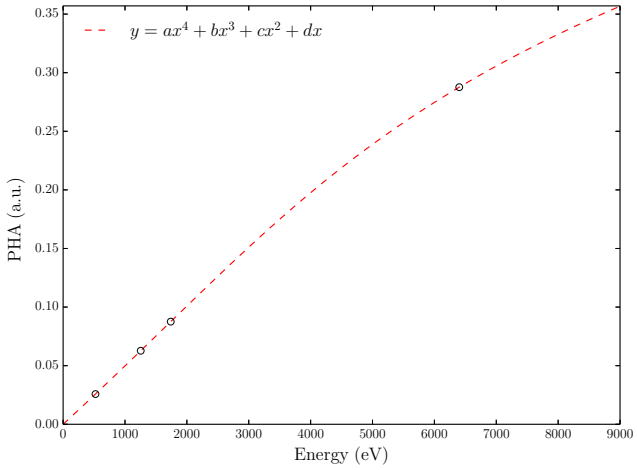

ch49

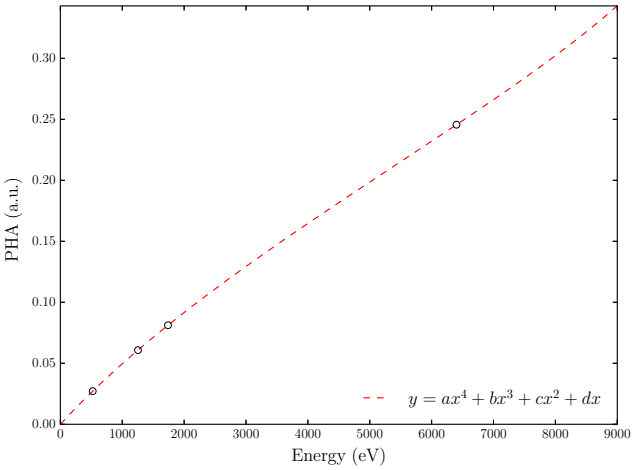

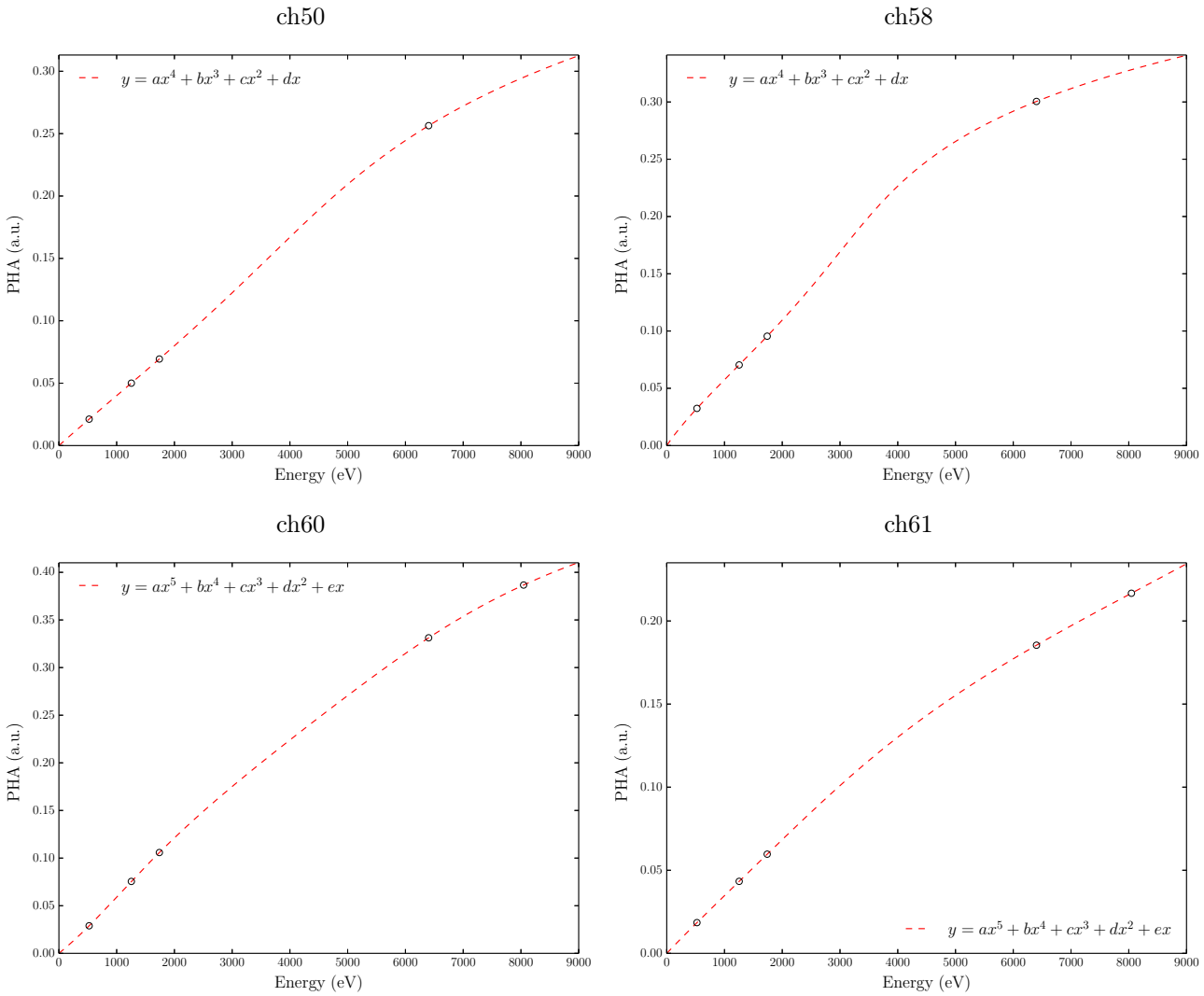

Fig. C.3 Energy calibration curve, 3 to 5th order function is used

Bibliography

[1] H. Akamatsu, L. Gottardi, C. P. de Vries, J. S. Adams, S. R. Bandler, M. P. Bruijn, J. A. Chervenak, M. E. Eckart, F. M. Finkbeiner, J. R. Gao, J. W. den Herder, R. den Hartog, H. Hoevers, R. E. Kelley, P. Khosropanah, C. A. Kilbourne, J. van der Kuur, S. J. Lee, A. J. van den Linden, F. S. Porter, K. Ravensberg, J. E. Sadleir, S. J. Smith, T. Suzuki, E. J. Wassell, and M. Kiviranta. TES-Based X-ray Microcalorimeter Performances Under AC Bias and FDM for Athena. *Journal of Low Temperature Physics*, 184(1-2):436–442, 2016. doi: 10.1007/s10909-016-1525-9.

[2] Hitomi Collaboration. The quiescent intracluster medium in the core of the Perseus cluster. *Nature*, 535 (7610):117–121, 2016.

[3] J W Fowler, W. B. Doriese, G. Hilton, K Irwin, D Schmidt, G Stiehl, D Swetz, J. N. Ullom, and L Vale. Optimization and Analysis of Code-Division Multiplexed TES Microcalorimeters. *Journal of Low Temperature Physics*, January 2012.

[4] G.Cliff and G.W.Lorimer. The quantitative analysis of thin specimens. *Journal of Microscopy*, 103(2): 203–207, 1975.

[5] Toru Hara, Keiichi Tanaka, Keisuke Maehata, Kazuhisa Mitsuda, Noriko Y. Yamasaki, Mitsuaki Ohsaki, Katsuaki Watanabe, Xiuzhen Yu, Takuji Ito, and Yoshihiro Yamanaka. Microcalorimeter-type energy dispersive X-ray spectrometer for a transmission electron microscope. *Journal of Electron Microscopy*, 59(1): 17–26, 2009.

[6] Kent D. Irwin. *Phonon-mediated particle detection using superconducting tungsten transition-edge sensors*. PhD thesis, Stanford University, 1995.

[7] Kent D. Irwin, Michael D. Audley, James A. Beall, J. örn Beyer, Steve Deiker, William Doriese, William Duncan, Gene C. Hilton, Wayne Holland, Carl D. Reintsema, Joel N. Ullom, Leila R. Vale, and Yizi Xu. In-focal-plane SQUID multiplexer. *Nuclear Instruments and Methods in Physics Research, Section A: Accelerators, Spectrometers, Detectors and Associated Equipment*, 520(1-3):544–547, 2004. doi: 10.1016/j.nima.2003.11.310.

[8] H. Katayama, M. Shouho, T. Kohmura, K. Katayama, K. Yoshita, H. Tsunemi, S. Kitamoto, K. Hayashida, E. Miyata, K. Hashimotodani, K. Koyama, G. Ricker, M. W. Bautz, R. Foster, and S. Kissel. Quantum efficiency of the CCD camera (XIS) for the ASTRO-E mission. *Nuclear Instruments and Methods in Physics Research, Section A: Accelerators, Spectrometers, Detectors and Associated Equipment*, 436:74–78, 1999.

[9] F. Kemper, W. J. Vriend, and A. G. G. M. Tielens. The Absence of Crystalline Silicates in the Diffuse Interstellar Medium. *The Astrophysical Journal*, 609:826–837, 2004.

[10] Masanari Koguchi, Ruriko Tsuneta, Yoshihiro Anan, and Koji Nakamae. Analytical electron microscope based on scanning transmission electron microscope with wavelength dispersive x-ray spectroscopy to realize highly sensitive elemental imaging especially for light elements. *Measurement Science and Technology*, 28, 2017.

[11] Corentin Le Guillou and Adrian Brearley. Relationships between organics, water and early stages of aqueous alteration in the pristine CR3.0 chondrite MET 00426. *Geochimica et Cosmochimica Acta*, 131:344–367, 2014.

[12] Akira Shoji Massaki Maezawa, Hirotake Yamamori. A Novel Approch to Chip-to-chip Communication Using a Single Flux Quantum Pulse. *IEEE Transactions on Applied Superconductivity*, 9(2), 1999.

[13] John C. Mather. Bolometer noise: nonequilibrium thoery. *Applied Optics*, 21(6):1125–1129, March 1982.

[14] S H Moseley, J. C. Mather, and D McCammon. Thermal detectors as x-ray spectrometers. *Journal of Applied Physics*, 56(5):1257–1262, September 1984.

[15] Haruka Muramatsu, Tasuku Hayashi, Keisei Maehisa, Yuki Nakashima, Kazuhisa Mitsuda, Noriko Y. Yamasaki, Toru Hara, and Keisuke Maehata. A Study of X-Ray Response of the TES X-Ray Microcalorimeter for STEM. *IEEE Transactions on Applied Superconductivity*, 27(4), 2017.

[16] Satoshi Okuzumi. 衝突密度進化と急速合体成長. **日本惑星科学**, 23(4):371–381, 2014.

[17] K. Sakai, K. Mitsuda, N. Y. Yamasaki, Y. Takei, R. Yamamoto, T. Hara, K. Maehata, N. Iyomoto, and K. Tanaka. TEM-EDS with breakthroughs in 3D wiring and high-speed processing. *Journal of Low Temperature Physics*, 167:759–764, 2012.

[18] Kazuhiro Sakai. *A Frequency-Division Multiplexing Readout System for Large-Format TES X-Ray Microcalorimeter Arrays towards Future Space Missions Kazuhiro Sakai.* PhD thesis, University of Tokyo, 2014.

[19] A E Szymkowiak, R L Kelley, S H Moseley, and C K Stahle. Signal processing for microcalorimeters. *Journal of Low Temperature Physics*, 93(3):281–285, November 1993.

[20] M. Watanabe and D. B. Williams. The quantitative analysis of thin specimens: A review of progress from the Cliff-Lorimer to the new ζ-factor methods. *Journal of Microscopy*, 221:89–109, 2006.

[21] R. Yamamoto, K. Sakai, K. Maehisa, K. Nagayoshi, T. Hayashi, H. Muramatsu, Y. Nakashima, K. Mitsuda, N. Y. Yamasaki, Y. Takei, M. Hidaka, S. Nagasawa, K. Maehata, and T. Hara. Common Bias Readout for TES Array on Scanning Transmission Electron Microscope. *Journal of Low Temperature Physics*, 184(1-2): 454–459, 2016.